Department of Signal
Theory and Communications
UNIVERSITAT POLITÈCNICA DE CATALUNYA
BARCELONATECH

Ph.D. Thesis Dissertation

Ocean surface currents reconstruction from microwave radiometers measurements

Author
Cristina González Haro

Ph.D. Thesis Advisor
Dr. Jordi Isern Fontanet

Ph.D. Thesis Tutor
Dr. Adriano Camps Carmona

Ocean Dynamics and Climate (ODC)
Institut Català de Ciències del Clima (IC3)

Remote Sensing Laboratory
Dept. Teoria del Senyal i Comunicacions
Universitat Politècnica de Catalunya

Barcelona, May 2015

Ocean surface currents reconstruction from microwave radiometers measurements
Ph.D. Thesis, Universitat Politècnica de Catalunya (UPC)

The research described in this Ph.D. Thesis has been mainly carried out at the Institut Català de Ciències del Clima (IC3) under the framework of two research projects lead by Dr. Jordi Isern-Fontanet: MED3D (CTM2009-110200) funded by the Spanish Ministry of Science and Innovation and MICROVELS (CIVP16A1819) funded by Fundación Ramón Areces. This Ph.D. Thesis has also been partially funded by the Spanish SEPE.

The author whished to thank in particular the Dept. d'Oceanografia Física del Institut de Ciències del Mar (ICM-CSIC) for hosting her during the final steps of this Ph.D. Thesis.

The short term stay at Laboratoire d'Océanographie Spatiale (LOS) IFREMER, Brest (France) was funded by the Mobility Fellowship for students enrolled in a Ph.D. program awarded by the Ministry of Education's Towards Excellence Mention (MHE2011-00129) and the Short Term Scietific Mission (STSM) COST Action (ECOST-STSM-ES1001-010512-017372).

Cover image and design: José Luis Maicas Balaguer.

Abstract

Ocean currents are a key component to understanding many oceanic and climatic phenomena and knowledge of them is crucial for both navigation and operational applications. Therefore, a key problem in oceanography is the estimation of the synoptic velocity field. Currently, global ocean surface velocities are routinely estimated from Sea Surface Height (SSH) measurements provided by altimeters. However, the separation between passes, as well as and the limited number of available altimeters leads to errors in the accurate location of oceanic currents when these measurements are used exclusively. Contrarily, satellite images of Sea Surface Temperature (SST) provide a good qualitative view of the location of ocean patterns, which has encouraged the investigation of alternative methodologies to reconstruct the velocity field based on these observations. This Ph.D. thesis has assessed the capability of SST microwave radiometers observations to retrieve ocean surface currents. The reconstruction of the ocean surface currents from SST observations can be expressed in terms of a transfer function notation, that allows to convert SST maps into SSH, and thus into currents. Because under geostrophic balance, the slope of SSH is proportional to ocean surface currents. This transfer function can be theoretically derived using the Surface Quasi-Geostrophic equations (SQG). Two different approaches were analyzed at a global scale: on one side, the analysis of the validity of the SQG approach has been performed, and on the other, an approach based on the synergetic properties between simultaneous SST and SSH observations has been analyzed. Both approaches have been compared with ocean surface currents retrieved from merged altimetric observations. The study has been focused on the period from October 2002 to May 2005, since during that period there were available four different altimeters, and the quality of the merged altimetric observations was enhanced.

The analysis of the validity of SQG at a global scale revealed that this dynamical model is valid near the major extratropic current system such us the Gulf Stream, the Antartic Circumpolar Current, Kuroshio currents.Besides, the potential of MW SST observations to reconstruct ocean surface currents was analyzed using a synergetic approach: the combination of the SST phase with the SSH spectra. Actually, we explored under which environmental conditions the phase of the MW SST is close to the SSH phase. Results showed that the phase of the MW SST can be used to retrieve ocean currents during winter, near the major extratropical current systems, which are characterized by an intense mesoscale activity and the presence of strong thermal gradients, and deep ML. Furthermore, the reconstruction of the velocity fields from an ideal transfer function built up from simultaneous SST and SSH observations revealed that the

SQG approach can be enhanced.

The spectral properties of this ideal transfer function derived from simultaneous SST and SSH observations was further studied. As a first attempt, the spectral properties of a mean transfer function were characterized at a global scale. Results revealed a flatter response than the k^{-1} predicted by SQG theory near the major extratropical current systems, when the spectral slope was estimated in the wavelength range between 100-400 km. Nevertheless, the spectral slope was closer to k^{-1} in high energetic regions when restricting the analysis to short wavelengths (100-250 km). The flow was then reconstructed using a transfer function that followed a k^{α} model, with α being the estimated spectral slope of the mean transfer function. However, the evaluation of the performance revealed that the reconstruction considering the estimated spectral slope of the mean transfer function did not significantly improve the SQG reconstruction.

The temporal variability of the transfer function was further analyzed. Contrary to the approach previously used, we adjusted the spectral slope in the real domain by using two different metrics: (i) by maximizing the correlation between the flow reconstructed from SST by the transfer function and the flow retrieved from SSH altimetric observations, and (ii) by minimizing the RMSE between both flows. Despite the daily spectral slopes may deviate from k^{-1}, the mean of the three estimated spectral slopes presented similar geographical patterns, with values approximately k^{-1} near energetic regions, such us the ACC. The above analysis revealed that at short scales the SQG approach is a reasonable good approach, at least, from a statistical point of view.

Contents

List of Figures

List of Tables

List of Symbols

Latin symbols

B_{bb}	Blackbody Spectral Brightness [$Wm^{-2}Hz^{-1}Sr^{-1}$].
B	Gray body Spectral Brightness [$Wm^{-2}Hz^{-1}Sr^{-1}$].
c	Speed of light 310^8 [m/s].
D_a	Antena aperture diameter [m].
e	Emissivity.
f	Frequency [Hz].
g	Gravity constant 9.8 [m/s^2].
h	Planck's constant $1.38 \cdot 10^{23}$ [J/K].
m	Mass [kg].
p	Pressure [Pa] (SI base units: [N/m^2 or $kg/(m\ s^2)$]).
T	Temperature [K].
T_B	Brightness Temperature [K].
$\vec{v}$	Velocity field $(u\vec{e}_x + v\vec{e}_y + w\vec{e}_z)$ [m/s].

Greek symbols

α	Spectral slope of the transfer function.
λ	Wavelength [m].
ϵ	Complex dielectric constant.
$\vec{\Omega}$	Coriolis force.
ρ	Fresnel amplitude. (Chapter 2)
	Density [Kg/m^3] (Chapter 3,)
$\Delta\theta_{-3dB}$	Angular resolution [rad].
ψ	Stream Function.

Chapter 1

Introduction

A key problem in oceanography is the estimation of a synoptic velocity field. Ocean currents transport and redistribute heat and salt. Both play an important role in driving the planetary climate system. Of particular importance are the Western boundary currents (e.g., Gulf Stream and Kuroshio Current), which transport heat from the tropics toward the poles, and Eastern boundary undercurrents (e.g., California Undercurrent). For example the Gulf Stream makes that Northwest Europe has a more temperate climate than any other region at the same latitude. Conversly, the climate in Lima, Peru, is cooler (sub-tropical) than the tropical latitudes in which the area is located, due to the effect of the Peru or Humboldt Current. In addition to the horizontal transport of water and heat, vertical motions in the ocean are critical to the exchange of heat and gases such as CO_2 between the surface layer and the deep ocean. Ocean surface currents also contribute to studies of severe weather such as hurricanes, short-term climate phenomena such as El Niño and long-term climate variability.

Ocean surface currents are also crucial to a number of practical applications, such as marine search and rescue and emergency response. Ocean currents carry nutrients as well as pollutants, so it is important to know the currents for ecological and economic reasons. Tests showed[1] that by ingesting ocean current data into the Search and Rescue system, the search area decreased by 66% over 96 hours. By reducing the search area, crews can focus their efforts and save more lives. For ship routing applications (McCord *et al.* , 1999; Davidson *et al.* , 2009), small savings in fuel by better use of surface currents is a real challenge. In addition, modern commercial vessels are so large that currents below the surface have huge effect on navigation. The job of the port pilots would be easier, and ship navigation and safety would improve if there were a better understanding of the currents from the surface to the bottom.

[1] `http://www.ioos.noaa.gov/hfradar/welcome.html` Last visit: April 8, 2015

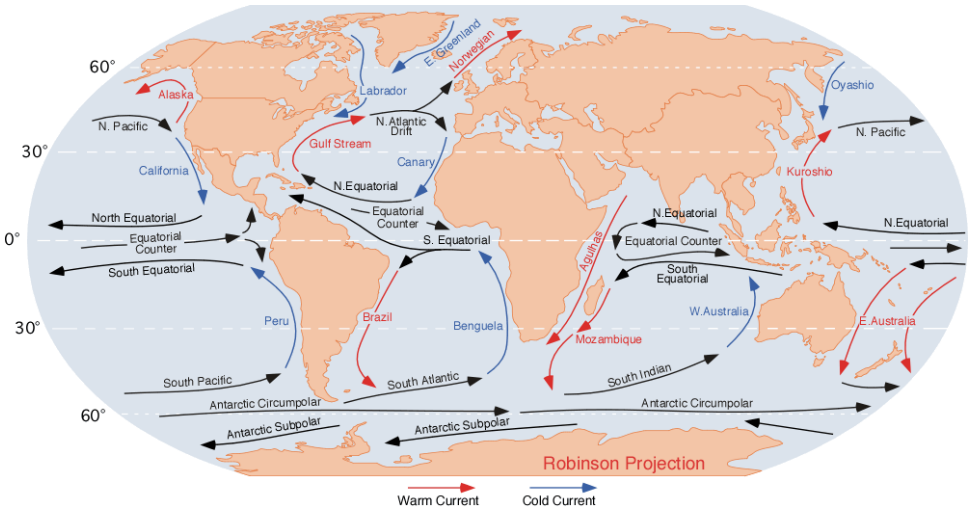

Figure 1.1: World ocean currents. Red arrows indicate warm currents, while cold currents are displayed in blue. Figure from `http://en.wikipedia.org/wiki/File:Corrientes-oceanicas.png` Last visit: April 12, 2015

1.1 Ocean currents

Ocean surface circulation

The ocean surface circulation is mainly driven by the wind stress and the water desnsity variations. Surface currents are formed by the interaction between wind patterns (easterly in the tropics, and westerly in mid-latitudes), the presence of the continents and the Coriolis force. As a result of these factors, the surface ocean circulation in the mid-latitudes is characterized by clockwise gyres in the Northern hemisphere and counterclockwise gyres in the Southern hemisphere. A typical gyre displays four types of joined currents: two east-west aligned currents found respectively at the top and bottom ends of the gyre; and two boundary currents oriented north-south and flowing parallel to the continental margins. For instance, the Gulf Stream, a narrow western boundary current, paired with the eastern boundary Canary Current, flanks the North Atlantic gyre. Its counterpart in the western Pacific is the Kuroshio current, which is part of the North-Pacific gyre. In addition to the currents that form the major ocean gyres, the Antartic Circumpolar Current (ACC) is the dominant feature in the Southern ocean, and the only current that flows completely the globe (Figure 1.1).

The ocean is a turbulent environment. The most energetic kind of ocean circulation variability is associated with so-called mesoscale variability (eddies, meandering currents or fronts), i.e. features on a 50-400 km scale, lasting 10-100 days, with currents of a few kilometres per hour. The energy of these mesoscale processes generally exceeds that of the mean flow by an order of magnitude or more. The mean current speeds with streamlines shown in Figure 1.2 (Lumpkin & Johnson, 2013) clearly illustrate the prominent large-scale currents such as the western boundary currents, their extensions, the equatorial current systems, and parts of the ACC. The global histogram of mean speeds (top left in Figure 1.2) shows that the maximum

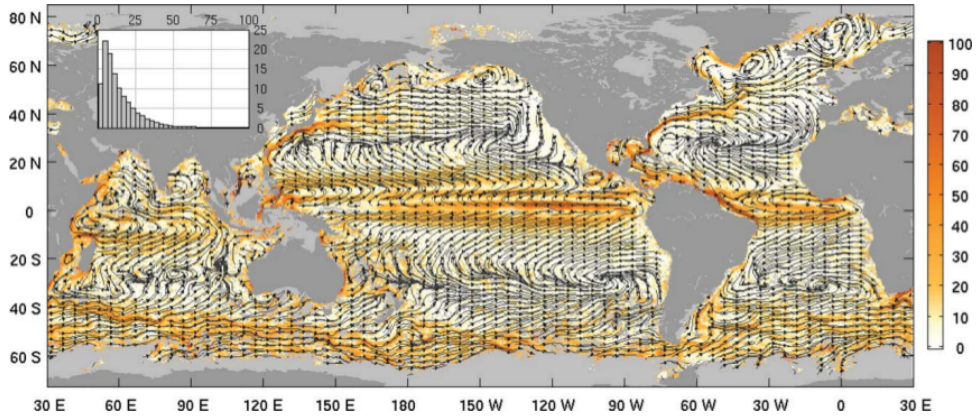

Figure 1.2: Mean current speeds (colors, in cm s^{-1}) from near-surface drifter data with streamlines (black lines). Stream-lines illustrate large-scale circulation features. Inset (top left) shows histogram of mean current speed (cm s^{-1}, horizontal axis, from 0 to 100 at 3.125 cm s^{-1} intervals) versus number of bins (in kilobins, vertical axis, from 0 to 25,000 bins). (Lumpkin & Johnson, 2013)

mean velocity is around 60 cm s^{-1}.

Historical perspective

Our knowledge of oceanic currents, winds, and tides goes back thousands of years. Polynesian navigators traded over long distances in the Pacific as early as 4000 bc (Service, 1996). Arabic traders used their knowledge of the reversing winds and currents in the Indian Ocean to establish trade routes to China in the Middle Ages and later to Zanzibar on the African coast (Stewart, 2004). Modern European knowledge of the ocean began with voyages of discovery by Bartholomew Dias (1487-1488), Christopher Columbus (1492-1494), Vasco da Gama (1497-1499), Ferdinand Magellan (1519-1522), and many others. They established the global trade routes from Spain to the Caribbean, and Philippines in the early 16th century. The routes were based on a good working knowledge of trade winds, the westerlies, and western boundary currents in the Atlantic and Pacific (Couper, 1983). The European explorers were soon taken over by scientific voyages of discovery led by (among many others) James Cook (1728-1779) on the Endeavour, Resolution, and Adventure, Charles Darwin (1809-1882) on the Beagle, and Sir James Clark Ross and Sir John Ross who surveyed the Arctic and Antarctic regions from the Victory, the Isabella, and the Erebus. Others collected oceanic observations and produced useful charts, including Edmond Halley who charted the trade winds and monsoons and Benjamin Franklin who charted the Gulf Stream. Franklin's Gulf Stream chart (see Figure 1.3) was published in 1770 in England, where it was ignored for many years. Once the British sailors followed Franklin's advice on navigating the current, they were able to gain two weeks in sailing time.

Slow ships of the 19th and 20th centuries led into satellites, drifters, and autonomous instruments toward the end of the 20th century. Satellites now observe the ocean, the air, and the land. Thousands of drifters and other *in-situ* sensors observe the upper two kilometers of the

Figure 1.3: The 1786 version of Franklin-Folger map of the Gulf Stream. Figure from: `http://commons.wikimedia.org/wiki/File:Franklingulfstream.jpg` Last visit: April 12, 2015.

ocean. Data from these systems, when fed into numerical models allows the study of the Earth as a system. For the first time, the interactions of biological, chemical, and physical systems can be studied to determine the past, current and future states of the Earth.

1.2 Measuring ocean surface currents: In-situ

Ocean surface currents can be measured *in-situ* using a variety of sensors and techniques, e.g. through mooring current meters, shipboard Acoustic Doppler Current Profiler (ADCP), CTD transects, gliders, surface drifters, and Argo floats, among others.

Geostrophic-Density

At scales of interest, currents are in geostrophic equilibrium, i.e. the pressure gradient force is balanced by the Coriolis effect. The resulting balance implies that currents are proportional to the preassure gradients:

$$u \equiv -\frac{1}{f_0 \rho_0}\frac{\partial p}{\partial y} \qquad v \equiv \frac{1}{f_0 \rho_0}\frac{\partial p}{\partial x}, \tag{1.1}$$

where f_0 is the Coriolis parameter, ρ_0 is a constant density and p is the pressure. Thus, since the ocean is in approximately hidrostatic equilibrium, the above equations can be used to relate currents to horizontal density gradients through the so-called thermal wind equations (Vallis,

2006):

$$\frac{\partial v}{\partial z} = -\frac{g}{f_0 \rho_0}\frac{\partial \rho}{\partial x} \qquad \frac{\partial u}{\partial z} = \frac{g}{f_0 \rho_0}\frac{\partial \rho}{\partial y}. \tag{1.2}$$

Thermal wind equations have been extensively used in the past in order to retrieve ocean currents once the distribution of density in the ocean was known. Before the deployments of drifters buoys, it was easier to obtain observations of density (from measurements of salinity and temperature) than it was to measure currents directly. With an instrument like a Conductivity Temperature Depth (CTD), salinity and temperature can be observed as a function of depth. These *in-situ* observations can be converted to potential density using the equation of state for seawater (Millero *et al.* , 2008).[2].

ADCP

The ADCP exploits the Doppler effect by emitting a sequence of high frequency pulses of sound that scatter off of moving particles in the water. Depending on whether the particles are moving toward or away from the sound source, the frequency, or pitch, of the return signal bounced back to the ADCP is either higher or lower. Particles moving away from the instrument produce a lower frequency return and vice versa. (see to section 1.7.4 of Emery *et al.* (1986) for further details).

On large research vessels the ADCP is permanently mounted on the bottom of the ship's outer hull. A typical unit is powerful enough to sample waters as deep as 700 m. During operation, the ADCP is sending out and receiving several acoustic pulses every second. An on-board computer processes the returned signal and a real-time display of the magnitude and direction of the current throughout the water column is produced, and can be monitored nearly continuously while the ship is in motion. The ADCP are also mounted on mooring current meters. They are mostly deployed at equatorial locations where geostrophy breaks down and direct velocity measurements are required[3]. Finally, the ADCP can be mounted on a CTD probe, which in this case is known as Lowered-ADCP (LADCP).

The Joint Archive for Shipboard ADCP (JASADCP)[4] is reponsible for the acquisition, review, documentation, archival, and distribution of shipboard ADCP data sets and LADCP[5]. See section 4.4 for further details.

Surface Drifter

Satellite-tracked drifting buoys (Sybrandy & Niiler, 1991; Niiler, 2001) provide observations of near-surface circulation. A drifter is composed of a surface float which includes a transmitter to relay data, and often a thermometer that reads temperature a few centimeters below the air/sea interface (Lumpkin & Pazos, 2007). The surface buoy is attached to a holey-sock drogue,

[2] `http://www.teos-10.org/` Last visit: April 10, 2015.
[3] `http://www.pmel.noaa.gov/tao/proj_over/mooring.shtml` Last visit: April 12, 2015.
[4] `http://ilikai.soest.hawaii.edu/sadcp/` Last visit: April 8, 2015.
[5] `http://ilikai.soest.hawaii.edu/ladcp/` Last visit: April 8, 2015.

centered at a depth of 15 m. The drifter follows the flow integrated over the drogue depth, although some slip with respect to this motion is associated with direct wind forcing (Niiler & Paduan, 1995).

Drifter velocities are derived from finite differences of their position fixes. These velocities, and the concurrent SST measurements, are archived at the Atlantic and Oceanographic Metereological Laboratory-AOML's Drifting Buoy Data Assembly Center[6] where the data are quality controlled and interpolated to 1/4-day intervals (Hansen & Herman, 1989; Hansen & Poulain, 1996).

ARGO

Argo[7] are drifting autonomous CTD profiles that aims to measure the physical state of the global ocean (actually Temperature and Salinity in the upper 2000 m) with an array of roughly 3000 floats cycling every 10 days, and over a period of several years (possibly several decades). Float launchings began in 1999, but the number of 3000 floats working at sea at the same time was reached only in 2007.

Although measuring surface velocity is not the primary mission of Argo floats, they typically spend 6-24 hours at the surface transmitting data to passing satellites. During this time, their position fixes can be used to infer surface velocity (Lebedev *et al.* , 2007; Park *et al.* , 2005), although with less accuracy than drifters because they are not drogued and are thus more susceptible to wind and wave action.

1.3 Measuring ocean surface currents: Remote

Satellite remote sensing is an ideal tool for studying ocean surface dynamics. The regular, repeated coverage offered by satellite systems cannot be achieved by *in-situ* measurements. However, the ability to capture the desired features of the global surface current systems becomes challenging for satellite systems as the spatial and time scales of the processes become smaller. Therefore, it reinforces the complementary of both observation systems: satellite and *in-situ* measurements.

Today's satellite sensors provide a wide range of data that contain information about ocean currents. The most direct method uses satellite altimetry to estimate surface currents. However, other sources of remotely sensed data such as, Sea Surface Temperature (SST) provided by radiometers, are used to asess current velocity with a variety of methods.

Radar Altimetry

At scales of tens of kilometers and larger, for approximately steady motions, and away from boundaries, the primary balance of forces is between horizontal pressure differences and the

[6] `http://www.aoml.noaa.gov/phod/dac/dacdata.php` Last visit: April 8, 2015.
[7] `http://www.argo.ucsd.edu/` Last visit: April 8, 2015.

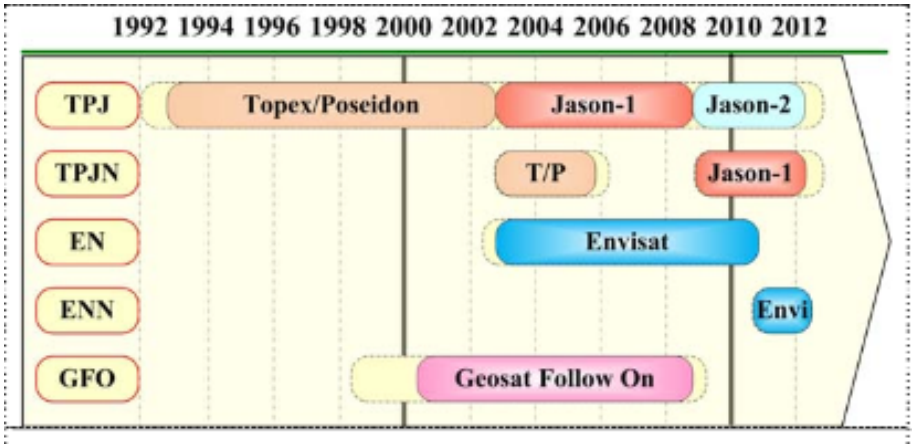

Figure 1.4: Time span of different altimeter missions (Yu *et al.* , 2014).

Coriolis force, which drives currents that follow lines of constant pressure, known as geostrophic currents. Because pressure is related to sea surface height (SSH), geostrophic currents (equation 1.1) can be calculated using horizontal gradients in SSH, as:

$$u = -\frac{g}{f_0}\frac{\partial \eta}{\partial y}, \qquad v = \frac{g}{f_0}\frac{\partial \eta}{\partial x} \tag{1.3}$$

where u and v are the zonal and meridional components of the velocity field, respectively. g is the gravity constant, f_0 is the coriolis parameter and η is the SSH.

Satellite altimeters measure the height of the sea surface along-track. These measurements allow to recover only the perpendicular component to the track. The trade off between spatial and temporal sampling of a single satellite altimeter makes it difficult to track the two-dimensional motion of the ocean. This limitation can be circumvented by combining different altimetric missions. Accordingly, Ducet *et al.* (2000) gave the first results of the global mapping of sea level and ocean circulation variations from the combination of TOPEX/POSEIDON (T/P hereafter) with ERS-1 and ERS-2. By comparing the SSH wavenumber spectrum from the merged data to that from the along-track data, they estimated the resolution of the merged data to be about 150 km in wavelength. The mapping of the ocean signal was done globally through an improved objective analysis method that takes long wavelength residual errors into account and uses realistic correlation scales of the ocean circulation with a global resolution of 1/4 degree every 10 days. SSALTO/DUACS project applied the sub-optimal interpolation technique to construct gridded data sets from multi-mission altimeter data (Le Traon & Dibarbourne, 2002).

The field of satellite altimetry thus benefits from almost two decades of international cooperation, with at least two altimeters in orbit at ant given time (see Figure 1.4). Although a two altimeter configuration provides a quite good representation of the mesoscale variability, Pascual *et al.* (2006) showed that a four altimeter configuration enhances the correct location of oceanic structures (Figure 1.5)

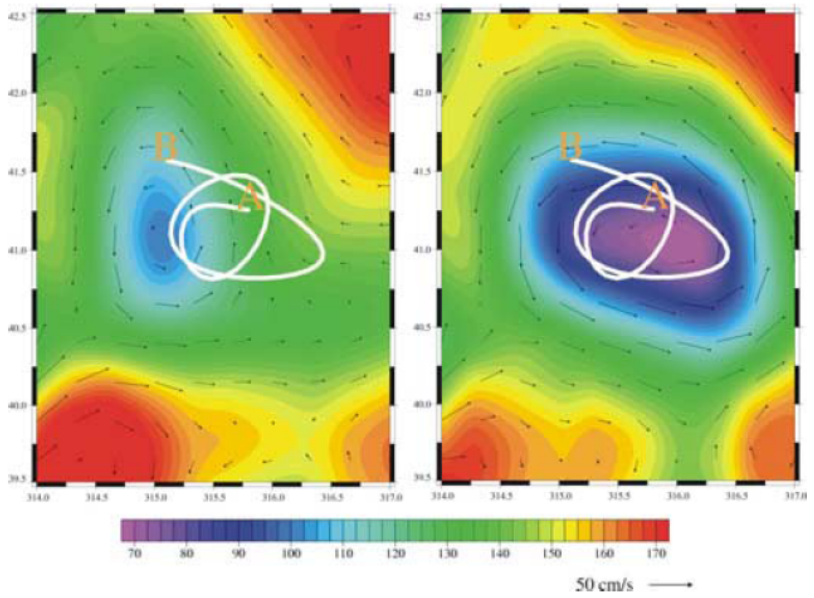

Figure 1.5: Enhancement of altimetry merged product Buoy trajectory (white line, from May 14, 2003 to May 28, 2003, from A to B) and merged absolute dynamic topography in the Gulf Stream on May 21, 2003. Left with 'only' two satellites, right with four satellites. The right map corresponds more closely to the eddy revealed by the buoy's path. Vectors correspond to the absolute velocity (Pascual *et al.* , 2006).

Suface velocity from Passive Radiometer observations

During the last few decades different techniques have been proposed to derive velocities from sequences of Sea Surface Temperature (SST) provided by passive radiometers: the Maximum Cross-Correlation (MCC) method (Emery *et al.* , 1986; Bowen *et al.* , 2002; Afanasyev *et al.* , 2002; Dransfeld *et al.* , 2006); the constrained optical flow method and the inversion of the heat equation (e.g. Kelly, 1989; Vigan *et al.* , 2000; Marcello *et al.* , 2008) and the neural network approach (Cote & Tatnall, 2007). Among these techniques, the MCC method is by far the most widely used. The basic idea consists of estimating the displacement of tracer patterns between two consecutive images by measuring the distance between pairs of windows ($\sim$ 20 km) located in different images. These pairs of windows are selected to have the maximum cross-correlation between tracer fields. Although this technique has been throughly validated with *in-situ* data and numerical models (Tokmakian *et al.* , 1990; Bowen *et al.* , 2002), its implementation is complex and demands high resolution ($\sim$ 1 km) cloud-free images over sufficiently short time periods ($\sim$ 6 h). In addition, the resulting velocity field has spatial resolutions lower than the original image due to the size of the window used. Furthermore, the need for cloud-free sequences of SST images, which is common to all of the above methods, constrains its operational use.

Alternatively, new methods able to diagnose the velocity field from a single SST image have been put forward during the last few years. In particular, two different approaches have been proposed: the multifractal analysis (Turiel *et al.* , 2005; Isern-Fontanet *et al.* , 2007; Turiel *et al.* , 2009) and the Surface Quasi-Geostrophic (SQG) equations (Lapeyre & Klein, 2006a;

LaCasce & Mahadevan, 2006; Isern-Fontanet *et al.* , 2006). The multifractal analysis exploits the property that SST multifractal components are closely linked with the ocean flow, which allows to make a reasonable guess about the stream function, referred to as the Maximum Singular Stream function (MSS), from a single SST image. However, the technique is limited and information on the direction of the current is not available. On the contrary, the SQG approach allows for reconstruction of not only surface velocities, but also the 3D velocity field; with the only ambiguity being the overall energy level. This ambiguity can be easily solved however, by comparing the resulting velocity field with altimetric or *in-situ* measurements (e.g. Isern-Fontanet *et al.* , 2008).

Doppler-Based Surface Velocities from SAR

An alternative method for calculating surface currents is through the explotation of the Doppler shift in synthetic aperture radar data (Chapron *et al.* , 2005). Excellent results have been achieved using the Doppler anomaly of satellite SAR instruments, but a significant limitation of the technique means that only currents perpendicular to the track can be estimated. Along-track SAR interferometry provides an alternative method but again, only one dimension can be estimated using conventional satellite SAR system. However, the DBI (Dual Beam Interferometer) tecnique combines two interferometric SAR looking at 20 degrees squint forward and backward from broadside, to allow estimation of vector surface velocities (Frasier & Camps, 2001). This is the approach that will be followed in the Wavemill mission.

High Frequecy Radar

Contrary to the previous remote sensing devices, High frequency (HF) radar systems are shore-based. Following the same premise of the ADCP, these shore-based instruments use the Doppler effect to determine when currents are moving toward or away from the shore. These radars can measure currents over a large region of the coastal ocean, from a few kilometers offshore up to 200 km, and they can operate under any weather conditions. To calculate both components of the velocity field, a second HF radar installation measuring the same currents from a different angle is required.

Several countries have begun using HF radar-derived ocean currents for their operational oceanographic needs[8] According to the Global High Frequency Radar Network[9] there are at least 400 HF radars deployed in many countries. The Global High Frequency Radar Network, inaugurated with a kickoff meeting at Oceanology International in London, England, on March 14, 2012, aims at increasing the number of coastal radars operating around the world, and at ensuring that HF radar data are available in a single standardized format in real-time.

[8] `http://www.emodnet-physics.eu/hfradar/docs/confirmed/The%20Global%20High%20Frequency%20Radar%20Network.pdf` Last visit: April 10, 2015.

[9] `http://www.ioos.noaa.gov/globalhfr/welcome.html` Last visit: April 10, 2015.

1.4 Key Challenges and future developements

Satellite systems can now capture the main ocean currents and their associated mesoscale variability. With more than 20 years of altimetry, changes at time scales relevant to climate can now begin to be observed. However, many important physical processes cannot be observed with the actual sensors because of their faster time scales and smaller spatial scales. This is the case of submesoscale features, such as small eddies and high potential filaments. Modeling studies that account for filaments are beginning to show that motions at these small scales are responsible for as much vertical transport as the large eddies (Lapeyre & Klein, 2006b).

These major advances point to the need of repeated global observations at finer space and time scales than are presently resolved by conventional atimeters. The planned Surface Water and Ocean Topograhy (SWOT) mission will provide unprecedent global characterization of fine-scales features and fronts, with much closer coastal coverage. SWOT proposed by Rodriguez *et al.* (1999) in the form of the former Wide Swath Ocean Altimeter (WSOA) consists of two side-looking antennae separated by a boom with a length of 10 m (Fu & Rodriguez, 2003). Even though the measurement errors of SWOT will be smaller than with conventional altimeters, the SWOT Project estimates that the measurement errors will be equivalent to the ocean signal at scales (spectral wavelengths) of 15 km on a global average, and the errors will mask the ocean signal at smaller scales. SWOT will make these fine resolution observations within two 50 km wide swaths separated by a 20 km nadir gap. A conventional nadir-looking altimeter will also be onboard SWOT for making SSH measurement along the center of the nadir gap.

After initial internal investigations the European Space Agency (ESA) is pursuing a programme of steps aimed towards the development of a Wavemill-based mission. The Wavemill concept based on the DBI technique proposed by Frasier & Camps (2001) consists of simultaneous imaging of swaths to either side of the sub-satellite track allowing SAR interferometry of the ocean surface. The Wavemill antenna configuration (Buck *et al.* , 2011) basically consists of separating two antennas in both the across-track and along-track directions . This configuration allows direct measurements of 2D ocean surface currents by along track interferometry, providing two-dimensional maps of sea surface height over 100 km swaths with ∼10km spatial resolution and of order 5 cm accuracy (Gommenginger *et al.* , 2010).

1.5 Motivation and our approach

Although velocity fields derived from altimetric measurements are extensively used, distances between tracks are generally large, and that restricts the scales of the obtained velocity field below 100-150 km. In addition, the limited number of available altimeters leads to errors in the accurate location of oceanic currents (Pascual *et al.* , 2006), which limits the quantitative reconstruction of the velocity field using exclusively altimeters. To circumvent such a limitation, as seen in previous section, other sources of satellite data can be considered. New methodologies based on Surface Quasi-Geostrophic (SQG) theory allow to reconstruct ocean velocity fields from only a snapshot of SST.

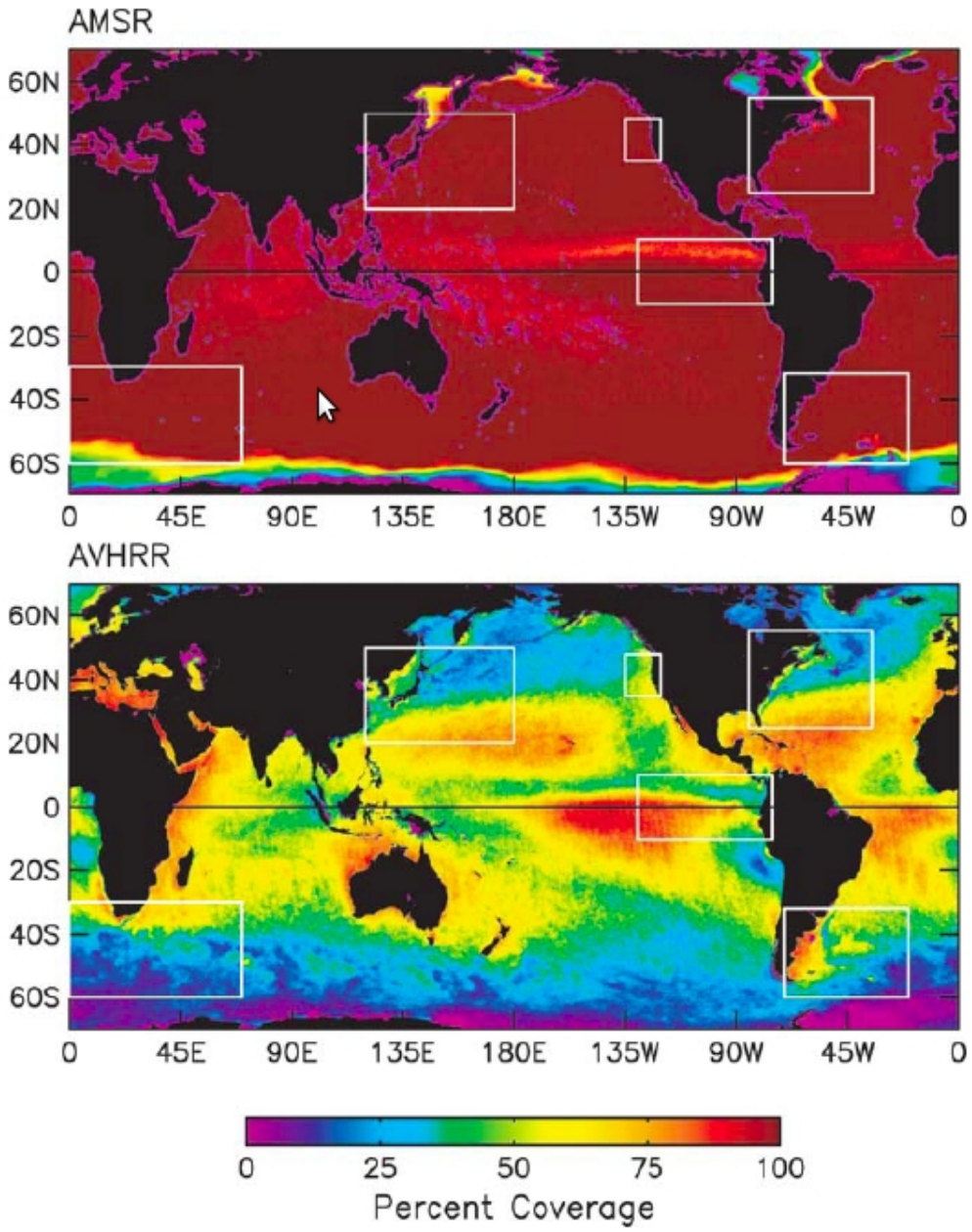

Figure 1.6: Percent coverage of SST measurements from (top) the AMSR-E and (bottom) the AVHRR in 3-day composite average maps during the 12 month period Oct 2002 through Sep 2003. (Chelton & Wentz, 2005).

Despite the capability to diagnose the velocity field from a single SST image significantly increases with these techniques, the operational use of SST images to derive surface currents at a global scale is still limited by the presence of cloud cover if infrared measurements are used. Low frequency microwave radiometers such as the Advanced Microwave Scanning Radiometer for EOS (AMSR-E), on the other hand, are very weakly depending upon cloud conditions and can provide global SST estimates. The improved global sampling of microwave measurements of SST by AMSR-E compared with IR measurements by the AVHRR is evident in Figure 1.6, which shows the percent coverage for each instrument in 3-day composite averages of SST over the 12-month period October 2002 through September 2003. The low coverage at high latitudes is attributable to ice cover. At lower latitudes, the prevalence of rain contamination reduced the AMSR-E coverage to 85% in the intertropical convergence zone near 10°N in the Eastern and central Pacific and to about 90% in some regions of the tropical Atlantic and Indian Oceans. Elsewhere, AMSR-E coverage in 3-day averages was near 100% everywhere. In comparison, AVHRR coverage in 3-day averages exceeds 75% in some regions of the Tropics and subtropics, but is less than 30% over much of the middle- and high-latitude ocean. This opens the door for using SST provided by microwave radiometers to investigate the capability to derive surface currents from SST images at a global scale, and to implement operational systems for the estimation of ocean velocities. In fact, it is possible to retrieve surface velocity fields from microwave SST measurements, under the appropriate environmental conditions, using an effective version of the SQG equations (Figure 1.7) (Isern-Fontanet *et al.* , 2006).

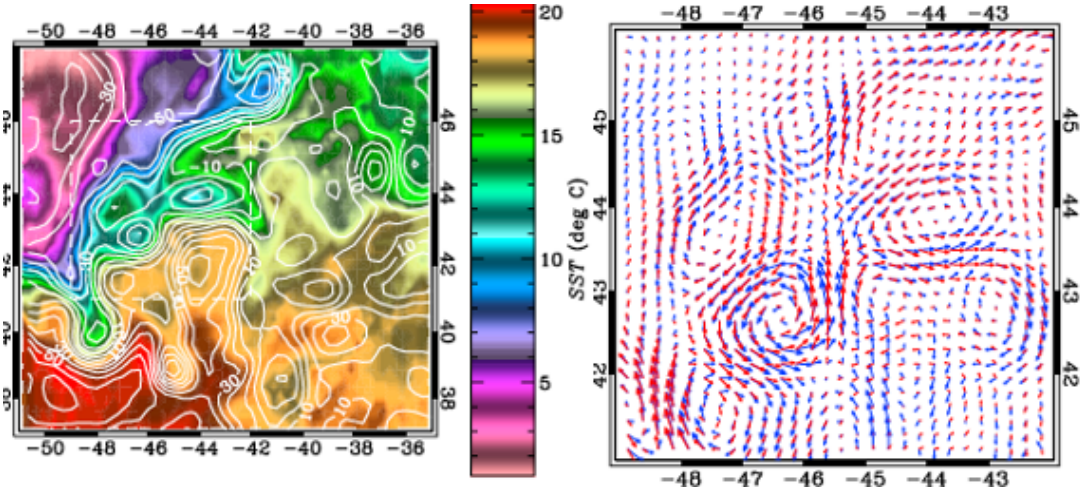

Figure 1.7: Potential use of MW to retrieve ocean currents. Left: AMSR-E SST image with superimposed contours of absolute dynamic height produced by Collect Localisation Satellites (CLS; Toulouse,France) and distribuited by AVISO. Right: Velocities derived from microwave SST (red) and altimeter (blue) observations in the area indicated by the white rectagle in the top figure. These data correspond to the area of 30°-48°N, 51°-35°W centered on January 5, 2005 (Isern-Fontanet *et al.* , 2006).

A key question is to which extent the SQG equations are a good model of the upper ocean dynamics. From a dynamic point of view, the spectra of the velocity field represents the distribution of kinetic energy (KE) within a range of spatial scales. Since the work of Kolmogorov

(1941), the properties of KE spectrum have been used to accept or reject the dynamical models of a turbulent flow. Indeed, Kolmogrov predicted that an homogeneous and isotropic three-dimensional (3D) turbulent flow should have a KE spectra with an inertial range scaling as $k^{-5/3}$ law, where k is the wavenumber. Besides, for a Quasi-Gesotrophic (QG) flow, Charney (1971) predicted an inverse energy cascade, from smaller to larger scales, with a KE spectrum that follows a k^{-3} law. The SQG approach, on the contrary, implies an energy spectrum that scales as $k^{-5/3}$ (Blumen, 1978). Furthermore, under the geostrophic balance, it is possible to relate the kinetic energy with the SSH (equation 1.3). Then the SSH spectrum, for the above models, should follow a k^{-5} law in the framework of QG theory, and a $k^{-11/3}$ law model in the case of SQG theory. Consequently, and directly deriving the KE spectrum from the SSH spectrum, the spectral slopes of SSH altimetric observations have been widely used to further investigate ocean surface dynamics (Le Traon *et al.* , 2008; Xu & Fu, 2011, 2012). Instead of following this approach to validate the SQG dynamical model, the relationship between SST and SSH can be investigated. For example, and without going into details (which are left for Chapter 2), assuming that the major contribution to the density anomaly is due to SST anamoly, the SQG theory relates SST and SSH observations by convolving SST with a kernel proportional to k^{-1}. This kernel is usually known as the transfer function in signal processing theory. However, recent studies have also revealed that the relationship between SST and SSH may differ from k^{-1} as the SQG theory predicts (Isern-Fontanet *et al.* , 2014).

This deviation from SQG theory may be a limitation, if the objective is the retrieval of the ocean surface currents from SST observations. To overcome this potential limitation the synergy between current SSH and SST measurements can be exploited. Figure 1.8 illustrates the synergy between along-track SSH and SST measurements. The observations shown in Figure 1.8 correspond to October 15, 2007. All the tracks of the different available altimeters for this date are also included in the top Figure. The 2D-SSH interpolated map, built up by combining all the along-track observations, is shown in the bottom Figure using black contours. This example evidences the sampling limitations of along-track observations due to the distance between tracks, e.g. the area between 56°W to 46°W is not sampled by any altimeter track. This results in a lower performance of the 2D altimery maps, which do not allocate properly the oceanic structures, e.g. the three eddies present in the area delimited by 56°W to 52°W longitude and 47°S to 45°S appear slightly shifted to the west in the SST images. It is more evident in the IR image. In addition, Figure 1.8 shows the better spatial resolution of IR images compared to MW images, and their limitation in measuring under the presence of clouds. A recent work (Isern-Fontanet *et al.* , 2014) has proposed exploiting the synergy between current SSH and SST measurements by combining the phase of SST, i.e. the relative position of structure, with the amplitude of SSH measurements, i.e. the distribution of energy among scales. Nevertheless, before attempting to combine SST images with along-track SSH measurements it is necessary to first identify the conditions and geographical areas where SST can be used to retrieve ocean currents. Indeed, the main limitation on the use of SST to derive currents using the above approach is that both two-dimensional SSH and SST have to be in phase. Recent studies based on numerical simulations have revealed that the phase shift between SST and SSH is minimum

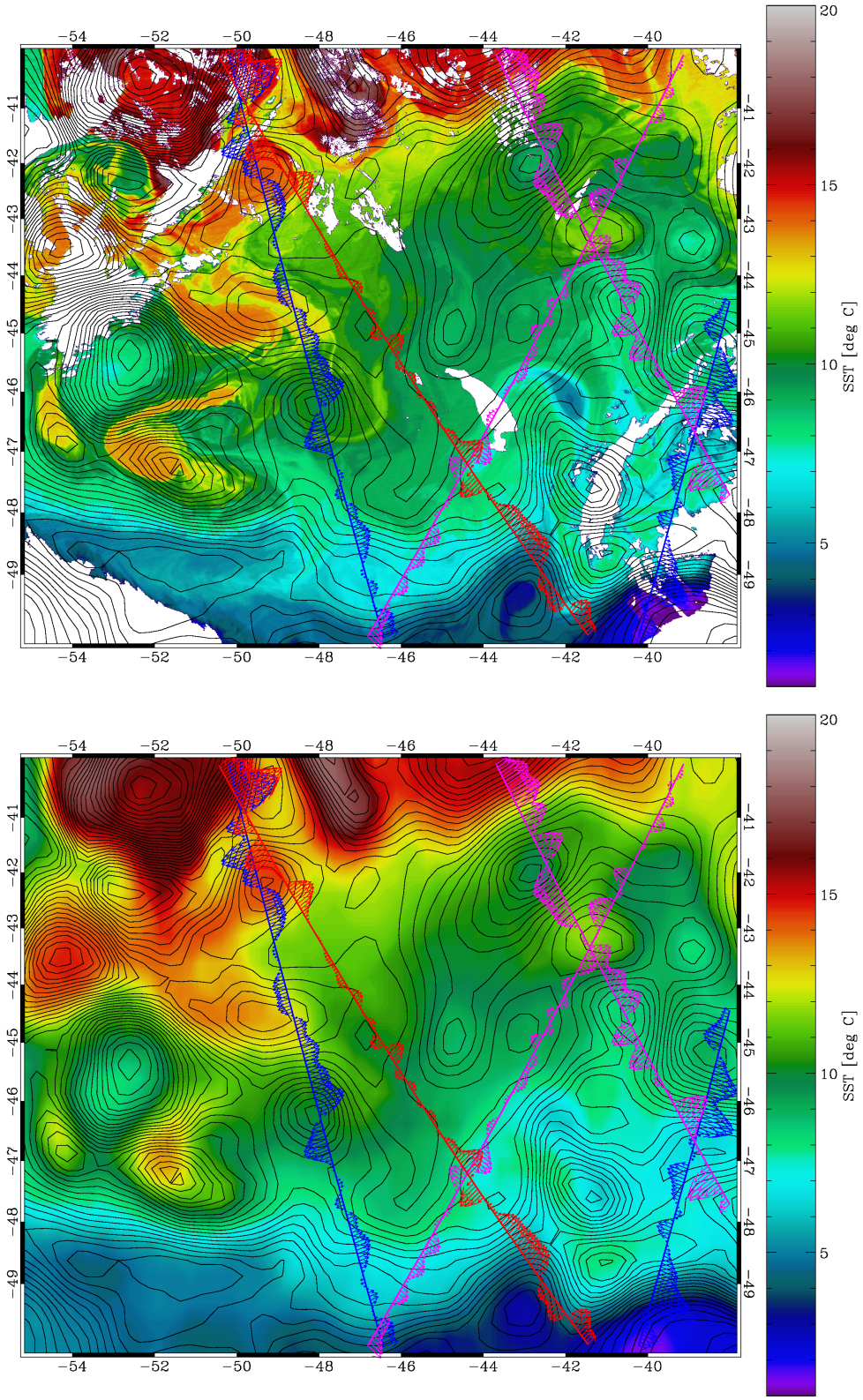

Figure 1.8: Synergy between SST and SSH measurements. Top: Infrared SST measured by MODIS, white mask corresponds to missing observations due to the presence of clouds. Bottom: MW SST measured by AMSR-E. Black contours, in both images, correspond to the simultaneous 2D SSH field built up by combining all available altimeters. The transects correspond to the velocities retrieved from along-track altimetry observations of: ERS-1 (blue), Jason1 (red) and GFO (violet). All observations correspond to the October 15, 2007. It is interesting to note that MODIS and AMSR-E provide simultaneous SST observations, since they are aboard of the same satellite, Aqua.

for deep Mixed Layers (ML) (Isern-Fontanet *et al.* , 2008, 2014). However, a global study on the matter has yet to be undertaken.

1.6 Objectives of the Thesis

This Ph.D. thesis aims at assesing the capability of SST microwave radiometers observations to retrieve global ocean surface currents and the improvement of its performance by exploiting its synergy with altimeter‘s observations. This main objective has been divided into three goals:

- Analysis of the validity of the SQG approach at a global scale using SST measurements provided by Microwave radiometers.
- Identify when it is possible to use the phase of SST to retrieve ocean surface currents.
- Assess the reconstruction of ocean surface currents by exploiting the synergy between SST microwave and altimetric observations.
- Analyze the relative distribution of energy among scales between SST and SSH observations.

1.7 Thesis outline

This Ph.D. Thesis is devoted to the retrieval of ocean surface currents from microwave radiometer remote sensing observations, and it is organized as follows:

Chapter 1 describes the motivation of this work and justifies its scientific and technological interest. The state-of-the-art of ocean surface current reconstruction from the space is also presented.

Chapter 2 sets the theoretical framework in which this Ph.D. Thesis is based on. The fundamental equations of the motion of the ocean are presented.

Chapter 3 reviews the theoretical background of remote sensing of the ocean using microwave radiometry and altimetry.

Chapter 4 describes the procedure and the data set used in the framework of this Ph.D. Thesis.

Chapter 5 assesses the capability of SST microwave radiometers to retrieve ocean surface currents at a global scale. The validity of SQG approach is assessed at a global scale and compared to an heuristic method that takes into account the synergy of SST microwaves and altimeter observations.

Chapter 6 performs a spectral analyis of the mean transfer function that relates SST and SSH observations and evaluates its performance for ocean surface current reconstruction.

Chapter 7 analyzes the temporal variability and the sensitivity of the spectral slope of the tranfer function that relates SST and SSH observations.

Chapter 8 summarizes and presents the conclusions that arises from the research conducted during this Ph.D. Thesis, remarks its original contributions, and presents suggestions for follow-on research.

Chapter 2

Theoretical Framework

The ocean is a turbulent flow governed by the equations of fluid dynamics, which are quite complex. Nevertheless, at the scales of interest to our work (see table tab:scale) L$\sim$ 100 km, U$\sim$ 10-100 cm/s Earth rotation plays a major role. This allows to simplify the equations to the so-called Quasi-Geostrophy approach. Here, the theoretical framework is reviewed in a quite informal approach, the reader interested in a more formal deduction of the equations is referred to Vallis (2006).

2.1 Equations of motion

2.1.1 Full set of equations

Time derivative: The Eulerian view

In solid-body mechanics one is normally concerned with the position and momentum of identifiable objects. The position and velocity of a particular object is then computed as a function of time by formulating equations of the general form:

$$\frac{\mathrm{d}x_i}{\mathrm{d}t} = F(\{x_i\}, t), \tag{2.1}$$

where $\{x_i\}$ is the set of positions and velocities of all the interacting objects and the operator F on the right-hand side is formulated using Newton‘s laws of motion.

In fluid dynamics such a procedure would lead to an analysis of fluid motions in terms of the positions and momenta of particular fluid elements, each identified by some label, which might simply be their position at an initial time. This is called a material point of view, because we are concerned to identifiable pieces of material; it is also called a *Lagrangian* view (after J.-L. Lagrange). However, from a practical point of view it would be extremely complicated to implement. Instead, for most problems we would like to know what the values of velocity, density and so on are at fixed points in space as time passes. For instance, in a weather forecast we might be interested on how warm it will be where we live, and if we are given that we do not

particularly care where a fluid parcel comes from. Since the fluid is a continuum, this knowledge is equivalent to knowing how the fields of the dynamical variables evolve in space and time, and this is often known as the field or *Eulerian* viewpoint (after L. Euler). This brings to evolution equations of the form:

$$\frac{\partial}{\partial t}\phi(x,y,z,t) = F, \tag{2.2}$$

where the field $\phi(x,y,z,t)$ is a dynamical variable (e.g., velocity, density, temperature) which gives the value at any point in space-time, and F is some operator to be determined from Newton's laws of motion and appropriate thermodynamic laws.

Let us suppose that a fluid is characterized by a velocity field $\vec{v}(\vec{x},t)$, and that it has another property ϕ. We are interested in the rate of change of this property ϕ of the fluid, and since it changes in time and space, the following chain can be used:

$$\delta\phi = \frac{\partial\phi}{\partial t}\delta t + \frac{\partial\phi}{\partial x}\delta x + \frac{\partial\phi}{\partial y}\delta y + \frac{\partial\phi}{\partial z}\delta z = \frac{\partial\phi}{\partial t}\delta t + \delta\vec{x}\cdot\nabla\phi. \tag{2.3}$$

This is true in general for any δt and $\delta\vec{x}$, etc. Thus the total time derivative is:

$$\frac{\mathrm{d}\phi}{\mathrm{d}t} = \frac{\delta\phi}{\delta t} + \frac{\mathrm{d}\vec{x}}{\mathrm{d}t}\cdot\nabla\phi, \tag{2.4}$$

where the second term on the right-hand side can be identified as the velocity of the fluid. Since the material derivative is so common, and to distinguish it from other derivatives, it is denoted by the operator $\mathrm{D}/\mathrm{D}t$. Thus, the material derivative of a field ϕ is

$$\frac{\mathrm{D}\phi}{\mathrm{D}t} = \frac{\partial\phi}{\partial t} + (\vec{v}\cdot\nabla)\phi, \tag{2.5}$$

where the brackets in the last term are helpful to keep in mind that $(\vec{v}\cdot\nabla)$ is an operator acting on the field ϕ. A similar expression can be obtained for a vector field $\vec{b}$:

$$\frac{\mathrm{D}\vec{b}}{\mathrm{D}t} = \frac{\partial\vec{b}}{\partial t} + (\vec{v}\cdot\nabla)\vec{b} \tag{2.6}$$

which in a cartesian coordinates system (x,y,z) could be decomposed in three equation similiar to (2.5), where the field ϕ should be replaced by each component of the vector $\vec{b}$. The second term on the right hand side, $(\vec{v}\cdot\nabla)$, is the so-called *advection term*, that gives the contribution of local change due to the velocity of the fluid.

The momentum equation

Newton's second law relates the change of the momentum of a fluid mass due to an applied force. The change in the Eulerian framework is

$$\frac{\mathrm{D}}{Dt}(\vec{v}) = \frac{\vec{F}}{m}, \tag{2.7}$$

where $\vec{F}$ is the force, m is the mass, and $\vec{v}$ is the velocity.

Motion of the ocean is mainly driven by four forces: pressure gradients, Coriolis force, gravity and viscosity. Without deriving the form of these forces, we can write the change of the momentum of a fluid per unit of mass due to an applied force as:

$$\frac{\partial \vec{v}}{\partial t} + \vec{v} \cdot \nabla \vec{v} = -\frac{1}{\rho} \nabla p - 2\vec{\Omega} \times \vec{v} + g\vec{e}_z + \nu \nabla^2 \vec{v} \tag{2.8}$$

where ρ is the density, p is the pressure, $\vec{\Omega}$ is the rotation rate of the Earth, and the term $2\vec{\Omega} \times \vec{v}$ stands for the Coriolis force, g is the gravity acceleration, $\vec{e}_z$ is the unit vector normal to ocean surface, and the last term $\nu \nabla^2 \vec{v}$ corresponds to the viscosity force.

The mass continuity equation

Since fluid density may change, and an equation that explicitly accounts for the flow of mass is one of the equations of motion of the fluid:

$$\frac{1}{\rho} \frac{\partial \rho}{\partial t} + \nabla \cdot \vec{v} = 0. \tag{2.9}$$

For an *incompressible* flow, that is a fluid with constant density, the mass continuity equation takes the form:

$$\nabla \cdot \vec{v} = 0. \tag{2.10}$$

The equation of state

In a three dimension system, the momentum and the mass continuity equations provide 4 equations, but 5 unknows (the three components of velocity field, pressure and density). Another equation is needed to close the equation group, the *equation of state* relates the various thermodynamic variables to each other. The conventional equation of state is an expression that relates temperature, pressure, composition (salinity), and density. It can be written as:

$$p = p(\rho, T, S), \tag{2.11}$$

where ρ is the density, T is the temperature and S is the salinity.

In the ocean both pressure and salinity affect the density of seawater (i.e. warmer waters are lighter and saltier waters are denser). However for many applications, it can be assumed that the density of seawater is independent of pressure (incompressible flow) and can be linearized, if changes in temperature and salinity are smaller, according to:

$$\rho = \rho_0[1 - \alpha_T(T - T_0) + \beta_S(S - S_0)], \tag{2.12}$$

whereas α_T is the coefficient of thermal expansion, and β_S is called, by analogy, the coefficient of saline contraction. Typical seawater values are $\rho_0 = 1028$ kg/m^3 , $T_0 = 10$°C$= 283$ K, $S_0 = 35$ psu, $\alpha_T = 1.7 \cdot 10^{-4}$ K^{-1} , and $\beta_S = 7.6 \cdot 10^{-4}$ psu^{-1}.

Since density depends on temperature and salinity, additional equations for these variables are necessary.

Equations for temperature and salinity

The equation governing temperature arises from conservation of energy. The principle of energy conservation, also known as the first law of thermodynamics, states that the internal energy gained by a parcel of matter is equal to the heat it receives minus the mechanical work it performs.

$$\frac{\partial T}{\partial t} + \vec{v} \cdot \nabla T = \dot{Q}, \tag{2.13}$$

where $\dot{Q}$ represents the external heating and diffusion.

Similarly, the equation for salinity is

$$\frac{\partial S}{\partial t} + \vec{v} \cdot \nabla S = S_{in} - S_{out}, \tag{2.14}$$

where S_{in} and S_{out} represents the salinity of the inner and outer flow, respectively.

2.1.2 Simplified equations

Boussinesq aproximation

The governing equations can be simplified if we exploit the smallness of density variations in many liquids. Indeed, density can be expressed as $\rho = \rho_0 + \delta\rho$, and it can be assumed that $\delta\rho/\rho_0 \ll 1$. The momentum equation can then be written as

$$\frac{\partial \vec{v}}{\partial t} + \vec{v} \cdot \nabla \vec{v} + 2\vec{\Omega} \times \vec{v} = -\nabla\phi + b\vec{k}, \tag{2.15}$$

where $\phi = \delta p/\rho_0$, and $b = -g\delta\rho/\rho_0$ is the buoyancy. Note that the term $g\delta\rho$ is not neglected, since there is no reason to believe it to be small ($\delta\rho$ may be small, but g is big). Equation (2.15) is the so-called momentum equation in the Boussinesq approximation, which ignores all variations of density of a fluid in the momentum equation, except when associated with the gravitational term.

Boussinesq approximation considers that the flow is incompressible, then the equation of the mass conservation takes the form of equation (2.10).

Primitive Equations

The primitive equations are a simplification of the Boussinesq equations that takes into account the following approximations:

- The *traditional approximation*: Coriolis terms in the horizontal momentum equations involving the vertical velocity are all neglected.

- The *hydrostatic approximation*: The hydrostatic approximation is a simplification of the equation governing the vertical component of the velocity. It takes into account that the pressure at any point in the ocean is due to the weight of the water above it. When vertical accelerations are small compared to the gravitational acceleration, the hydrostatic approximation is valid. In the vertical momentum equation the gravitational term is assumed to be balanced by the pressure gradient term, so that:

$$\frac{\partial p}{\partial z} = -\rho g. \tag{2.16}$$

The momentum equation in vector form is then,

$$\frac{\partial \vec{u}}{\partial t} + (\vec{v} \cdot \nabla)\vec{u} + \vec{f} \times \vec{u} = -\nabla_z p, \tag{2.17}$$

where $\vec{u}$ is the horizontal velocity vector $(u\vec{e}_x + v\vec{e}_y + 0\vec{e}_z)$, $\vec{f} = f\vec{e}_z = 2\Omega \sin\theta \vec{e}_z$, and $\vec{e}_z$ is the direction perpendicular to the plane. ∇_z is the horizontal gradient operator for z constant $(\partial/\partial x\vec{e}_x, \partial/\partial y\vec{e}_y)$.

Cartesian approximations: the tangent plane

The β-plane

The magnitude of the vertical component of rotation varies with latitude, and this has important dynamical consequences. This effect can be approximated by allowing the effective rotation vector to vary. Thus, for small variations in latitude, it can be decomposed as:

$$f = 2\Omega \sin\theta \approx 2\Omega \sin\theta_0 + 2\Omega \cos\theta_0(\theta - \theta_0), \tag{2.18}$$

then on the tangent plane the coriolis parameter varies as

$$f = f_0 + \beta y, \tag{2.19}$$

where $f_0 = 2\Omega \sin\theta_0$, $\beta = \partial f/\partial y = (2\Omega \cos\theta_0)/a$, and a is the radius of the Earth. This important approximation is known as the beta-plane, or β-plane, approximation. It captures the most important dynamical effects of sphericity, without complicating geometrical effects. Momentum equations (2.23), (2.24) and (2.25) will not be altered, save that f_0 is changed by $f_0 + \beta y$.

The f-plane

The rotation of the Earth plays an important role in many dynamic phenomena, however for phenomena on a scale smaller than the global, the use of spheric coordinates can be simplified. A tangent plane to the surface of the Earth is defined at a latitude θ_0 and the momentum equation for the flow is defined in that plane using a Cartesian coordinate (x, y, z) system.

$$\frac{\partial u}{\partial t} + (\vec{v}\cdot\nabla)u + 2\Omega_y w - 2\Omega_z v = -\frac{1}{\rho}\frac{\partial p}{\partial x}, \tag{2.20}$$

$$\frac{\partial v}{\partial t} + (\vec{v}\cdot\nabla)v + 2\Omega_z u = -\frac{1}{\rho}\frac{\partial p}{\partial y}, \tag{2.21}$$

$$\frac{\partial w}{\partial t} + (\vec{v}\cdot\nabla)w + 2(\Omega_x v - \Omega_y u) = -\frac{1}{\rho}\frac{\partial p}{\partial z} - g, \tag{2.22}$$

where now the rotation vector is fixed for a constant latitude θ_0 ($\vec{\Omega} = \Omega_x\vec{i} + \Omega_y\vec{j} + \Omega_z\vec{k}$ and $\Omega_x = 0$, $\Omega_y = \Omega\cos\theta_0$ and $\Omega_z = \Omega\sin\theta_0$). If the traditional approximation is made, and so the components of $\vec{\Omega}$ involving the vertical velocity w are ignored, then the momentun equations can be written as:

$$\frac{\partial u}{\partial t} + (\vec{v}\cdot\nabla)u - f_0 v = -\frac{1}{\rho}\frac{\partial p}{\partial x} \tag{2.23}$$

$$\frac{\partial v}{\partial t} + (\vec{v}\cdot\nabla)v - f_0 u = -\frac{1}{\rho}\frac{\partial p}{\partial y} \tag{2.24}$$

$$\frac{\partial w}{\partial t} + (\vec{v}\cdot\nabla)w = -\frac{1}{\rho}\frac{\partial p}{\partial z} - g \tag{2.25}$$

2.2 Quasi-Geostrophic approximation

Large scale flow in the ocean is characterized by an approximate balance in the vertical direction between the pressure gradient and gravity (hydrostatic balance), and in the horizontal dirction between the pressure gradient and the Coriolis force (geostrophic balance). These balances are exploited to simplify the primitive equations, and thereby obtain various sets of simplified equations, the so-called quasi-geostrophic equations.

Simplifying the equations in this way relies first on scaling the equations. The idea is that the scales of the variables are chosen, typically either on some a priori basis or by using observations as a guide. Then the variables are normalized to their typical scale (dimensionless), and we attempt to derive a set of equations that is simpler than the original set, but that consistently describes the motion of the chosen scale. The scale of variables are denoted with capital letters; thus if L is the typical length of the described motion, and U a typical velocity scale, then:

$$(x, y) \sim L \text{ or } \mathcal{O}(L), \tag{2.26}$$

$$(u, v) \sim U \text{ or } \mathcal{O}(U), \tag{2.27}$$

Thus, using the typical scale for each variable they can be written as a function of a dimensionless variable that will be denoted with *

$$(x, y) = (Lx^*, Ly^*) \quad (u, v) = (Uu^*, Uv^*), \tag{2.28}$$

where the terms with * are $\mathcal{O}(1)$ by definition. The terms in the momentum then scale as:

$$\underbrace{\frac{\partial \vec{u}}{\partial t}}_{\frac{U}{T}} + \underbrace{(\vec{v}\cdot\nabla)\vec{u}}_{\frac{U^2}{L}} + \underbrace{\vec{f}\times\vec{u}}_{fU} = \underbrace{-\frac{1}{\rho}\nabla_z p}_{\frac{\mathcal{P}}{L}}, \tag{2.29}$$

where ∇_z operator acts in the x, y plane and $\mathcal{P}$ is the amplitude of the variations in the surface displacement.

The ratio of the advective term $(\vec{v}\cdot\nabla)\vec{u}$ to the rotational term $\vec{f}\times\vec{u}$ in the momentum equation is the Rossby number

$$\mathrm{Ro} = \frac{U^2/L}{fU} = \frac{U}{fL}. \tag{2.30}$$

If the Rossby number is small then rotation effects are important, and as the values in table 2.1 indicate, this is the case for large-scale flow in the ocean. If the Rossby number is sufficiently small in equation (2.29), then the rotation term will dominate the non-linear advection term, and the only term which can then balance the rotation term is the pressure term, and therefore:

$$\vec{f}\times\vec{u} \sim -\frac{1}{\rho}\nabla_z p. \tag{2.31}$$

This balance is known as geostrophic balance, and the geostrophic velocities are then defined as:

$$u_g \equiv -\frac{1}{f\rho}\frac{\partial p}{\partial y} \qquad v_g \equiv \frac{1}{f\rho}\frac{\partial p}{\partial x}. \tag{2.32}$$

At this point it is interesting to note, that for an horizontal non-divergent flow ($\nabla\cdot\vec{u} = 0$):

$$\frac{\partial u}{\partial x} + \frac{\partial v}{\partial y} = 0, \tag{2.33}$$

it may exist a function ψ, such as:

$$u = -\frac{\partial \psi}{\partial y}, \qquad v = \frac{\partial \psi}{\partial x} \tag{2.34}$$

This function is the so-called stream function of the flow, which for a constant Coriolis parameter f_0 , a constant density ρ_0, and comparing (2.34) with (2.32), it can be written as:

$$\psi = \frac{p}{f_0\rho_0}. \tag{2.35}$$

In Cartesian coordinates de Coriollis parameter can be expressed as:

$$\vec{f} = f_0\vec{e_z} + \beta y\vec{e_z}. \tag{2.36}$$

The variation of the Coriolis parameter is assumed to be small. This is a key difference between the quasi-geostrophic system and the planetary geostrophic system, and in particular the term βy is assumed to be approximately the size of the relative vorticity, and much smaller than f_0,

Table 2.1: Scales of mesoscale flow in ocean. The choices given are representative of mesoscale eddying motion in the ocean.

Variable	Scaling Symbol	Meaning	Value
(x, y)	L	Horizontal length	50-500 km
t	T	Timescale	100-10 days
(u, v)	U	Horizontal velocity	0.1 m s^{-1}
	Ro	Rossby number, U/fL	0.1

thus

$$\beta y = \frac{U}{L}, \qquad \beta = \frac{U}{L^2}, \tag{2.37}$$

and so a $\mathcal{O}(1)$ dimensionless β paremeter is defined as:

$$\beta^* = \frac{\beta L^2}{U} = \frac{\beta L}{\mathrm{Ro} f_0}, \tag{2.38}$$

from this the corresponding dimensionless version of f is

$$f^* = f_0^* + \mathrm{Ro}\beta^* y^*, \tag{2.39}$$

where $f^* = f/f_0$ and $f_0^* = 1$.

Now, if the dependent variables are expanded in an asymptotic series in Rossby number:

$$\vec{u}^* = \vec{u}_0^* + \mathrm{Ro}\vec{u}_1^* + \ldots, \quad \phi^* = \phi_0^* + \mathrm{Ro}\phi_1^* + \ldots, \quad b^* = b_0^* + \mathrm{Ro}b_1^* + \ldots, \tag{2.40}$$

and then substituted in the equations of motion, the lower order $\mathcal{O}(1)$ momentum equation gives the geostrophic balance:

$$\vec{f_0^*} \times \vec{v_0^*} = -\nabla_z \phi_0^*. \tag{2.41}$$

At next order $\mathcal{O}(\mathrm{Ro})$ the momentum equation is

$$\frac{\partial \vec{v_0^*}}{\partial t} + \vec{v_0^*} \cdot \nabla \vec{v_0^*} + \beta^* y^* \vec{e}_z \times \vec{v_0^*} + \vec{f^*} \times \vec{v_1^*} = -\nabla_z \phi_1^* \tag{2.42}$$

Manipulating equation (2.42), basically by computing its rotational, taking into account the mass conservation, and the thermodinamic equations, and by defining the stream fuction (2.34), the equations that describe the motion of the ocean are simplified to the following expressions:

$$\frac{DQ}{Dt} = 0, \tag{2.43}$$

$$\nabla_z^2 \psi + \frac{\partial}{\partial z}\left(\frac{f_0^2}{N^2}\frac{\partial \psi}{\partial z}\right) + f_0 = q, \tag{2.44}$$

where the quantity q is the potential vorticity, $Q = q - f_0$ is known as the quasi-geostrophic

potential vorticity anomaly and N is the Brunt-Väisälä frequency

$$N^2 = -\frac{g}{\rho_0}\frac{\partial \rho}{\partial z} \tag{2.45}$$

N gives an idea of the vertical stability of a fluid parcel. If $N^2 > 0$ then a parcel displaced upward is heavier than its surroundings, and thus experiences a restoring force; the density profile is said to be stable, and N is the frequency at which the fluid parcel oscillates. If $N^2 < 0$, the density profile is unstable, and the parcel continues to ascend and convection occurs.

The derivation of the QG approximation allows to reduce the Navier-Stokes equations, which are a six coupled non-linear partial differential equations with seven unkowns (u, v, w, T, p, ρ, S) to a single second-order partial differential equation with a single unknown (ψ). The other dynamic parameters that describe the motion of the ocean are obtained once the unkonwn ψ is determined, as:

1. Velocity: $\vec{u} = \vec{e}_z \times \nabla\psi$
2. Realtive vorticity: $\zeta = \nabla^2\psi$
3. Perturbation pressure: $\phi = f_0\psi$
4. Perturbation buoyancy: $b' = f_0\partial\psi/\partial z$

2.3 Solution of the Quasi-Geostrophy equation

The principle of invertibility of the potential vorticity (PV, Hoskins *et al.* , 1985) allows the diagnosis of the 3D dynamics of a balanced flow from the knowledge of PV in the ocean interior and density on the vertical boundaries. If we assume that the flow is in Quasi-Geostrophic (QG) equilibrium, the problem consists of inverting the equation

$$\nabla_z^2\psi + \frac{\partial}{\partial z}\left(\frac{f_0^2}{N^2}\frac{\partial\psi}{\partial z}\right) = Q, \tag{2.46}$$

where $Q(\vec{x}, z)$ is the PV anomaly, $\psi(\vec{x}, z)$ the stream function of the flow, f_0 the local Coriolis frequency, $N(z)$ the Brunt-Väisälä frequency, $\vec{x} = (x, y)$ and $\nabla_z \equiv (\partial_x, \partial_y)$.

This problem can be split into two solutions as proposed by Bretherton (1966) and Lapeyre & Klein (2006a). An interior solution $\psi_i(\vec{x}, z)$ obtained assuming zero surface buoyancy and non-zero interior PV, i.e. $b_s = 0$ and $Q \neq 0$ and a surface solution $\psi_s(\vec{x}, z)$ obtained assuming non-zero surface buoyancy and zero interior PV, i.e. $b_s \neq 0$ and $Q = 0$. Then, the total solution to the inversion problem is the sum of both contributions, i.e.

$$\psi(\vec{x}, z) = \psi_s(\vec{x}, z) + \psi_i(\vec{x}, z), \tag{2.47}$$

where the subscripts '$_s$' and '$_i$' stand for surface and interior fields, respectively. To sum up, the solution to 2.46 can be split into two diferent problems with diferent boundary conditions that

can be derived from the hydrostratic equation. For the surface problem, it would lead to invert:

$$\nabla^2\psi_s + \frac{\partial}{\partial z}\left(\frac{f_0^2}{N^2}\frac{\partial\psi_s}{\partial z}\right) = 0, \tag{2.48}$$

with surface boundary condition

$$f_0 \left.\frac{\partial\psi_s}{\partial z}\right|_s = b_s. \tag{2.49}$$

For interior problem the expression to invert is

$$\nabla^2\psi_i + \frac{\partial}{\partial z}\left(\frac{f_0^2}{N^2}\frac{\partial\psi_i}{\partial z}\right) = Q, \tag{2.50}$$

with surface boundary condition

$$f_0 \left.\frac{\partial\psi_i}{\partial z}\right|_s = 0. \tag{2.51}$$

The bottom boundary condition is the same for both solutions, for an infinite vertical domain it will be expressed as:

$$\lim_{z\to-\infty}\frac{\partial\psi_{i,s}}{\partial z} = 0, \tag{2.52}$$

and for a finite H depth as:

$$\left.\frac{\partial\psi_{i,s}}{\partial z}\right|_{-H} = 0. \tag{2.53}$$

2.3.1 Surface Quasi-Geostrophy

Assuming a constant stratification ($N(z) = N_0$), and introducing the Prandtl ratio n as (Tulloch & Smith, 2006)

$$n_0 = \frac{N_0}{f_0}, \tag{2.54}$$

the surface-forced problem can be written in the Fourier space as

$$-k^2\hat{\psi}_s + \frac{1}{n_0^2}\frac{\partial^2\hat{\psi}_s}{\partial z^2} = 0, \tag{2.55}$$

where $\hat{}$ stands for the Fourier transform, $\vec{k} = (k_x, k_y)$ is the wavevector and $k = \|\vec{k}\|$ is the modulus of the wavevector. Then, the solution of equations (2.49), (2.52) and (2.55) in the horizontal Fourier transform domain reduces to:

$$\hat{\psi}_s(\vec{k}, z) = \frac{\hat{b}_s(\vec{k})}{n_0 f_0 k}\exp\left(n_0 k z\right). \tag{2.56}$$

Equation (2.56) is termed the Surface Quasi-Geostrophy (SQG) system (Held *et al.* , 1995). Although the scope of this Ph.D. thesis is the retrieval of the ocean surface velocity field, it is worth to highlight that the relation (2.56) allows to retrieve the surface contribution to the vertical velocity field from a surface field. Actually, it implies that the subsurface field resembles a low-pass filtered version of the surface field. Note that small scales (large wavenumbers) decay

more rapidly than the large scales.

This is the most simple solution, but other solutions arise just by changing the boundary conditions. For example, if a finite domain depth (H) is considered instead of an semi-infinite domain like in equation (2.56), it would lead to expression

$$\hat{\psi}_s(\vec{k}, z) = \frac{\hat{b}_s}{n_0 f_0 k} \frac{\cosh(n_0[H+z]k)}{\sinh(n_0 k H)}, \tag{2.57}$$

(Tulloch & Smith, 2006) from which the classical SQG solution (2.56) is recovered in the limit of an infinite depth (Held *et al.* , 1995).

In the two previous solutions, equations (2.56) and (2.57), the SQG formalism was applied considering that the Brunt-Väisälä frequency was constant. However, this is not a realistic assumption in the ocean, where the stratification is surface intensified. LaCasce (2012) derived the SQG solutions with exponential stratificantion and compared the results to those obtained with constant stratification. The near-surface SQG velocities with an exponential stratification were weaker than the classical SQG with constant stratification, and they decay more rapidly with depth.

2.3.2 Total solution

Lapeyre & Klein (2006a) showed that the large-scale forcing in density and PV can lead to the property that the interior PV mesoscale anomalies are correlated to the surface buoyancy anomalies in the upper ocean. In that case, the PV anomaly can be separated as

$$Q(\vec{x}, z) \approx \xi(z) b_s(\vec{x}), \tag{2.58}$$

with $\xi(z)$ being a function that specifies the amplitude of PV anomaly. This result was also confirmed by Isern-Fontanet *et al.* (2014), who computed linear correlation between PV below the mixed layer (ML) and sea surface buoyancy using an Ocean General Circulation Model (OGCM) in the Mediterranean. Results (see Figure 2.1) revealed that correlations where higher for deep ML than for shallow ML.

The remarkable consequence is that the interior contribution to the total solution of the PV inversion problem can also be retrieved from the surface buoyancy b_s, once the function $\xi(z)$ is determined. Then, for a finite depth H with constant stratification $N_0 \equiv f_0 n_0$ the interior solution is

$$\hat{\psi}_i(\vec{k}, z) = -\frac{\xi(z)}{f_0 \left(k^2 + \frac{1}{n_0^2 H^2}\right)} \hat{b}_s(\vec{k}), \tag{2.59}$$

(e.g. Klein *et al.* , 2011), which corresponds to the baroclinic mode. At long scales, this solution tends to a constant, while at short scales it behaves as $\hat{\psi}_i(k, 0) \sim k^{-2}$. Whereas, the surface solution for a finite depth H with constant stratification equation (2.57), discussed in previous section, at short scales (large k) is similar to the classical SQG solution $\hat{\psi}_s(k, 0) \sim k^{-1}$, equation (2.56), while at large scales (small k) it is steeper, $\hat{\psi}_s(k, 0) \sim k^{-2}$.

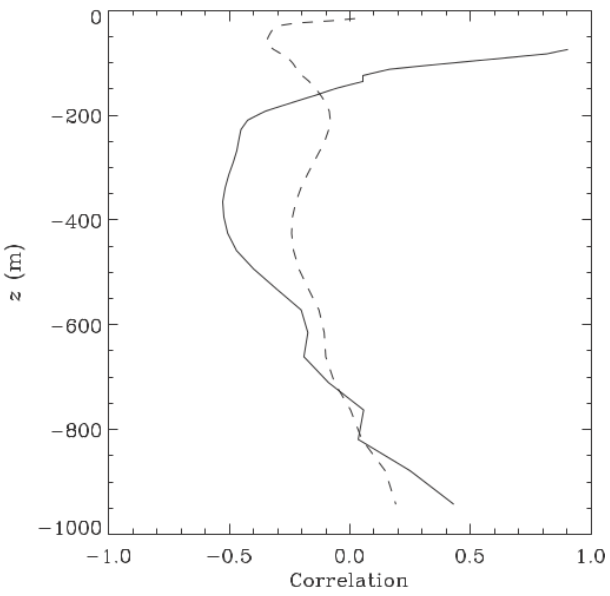

Figure 2.1: Correlation between PV and b_s: Mean spatial correlation between surface buoyancy anomaly and PV anomaly in the Levantine Basin for ML deeper than 70m (solid line) and ML shallower than 20 m (dash line) (Isern-Fontanet *et al.* , 2014).

The relative dominance of each solution can be separated by a critical wavelength that depends on the large scale properties of the flow. (Lapeyre, 2009; Klein *et al.* , 2011).

Effective SQG

Lapeyre & Klein (2006a) showed the contribution of the interior stream function ψ_i and the surface stream function ψ_s are non-orthogonal in the first 500 m. One important consequence is that the total solution can be approximated by an effective SQG solution (eSQG), obtained from the substitution of n_0 in the denominator of equation (2.56) by a value n_e that takes into account both, the interior and surface the solutions. This value is obtained from the comparison with independent observations (Isern-Fontanet *et al.* , 2008).

The eSQG model allows the reconstruction of geostrophic velocities in the upper oceanic layers from only one snapshot of the surface density field b_s and two parameters: the Brunt-Väisälä frequency n_0 that determines the vertical attenuation of surface fields and depends on the large-scale properties of the flow, and the effective Prandtl ratio (n_e) that, determines the energy level at the ocean surfaces and depends on the mesoscale.

2.4 Observable Variables

In the previous sections, the dynamical framework that can be used to model upper layers of the ocean has been developed. Nevertheless, some variables involved, e.g PV, cannot be observed from satellites. However, it has been seen that the ocean surface velocity field can be retrieved from the stream function, equation (2.32), assuming that the ocean is in geostrophic equilibrium.

Dynamic topography η provides a direct estimation of the stream-function at the surface:

$$\psi(\vec{x}) = \frac{\mathrm{g}}{f_0}\eta(\vec{x}), \tag{2.60}$$

where g is the gravity constant and f_0 is the Coriolis parameter. Dynamic topography can be retrieved from Sea Surface Height (SSH) measurements adquired by radar altimeters on board satellites. Actually, ocean surface velocity are routinely and extensively retrieved using this technique.

In addition, considering the Quasi-Geostrophic equilibrium, the stream function can be estimated from the surface buoyancy equation (2.56). It is important to highlight that buoyancy itself is not an observable variable from space. However, if the ocean is assumed to be an incompressible flow, the density anomaly can be linearized as a function of the temperature and the salinity, equation (2.12), and the surface buoyancy can be computed as:

$$b_s(\vec{x}) = -\frac{\mathrm{g}}{\rho_0}\left(-\alpha_T T_s(\vec{x}) + \beta_S S_s(\vec{x})\right), \tag{2.61}$$

where g is the gravity constant, α_T is the coefficient of thermal expansion, β_S is the coefficient of saline contraction, and T_s and S_s are Sea Surface Temperarture (SST) and Sea Surface Salinity (SSS), respectively, both variables can be observed from space. Whereas SST has been measured from space for the past 2 decades, measurements of SSS from space are relatively new. Nowadays there are two active missions that provide synoptic measurements of SSS: SMOS mission from ESA, launched on November 2009, and Aquarius mission from NASA launched on June 2011. Thus, systematic SSS observations were not available the period wherein this thesis is focused on: from 2002 to 2005. It is important to recall that during this period there were available up to four different altimeters, which enhances the proper location of oceanic structures (Pascual *et al.* , 2006). Nevertheless, it can be assumed that the contribution to density anomaly is dominated by SST, and then, this field can be used to compute surface buoyancy as:

$$b_s(\vec{x}) \simeq \frac{\mathrm{g}\alpha_T}{\rho_0}T_s(\vec{x}). \tag{2.62}$$

A relevant question is to which extent equation (2.62) is valid. In general, salinity anomalies possess similar structures as temperature anomalies due to the advection by geostrophic eddies that create sharp gradients of both fields in the same regions (Klein *et al.* , 1998). In-situ observations (Ferrari & Rudnick, 2000) show a tendency for salinity and density gradiets to be aligned and pointing into opposite directions. Therefore temperature fronts would tend to be compensated by salinity fronts. This implies that equation 2.62 would overstimate density gradients. In fact, Isern-Fontanet *et al.* (2008) studied the alignment and compensation in denstity between salinity and temperature by means of the complex ratio given by Ferrari & Paparella (2003)

$$r = \frac{\alpha_T}{\beta_S}\frac{\partial_x T_s + i\partial_y T_s}{\partial_x S_s + i\partial_y S_s}. \tag{2.63}$$

The phase θ_r of the complex ratio r quantifies the degree of alignment of salinity and tempera-

ture gradients and the magnitude of their relative strength. Then, thermohaline compensation (cancellation of temperature gradients by salinity gradients in density) corresponds to $|r| = 1$ and $\theta_r = 180°$. Results showed, that in general, there is a strong alignment between salinity and temperature gradients with a mean phase slightly lower than 180°. The magnitude of $\langle r \rangle$ showed a mean value between 1.41 and 2.47 for all the studied areas in the North Atlantic ocean. This indicates that in general there is a dominance of temperature. It was also confirmed by the adjustment of the effective parameter n_e. The effective Prandtl ratio was estimated from buoyancy n_b, and from SST n_T. Thus, n_b accounts for the contribution of the interior PV in the surface field (section 2.3.2), whereas n_T accounts in addition for the salinity contribution. Results revealed that the magnitude of n_b was quite close to n_0, while the magnitude of n_T is larger than the values of n_0 and n_b. This confirms that the compensation between temperature and salinity is important and that salinity distribution has a stronger effect on the magnitude of surface fields than the interior PV.

2.5 Transfer function

In engineering, a transfer function is a mathematical representation to describe the input and the ouput of a black box models. In signal processing the term is normally used to refer to linear, time-invariant systems. Note that, in a linear time-invariant system, the frequency response to a given input does not depend on time. Given an input $\hat{X}(i\omega)$, the ouput signal $\hat{Y}(i\omega)$ will be always the same. Therefore, the frequency response of the system describes the change in amplitude and phase of the input system for every frequency ω, in terms of gain:

$$F(\omega) = \frac{|\hat{Y}|}{|\hat{X}|} = |\hat{H}(i\omega)|, \tag{2.64}$$

where i is the complex unit and phase shift:

$$\Delta\theta(\omega) = \arg(\hat{Y}) - \arg(\hat{X}) = \arg(\hat{H}(i\omega)). \tag{2.65}$$

Therefore, the transfer function can be written in the frequency Fourier domain as:

$$\hat{H}(i\omega) = F(\omega)e^{i\Delta\theta(\omega)}. \tag{2.66}$$

The solutions to the PV invertion problem, that were discussed previously in this chapter, could be seen as a response of a system whose input signal is the surface buoyancy. Then, the total solution to the PV inversion problem has the form:

$$\hat{\psi}(\vec{k}, z) = F_b(k, z)\hat{b}_s(\vec{k}, z). \tag{2.67}$$

It is important to hightlight that the transfer function $F_b(k, z)$ does not depend on the wavevector $\vec{k}$, but on its modulus k.

Since the geostrophic streamfunction at the ocean surface is proportional to the dynamic

topography (2.60), the transfer function for surface buoyancy can be calculated as

$$F_b(k) = \frac{g}{f_0}\frac{\langle|\hat{\eta}|\rangle_k}{\langle|\hat{b}_s|\rangle_k}, \tag{2.68}$$

where angle brackets with a subscript k indicate that the average is taken over those wavevectors with the same modulus. In the case of the classical SQG solution, the transfer function at the surface takes the form:

$$F_b(k) = \frac{1}{n_0 f_0 k}. \tag{2.69}$$

Equation (2.67) implies that the streamfunction, and the surface buoyancy are in phase. However, previous studies have shown that there may exist a phase shift between the streamfunction and surface buoyancy (Isern-Fontanet *et al.* , 2008; Hausmann & Czaja, 2012). To take this into accunt, the phase shift $\Delta\theta_b(\vec{k})$ is introduced in (2.67) for ocean surface ($z = 0$) (Isern-Fontanet *et al.* , 2014). Then,

$$\hat{\psi}_s(\vec{k}) = F_b(k)e^{i\Delta\theta_b(\vec{k})}\hat{b}_s(\vec{k}, z) \tag{2.70}$$

The phase shift can be obtained as (Isern-Fontanet *et al.* , 2014):

$$\Delta\theta_b(\vec{k}) = \arccos\left[\frac{\Re(\hat{\eta}\hat{b}_s^*)}{|\hat{\eta}||\hat{b}_s|}\right] \tag{2.71}$$

Similarly, a transfer function amplitude $F_T(k)$ and a phase shift $\Delta\theta_T(\vec{k})$ can be defined for the SST anomaly. Since, as it was discussed in previous section, SST can be used to retrieve the streamfunction, assuming that the variability of density anomaly is dominated by SST anomaly. Therefore, equation (2.70) becomes

$$\hat{\psi}(\vec{k}) = F_T(k)e^{i\Delta\theta_T(\vec{k})}\hat{T}_s(\vec{k}). \tag{2.72}$$

Note that under this assumption $F_T(k) \propto F_b(k)$, and $\Delta\theta_T(\vec{k}) = \Delta\theta_b(\vec{k})$.

It should be pointed out, that all the solutions to the invertibility of the PV problem discussed in this chapter imply that the surface buoyancy and the streamfunction are in phase. Before attempting to retrieve ocean surface current from SST measurements it is needed to study under which circumstances the streamfunction and the surface buoyancy are in phase, or referring to remote sensed observations, when SST and SSH are in phase. This is one of the main contributions of this Ph.D. thesis.

Chapter 3

Remote Sensing of the Ocean

3.1 Microwave Radiometers

The Earth continuously receives electromagnetic radiation coming mainly from the Sun. Part of this radiation is scattered and/or absorbed by the atmosphere, and the other part is transmitted to the Earth‘s surface. At the Earth‘s surface, part of this energy is absorbed, and part is scattered outwards. The energy absorbed is then transformed into thermal energy, which leads to a temperature increase until the thermodynamic equilibrium is reached. According to Thermodynamics, At this state, all media (gases, liquids, solids and plasma) radiate energy to keep the energy balance. Radiometry is the field of science devoted to the measurement of the electromagnetic radiation. Radiometers are instruments capable of measuring with high accuracy the power emitted by a body. The basic concepts and principles of microwave radiometry are reviewed in this section.

3.1.1 Principles

Blackbody radiation

All bodies at a non-zero absolute physical temperature radiate electromagnetic energy. The increase of radiated energy is proportional to the temperature increase. A blackbody is defined as an idealized, perfectly opaque material that absorbs all the incident radiation at all frequencies, reflecting none. Also, a blackbody is a perfect emitter, since otherwise its temperature would indefinitely increase. Therefore, when a black-body reaches the thermodynamic equilibrium, it radiates all the absorbed energy omnidirectionally. The blackbody spectral brightness B_{bb} is given by the Planck‘s radiation law (Planck, 1901)

$$B_{bb} = \frac{2hf^3}{c^2} \frac{1}{e^{\frac{hf}{k_B T}} - 1}, \tag{3.1}$$

where f is the frequency in Hz, $h = 6.63 \cdot 10^{-34}$ Js is the Planck‘s constant, $k_B = 1.38 \cdot 10^{-23}$ J/K is the Boltzmann‘s, $c = 3 \cdot 10^8$ m/s is the speed of light and T is the temperature in K.

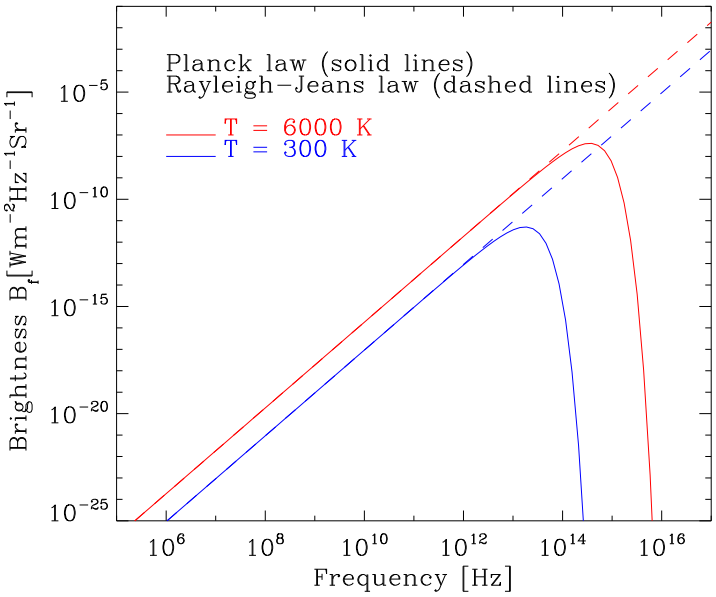

Figure 3.1: Comparison of Planck radiation law with its low-frequency approximation (Rayleigh-Jeans law) for T =300 K and T =6000 K

At microwave frequencies, $hf/k_BT \ll 1$, the Taylor's approximation can be used to simplify equation (3.1), which leads to Rayleigh-Jeans law:

$$B_{bb} = \frac{2f^2 k_B T}{c^2} = \frac{2k_B T}{\lambda^2}, \tag{3.2}$$

where $\lambda = c/f$ is the wavelength. The Rayleigh-Jeans law is widely used in microwave radiometry since it is mathematically simpler than Planck's law. In the case of black body emission from a surface at 300 K, typical of the ocean, the Rayleigh-Jeans aproximation differs by less than 1% from the precise emission according to Planck's law, as long as $f < 117$ GHz. Figure 3.1 shows a graphical comparison of Planck's law and the Rayleigh-Jeans law for T =300 K ($\sim$ the Ocean's temperature), and T =6000 K ($\sim$ the Sun's surface temperature).

Gray body radiation

Real materials or gray bodies do not behave as blackbodies: they do not absorb all the energy incident upon them, and its emission is lower than that of perfect blackbodies. It is therefore convenient to define a microwave brightness temperature $T_B(\theta, \phi)$, so that the brightness of a gray body can be expressed, similarly to equation 3.2 , as

$$B(\theta, \phi) \equiv \frac{2k_B}{\lambda^2} T_B(\theta, \phi), \tag{3.3}$$

where θ and ϕ are the zenith and the azimuth angles defining the direction of propagation of the microwave energy flux. $T_B(\theta, \phi)$ is the temperature of the black-body source that would

generate the measured brightness $B(\theta, \phi)$; it is not the real temperature of the object, but an effective temperature. The brightness of gray bodies relative to that of blackbodies at the same physical temperature is called the emissivity $e(\theta, \phi)$,

$$e(\theta, \phi) = \frac{B(\theta, \phi)}{B_{bb}} = \frac{T_B(\theta, \phi)}{T} \tag{3.4}$$

Note that, since real materials emit less than a blackbody, $B(\theta, \phi) \leqslant B_{bb}$, and therefore $0 \leqslant e(\theta, \phi) \leqslant 1$. The emissivity equals 0 in the case of a perfect reflector (e.g. a lossless metal), and 1 in the case of a perfect absorber, a blackbody. Thus, the brightness temperature $T_B(\theta, \phi)$ of a material is always smaller than, or equal to, its physical temperature T. Through e the brightness becomes dependent on the dielectric properties of the emitting surface, as well as its temperature. It also varies with the viewing direction relative to the surface normal.

Table 3.1: Recent and current series of microwave radiometers

Sensor acronym	Platform(s)	Agency	Dates (for series)	Center frequency [GHz]	Main Data Products
TMI (TRMM Microwave Imager)	TRMM	NASA/JAXA	Sep 1987 - present	10.97 19.4 21.3 37 85.5	SST Wind Speed Water vapor Cloud liq. water Rain rate
AMSR-E (Advanced Microwave Scanning Radiometer)	Aqua	JAXA/NASA	May 2002- Oct 2011	6.95 10.65 18.7 23.8 36.5 89	SST Wind Speed Atm. water vapour Cloud liq. water Rain rate Sea ice
Windsat	Coriolis	U.S. DoD	Jan 2003- present	6.8 10.7 18.7 23.8 37	SST wind speed and direction
MIRAS (Microwave Imaging Radiometer with Aperture Synthesis	SMOS	ESA	Nov 2009- present	1.4	SSS Soil Moisture
Aquarius	Aquarius/SAC-D	NASA/CONAE	Jun 2011- present	1.4	SSS
AMSR2 Advanced Microwave Scanning radiometer	GCOM-W1	JAXA	May 2012- present	6.03 7.3 10.65 18.7 23.8 36.5 89	SST Wind Speed Atm. water vapour Cloud liq. water Rain rate Sea ice

Sea Surface emission

The emissivity e for a plane surface of complex relative dielectric constant ϵ is different for different polarisation states. Figure 3.2 illustrates the general shape of the variation of e_H and e_V with viewing angle. The subscripts H and V refer to horizontal and vertical polarization states, respectively. The exact direction of the Brewster angle at which e_V peaks (where the reflection is zero) will vary with the value of ϵ, the complex dielectric constant for seawater.

Lane & Saxton (1952) expressed this as:

$$\epsilon = \epsilon_\infty + \frac{\epsilon_s - \epsilon_\infty}{1 + i2\pi f t_r} - i\frac{\sigma}{2\pi f \epsilon_0} \tag{3.5}$$

where i is the imaginary number $\sqrt{-1}$, ϵ_∞ and ϵ_s are the dielectric constant at very high and zero frequency respectively; t_r is the relaxation time; σ is the ionic conductivity; and $\epsilon_0 = 8.854{\cdot}10^{-12}$ F m^{-1} is the permittivity of free space. ϵ_s, t_r and σ are functions of the temperature and salinity of seawater, and have been evaluated experimentally by Klein & Swift (1977). A more recent determination by Wentz & Meissner (2000) uses improved estimates of some of the variables, including more reliable salinity dependence.

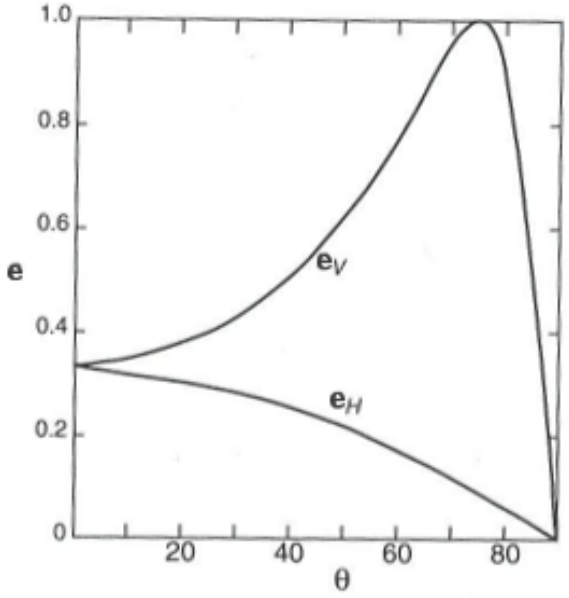

Figure 3.2: Typical shape of the variation with viewing angle, θ, of horizontally and vertically polarised emissitivity, e_H and e_V. Based on(Robinson, 2004).

The consequent dependence of e on T means that the apparently linear relationship expressed in equation 3.2 between microwave brightness and actual SST does not happen in practice. The dependence of e on salinity provides a potential opportunity for using microwave radiometry to detect remotely the salinity of the surface layer of the sea. The dependence on viewing angle makes it difficult to calculate precisely the radiation emitted from a rough sea surface. Given the wide field of view (FOV) of microwave radiometers the measured radiation is integrated over an area having dimensions typically oon the order of tens of kilometres. Thus, it is the statistical distribution of θ for all surface facets in the FOV which affects the measured brightness. This in turn must depend on the sea surface slope statistics, which are controlled by the wind stress. For this reason the brightness contains information on the surface wind, and it is possible to obtain remotely measurements of this magnitude.

3.1.2 Effect of the atmosphere

A microwave radiometer receives sea surface emissions through the atmosphere. As it travels, the radiation is absorbed and scattered by water vapor, molecular oxygen, and small cloud droplets, and is scattered by rain drops. The signals received by a radiometer also include the thermal atmospheric emissions of that travel upwards from the sea surface to the instrument. Then, the brightness temperature $T_B(\theta, \phi)$ as viewed by the antenna from a zenith, and azimuth angles θ and ϕ contains contributions from several sources (see Figure 3.3):

- the emission of sea surface at temperature of T_s
- the incoming radiation from cold space at a temperature T_c (taken to be 2.7 K)
- and the emission by the atmosphere itself (T_{atmU} and T_{atmD})

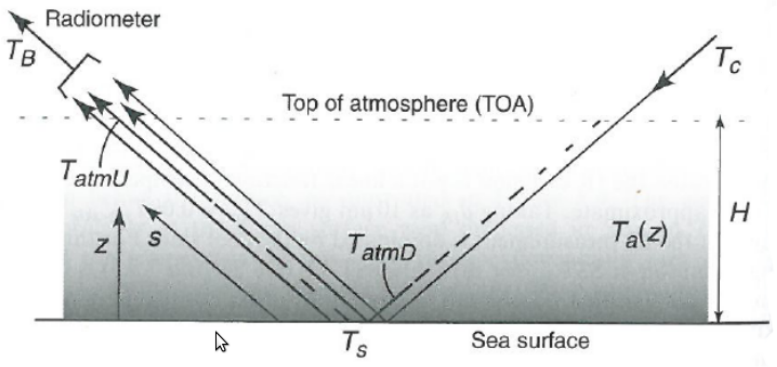

Figure 3.3: Contributions to the microwave radiation received at the sensor (Robinson, 2004)

The contribution of the atmosphere can be evaluated using the radiative transfer equation (RTE) Goody & Y.L-Young (1998), simplified by the Rayleigh-Jeans approximation:

$$\frac{\partial T_B}{\partial s} = -\alpha(s)[T_B(s) - T_a(s)], \tag{3.6}$$

where $\alpha(s)$ is the atmospheric absorption coefficient, and T_a is the actual atmospheric temperature, both of which are dependent on position, s. Figure 3.3 illustrates the domain in which Equation 3.6 is to be solved, with T_s and T_c contributing to the boundary conditions. Following Wentz & Meissner (2000) this yields to:

$$T_B = T_{atmU} + \tau_H \epsilon T_S + \tau R(1 + \Omega)(T_{atmD} + \tau_H T_c), \tag{3.7}$$

where τ_H is the transmittance through the atmosphere along path s, between the ground and a height H above which the influence of any residual atmosphere is no longer felt. T_{atmU} and T_{atmD} are the contributions of the atmospheric emission integrated through the whole atmosphere, representing respectively the upward radiation at the top of atmosphere and the downward radiation incident on the sea. For a smooth surface the reflectivity R in the viewing direction, is related to the emissivity by $R = 1 - e$. However, if the surface is rough, the scatering

results in additional energy being reflected, and this is accounted for in the term Ω. For calm conditions $\Omega = 0$, but at frequencies between 7 GHz and 37 GHz it increases with wind speed to a value of 0.14 for V-polarisation and 0.25 for H-polarisation (Meissner & Wentz, 2002).

To fully evaluate $\alpha(s)$ a detailed knowledge of the atmospheric profile of temperature, water vapour and cloud liquid water against pressure is required. The absoption of electromagnetic radiation by these processes depends on frequency, and it makes that corrections for the atmospheric attenuation can make use of multispectral measurements (Meissner & Wentz, 2002).

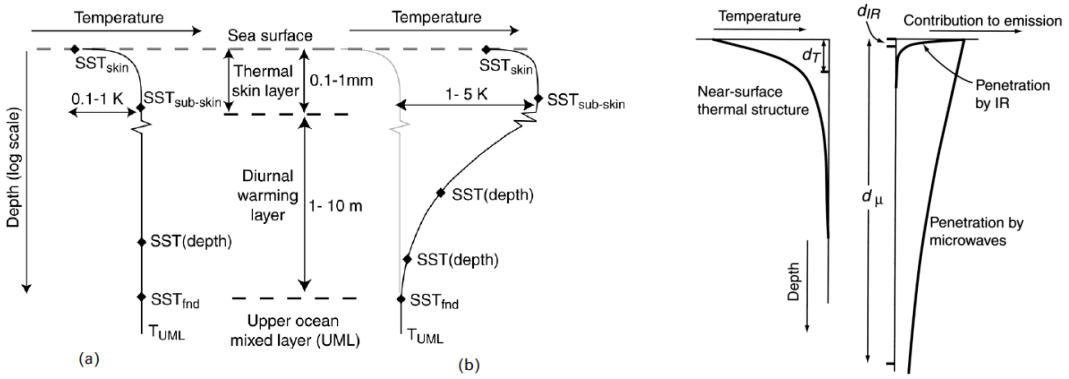

Figure 3.4: Characteristic SST profile. Left: Schematic diagram showing characteristic temperature profiles at the sea surface for (a) night time conditions or daytime with moderate to strong winds and (b) day time calm to light wind conditions and direct solar heating . Right: The approximate relation between the supposed skin-layer thermal structure of the sea and the penetration depth of microwave and IR radiation (Robinson, 2004)

3.1.3 Geophysical interpretation

In the surface layer, water temperature varies diurnally with the changes in solar radiation caused by the Earth‘s rotation. In the daytime, the solar shortwave radiation is absorbed in the surface layer, thereby increasing its temperature. This diurnal variation is confined to the surface within a depth of a few meters. A very thin cool layer exists immediately underneath the sea surface. The depth of this ”skin layer“ (e.g. Saunders, 1967) is usually less than 1 mm, with the temperature at the top of the layer usually a few tenths of a degree lower than that of the underlying waters. Donlon *et al.* (2002) noted that this skin layer exists in both the daytime and nighttime, even with weak wind conditions (< 6 ms^{-1}). Formation of the skin layer can be explained as follows: Shortwave radiation entering the ocean is absorbed to depths that can reach 100 m in very clear water, while net longwave radiation is emitted from a depth of about 10 μm (Figure 3.4). The penetration depth of infrared waves is quite shallow, ranging from 4μm ($\lambda = 12\mu$m) to 80 μm ($\lambda = 3.7\mu$m). In the microwave frequency range used for remote sensing of SST ($4 - 10$ GHz), the penetration depth is slightly proportional to the temperature and is less than 0.5 cm.

To coordinate global multi-sensor SST products for scientific and operational use, the Global Ocean Data Assimilation Experiment (GODAE) Science Team has defined five kinds of SST: interface SST (SST_{int}), skin SST (SST_{skin}), subskin SST ($SST_{subskin}$), SST at depth (SST_{depth}), and foundation SST (SST_{fnd}) (Donlon *et al.* , 2007). SST_{int} is a theoretical value that represents the precise air-sea interface and that cannot be measured by our current technology. SST_{skin} is defined as the thermal radiometric skin temperature, which is measured using an infrared radiometer operating in the 10-12 μm bands. This SST represents the actual temperature of the water in the thermal skin layer. $SST_{subskin}$ represents the temperature at the base of the thermal skin layer, which can be well approximated by microwave radiometer measurements in the 4-10 GHz bands. Foundation SST, SST_{fnd}, is determined as the surface layer temperature free from diurnal variation and equal to $SST_{subskin}$ if the diurnal signal is absent.

3.1.4 Spatial sampling

The angular resolution, $\Delta\theta_{-3dB}$, of a MW radiometer is normally defined as the half-power width of the antenna main beam. While this depends on the detailed antenna design and is related to the power pattern, $G(\theta, \phi)$, it is always constrained by the wavelenght of radiation and the antenna aperture diameter, D, to approximately satisfy $\Delta\theta_{-3dB} = \lambda/D_a$ radians. For a satellite at altitude H_{sat}, and a nadir looking antenna, this results in a ground resolution cell or beam footprint with a linear dimension:

$$d = \Delta\theta_{-3dB} H_{sat} = \lambda H_{sat}/D_a = cH_{sat}/Df. \tag{3.8}$$

Thus for a given footprint size d the required antenna size is $D_a = \lambda H_{sat}/d$.

Figure 3.5 shows an example of a typical scanning multi-frequency MW radiometer. One main advantge of this type of scanning is that the viewing angle is constant. The size of the footprint for each sample varies considerably between frequencies, according to (3.8), being the smallest for the highest frequency. The smallest footprint constrains both the sampling rate along the scan, and the scanning rate, which must complete one scan cycle in the time taken by the satellite to travel a distance equal to the linear dimensioin of the highest frequency footprint.

Since all frequency bands use the same parabolic reflector and scanning system, larger footprints must oversample in the along-track direction. If they sample at the same rate as the highest frequency band, then they also oversample along the scan trajectory. The oversampling can be used to reduce the noise by averaging.

3.2 Radar Altimeters

Satellite radar altimeters are active microwave sensors that determine the distance from the satellite to a target surface by measuring the satellite-to-surface round-trip time of a radar pulse. However, this is not the only measurement made in the process, and a lot of other information can be extracted from altimetry.

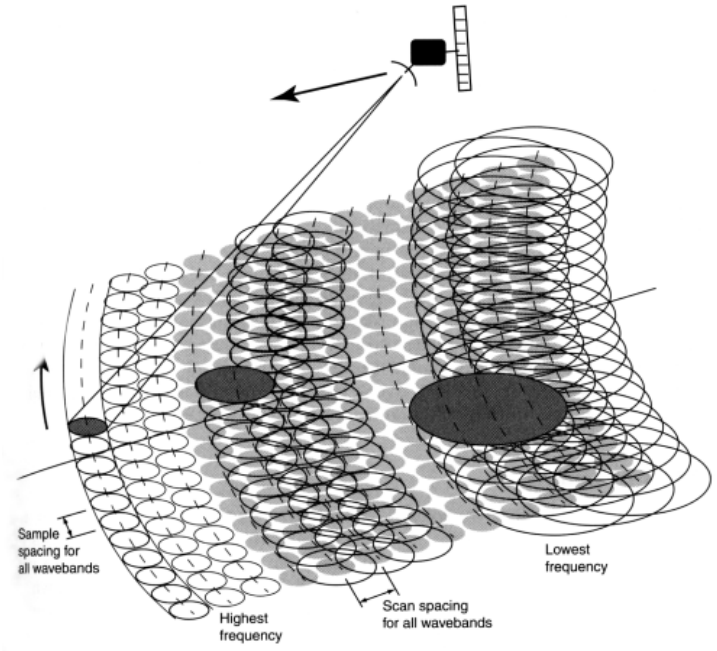

Figure 3.5: Spatial sampling of MW radiometer. The scanning and sampling patterns of different frequency channels of a typical scanning MW radiometer. The different wavebands normally scan teh same line together, and have been separated here only for clarity (Robinson, 2004).

3.2.1 Principles of satellite altimetry

The basic concept of a radar altimeter is very simple. A pulse of microwave radiation is emitted in the direction of the sea surface, and the time taken for it to return, t, is measured. Knowing the speed of the light, c, and the transit time, t, the distance, R_{alt}, between the sensor and the sea to be calculated. In fact the distance should properly be expressed as:

$$R_{alt} = \frac{ct}{2} - \sum_{i=1} \Delta R_i, \tag{3.9}$$

where the ΔR_i terms represent the corrections for delays in the round trip travel time. Some of them allow for the effect of the atmosphere on the radar transmission speed, and others accommodate the influence of sea state on the round trip travel time of the pulse. Figure 3.6 illustrates how a pulse of duration τ is returned from a perfectly flat sea surface. Because the pulse expands as a spherical shell the first encounter with the sea occurs at the point closest to the sensor (i.es., immediately below it at range R) at time $t = R/c$ measured from when the pulse was emitted. The illuminated area is at first a point and then a circle whose area grows linearly with time. At time $t = R/c + \tau$, the trailing edge of the pulse reaches the sub-satellite point and from then, the illuminated area becomes an annulus. While the radius of the annulus continues to grow with time, the illuminated area now remains constant. The first reflected signal arrives back at the altimeter at time $t = 2R/c$ and its power grows linearly from zero until at time $T = 2R/c + \tau$ it levels out when the illuminated area becomes constant.

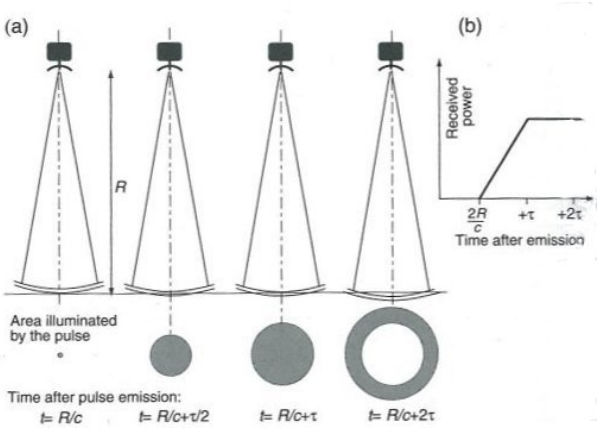

Figure 3.6: Principles of satellite altimetry. Interaction of a pulse of duration τ with a smooth sea surface. (a) the illuminated surface geomtry. (b) The resulting power of the reflected pulse (Robinson, 2004).

In practice the sea is not perfectly flat and is often very rough. The consequence is that the growth of the reflected signal received at the sensor is drawn out over time. It starts rising earlier but reaches its maximum later. However, the time from the mid-point of the pulse emission to the mid-point of the rising edge of the return still corresponds to the two-way travel time to the mean sea surface level. Thus, the altimeter is able to average out the effect of the ocean waves.

3.2.2 Effect of atmosphere

Free electrons are present in the Earth's ionosphere. As with water vapor, these electrons delay the return of the radar pulse from the altimeter and thus affect the accuracy of sea-level measurements. The correction term, ΔR_i, in equation (3.9) must account for all the processes which slow down the microwave transmission between the satellite and the sea surface below the speed of light. There are two places where the refraction of microwave radiation occurs: the troposphere, where the effect of atmospheric gases are combined into the dry tropospheric correction while the effects of water as vapour and liquid droplets in clouds are expressed in the wet tropospheric correction; and the ionosphere where free electrons alter the dielectric properties of the upper atmosphere.

Dry tropospheric correction

The dry tropospheric correction, ΔR_{dry}, depends on the total mass in the path of the microwave pulse. The vertical distribution of gases is well known and the horizontal variability is represented by the distribution of atmospheric preassure, p_a, at sea leavel, in the following expression:

$$\Delta R_{dry} = 2.2277 \cdot 10^{-5}(1 + 0.0026 \cos 2\Phi)p_a. \tag{3.10}$$

The correction term ΔR_{dry} is expressed in meters, and the pressure in Pascals. The term including latitude, Φ, is to allow for the variation of gravity with latitude which modifies the

relation between p_a, and the air mass. The size of ΔR_{dry} is about 2.3 m, but the only uncertainty attached to the correction comes from the estimate of p_a, where an error of 5mbar corresponds to 1cm in range. Sea level pressure for altimetry processing is obtained from the 6-h operational weather analyses of the European Centre for Medium-range Weather Forescasting (ECMWMF).

Wet tropospheric correction

The wet tropospheric correction, ΔR_{wet}, counts for the effect of the liquid water content of clouds, which is typically less than 1 cm except for convective cumulus clouds and a much larger contribution from water vapour, varying typically from 10 cm at mid-latitudes to 30 cm in the tropics. The correction for each of these has been developed as a linear function of the integrated columnar liquid water and water vapour respectively. Modern altimeters rely on simultaneous measurements with a microwave radiometer on board the same satellite. For ERS and Envisat altimeters this is a two channel (23.8 and 36.5 GHz) radiometer with a 20 km field of view (FOV) , yielding an estimate of ΔR_{wet} to accuracy of about 2 cm (Eymard *et al.* , 1996). For T/P a three channel (18.0 GHz, 21.0 GHz, and 37.0 GHz) radiometer is used and an accuracy of ΔR_{wet} better than 1.1 cm is achieved (Ruf *et al.* , 1994) even under the worst conditions of variable clouds and wind.

Rain causes problems for the altimeter, not so much because of the additional delay which is small, but because patchy cells of heavy rain cause localised attenuation of the return signal, distorting the waveform and producing errors in the tracking algorithm. When rainfall is flagged the corresponding altimeter observation is eliminated from the estimate of sea surface height. The presence of rain is identified from a combination of the passive microwave radiometer data and the differential attenuation between the two frequency channels of the altimeter (Quartly *et al.* , 1996).

Ionosheric correction

Free electrons produced by solar ionising radiation alter the dielectric properties of the medium, resulting in frequency dispersion of the microwave signal. The effect is strongest at altitudes between 250 km and 400 km. Although the typical magnitude of ΔR_{ion} does not exceed 20 cm for a 13.5 GHz altimeter, the problem is that the effect is highly variable. It is therefore essential to find a direct way to estimate ionosphere delay on a point-by-point basis.

The answer is to utilise the property of the ionosphere dispersion, which causes the delay for a radar pulse to vary inversely with the square of the frequency. If the time delay for a radar pulse to vary inversely with the square of the frequency. If a dual-frequency atimeter is used with bands at frequencies f_1 and f_2, then the channels will measure different ranges R_1 and R_2 instead of the true value R (when other delaying factors have been corrected). The ranges are thus related by:

$$\frac{R_1 - R}{R_2 - R} = \frac{f_2^2}{f_1^2}, \tag{3.11}$$

and so,

$$R = \frac{R_1 f_1^2 - R_2 f_2^2}{f_1^2 - f_2^2}. \tag{3.12}$$

The error resulting from the two-channel approach is about 1.1 cm (Imel, 1994) caused largely by the sensitivity of the differential method to the combined sensor noise of both channels, and this can be reduced by along-track low-pass filtering of the ionospheric correction.

3.2.3 Geophysical interpretation

Sea surface height (h_{raw}) is the distance between the free surface of the sea and an arbitrary reference surface: the reference ellipsoid (the Earth's centre or a rough approximation of the Earth's surface). Sea surface height can be computed from the satellite's position on orbit (H_{sat}) with respect to the reference ellipsoid and the satellite-to-surface range R_{alt}, equation (3.9), calculated by measuring the time taken by the signal to make the round trip (see Figure 3.7).

$$h_{raw} = H_{sat} - R_{alt}. \tag{3.13}$$

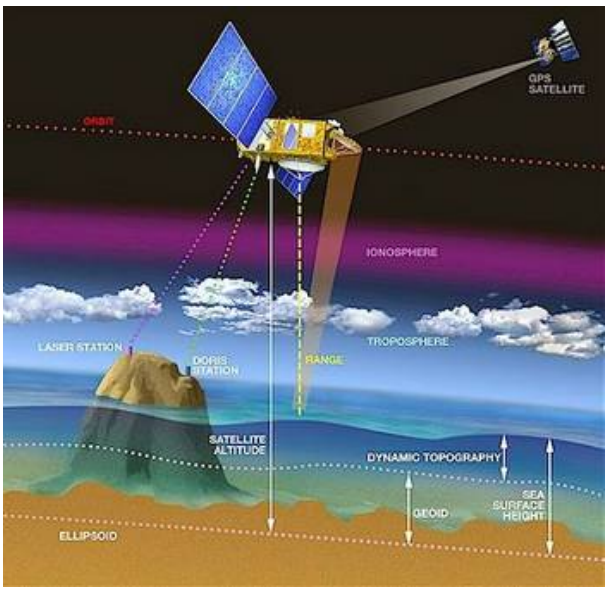

Figure 3.7: Schema of SSH measurements from altimeters. Altimeters emit signals to Earth, and receive the echo from the sea surface, after its reflection. The sea height is represented by the distance satellite - surface and the satellite's position relative to an arbitrary reference surface (the reference ellipsoid)(Credits CNES). `http://www.aviso.altimetry.fr/en/techniques/altimetry/principle/basic-principle.html` Last visit: April 10, 2015.

Several physical factors contribute to sea surface height. The first is the distribution of gravity over the Earth, as represented by the geoid above the reference ellipsoid (h_{geoid}) in Figure 3.7. Another factor that contributes to sea surface height is the instantaneous tidal displacement

(h_{tide}) of the sea surface relative to the contribution of Earth tide. A third local response of the ocean is due to the atmospheric pressure distribution h_{atm}. This is the so-called inverse barometer effect, whereby sea level changes of approximately ± 1 cm are observed to take place in response to variation in air pressure of ± 1 mbar. The remaining factor is the sea surface height associated with the motion of the sea, called the ocean dynamic topography (η)[1] . This is a property of most relevance from an oceanographic point of view, since it contains information about ocean circulation:

$$\eta = H_{sat} - R_{alt} - h_{geoid} - h_{tide} - h_{atm}, \tag{3.14}$$

h_{tide} and h_{atm} are known with a reasonable accuracy and can be corrected for. However this is not the case for the geoid height. There are a number of ways to deal with the lack of an independent geoid of sufficient precision. The first is to note that the geoid is essentially time invariant. Therefore the time varying part of $\eta + h_{geoid}$ is the same to the time varying part of η and it can be isolated provided the satellite occupies an orbit for which the ground track periodically repeats itself at intervals of several days. Thus h_{geoid} can be neglected by computing the sea level anamoly (SLA) $h^{'}$, once h_{tide} and h_{atm} have been corrected (see section 4.2):

$$\eta^{'} = h - \langle h \rangle. \tag{3.15}$$

3.2.4 Spatial sampling

The temporal and space resolution depend entirely on the exact orbit repeat cycle of the satellite. For ocean applications an orbit having a regularly repeating ground track is essential to resolve tidal fluctuations and to measure dynamic variability, especially in the absence of an independent geoid.

Starting by considering the altitude of the satellite, low orbits present some advantages. They require less power for the same signal-to-noise performance as a higher orbit, and the footprint is also smaller, giving finer spatial resolution. On the contrary, a satellite in a high orbit is less afected by the atmosphere. Between 800 and 1300 km it reduces by an order of magnitude, there is less variability and so orbit model errors are considerably lower. In addition, a higher orbit enables the ground station to intercept more overpasses. Thus, the advantages of height are principally related to the reduction of satellite orbit error which is one of the crucial factors in improving altimeter performance. For a dedicated altimetry mission this consideration weights more than the benefits of a low orbit and an altitude over 1300 km is advised.

Once the height is fixed, so is the revisit time of the satellite. The choice of repeat cycle also controls the spatial-sampling interval. The longer the revisit interval the finer the spatial-grid. Thus the nearly 10-day repeat cycle of T/P gives a 316 km track separation at the equator, for a 66° inclined orbit, whereas the 3-day repeat cycle of Seasat's 72° orbit gives a track separation

[1]In this thesis ocean dynamic topography is denoted with η and for the sake of simplicity using the acronym SSH. In order to avoid confusing the reader, in this section we do not use the acronym for the real sea surface height h_{raw}

of about 800 km. Figure 3.8 compares those orbits over the North Atlantic. The first of these is more appropiate for the characteristic length and timescale of the geostrophic processes to be observed by the altimeter. The spatial sampling is a better match to the typical first mode baroclinic Rossby radius which defines the smallest size of geostrophic eddies, and these tend to have a lifetime of at least ten days. The 3-day repeat is more likely to miss smaller features.

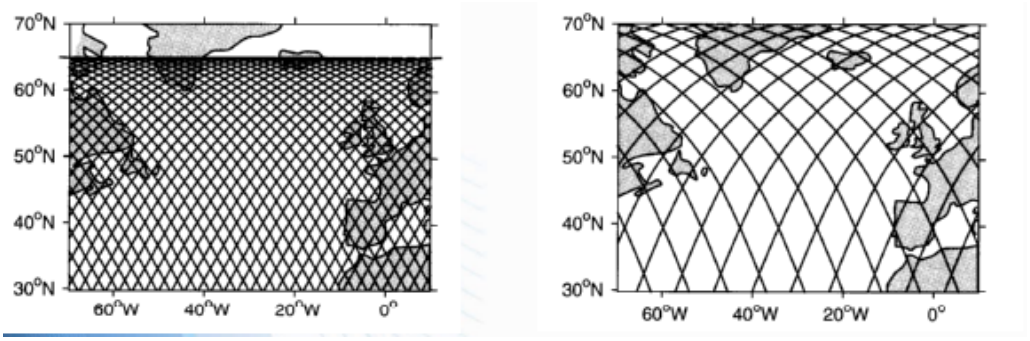

Figure 3.8: Spatial distribution of the ground track over the North Atlantic for an orbit with: (Left) repeat pattern of about 10 days and an inclination of 66° (Right) repeat pattern of 3 days at an inclination of 72°(Robinson, 2004).

In practice, the optimum solution for an overall Earth-observing system would be to use a combination of more than one altimeter on platforms with different types of orbit. It is worth to highlight that measurements of SSH along-track can only provide the across-track component of the velocity. To circumvent this limitation, SSH data are typically interpolated onto a geographical grid and composited over the period or an exact repeat cycle, to produce "images" which are comparable to global SST products, in terms of resolution (see section 4.2.2). Pascual *et al.* (2006) showed that the representation of the mesoscale variability in the Global Ocean can be improved when data from four different altimeter are used (see Figure 1.5).

Table 3.2: Recent and current series of altimeters

Altimeter	**Agency**	**Dates**	**Height [km]**	**Orbit**	**SSHA r.m.s accuracy [cm]**
TOPEX/Poseidon	NASA/CNES	1992-2005	1336	9.92 day repeat non-Sun-synchronous	2-3
Poseidon-2 on Jason-1	NASA/CNES	2011-2005	1336	9.92 day repeat non-Sun-synchronous	$\simeq$2
Poseidon-3 on Jason-2	NOAA/NASA CNES/Eumetsat	2008-present	1336	9.92 day repeat non-Sun-synchronous	$\simeq$2
Radar altimeter on ERS-1	ESA	1991-2000	780	3 and 35 day repeat Sun-synchronous	$\simeq$5-6
RA on ERS-2	ESA	1995-2003	780	35 day repeat Sun-synchronous	$\simeq$5-6
RA2 on Evisat	ESA	2002-present	800	35 day repeat Sun-synchronous	3
Geosat	U.S Navy	1986-1989	800	17.05 day repeat Sun-synchronous	10 reanalysis
Geosat Follow-on	U.S Navy	2000-2008	800	17.05 day repeat Sun-synchronous	$\simeq$10 reanalysis

Chapter 4

Data and procedure

This chapter describes the data set used in this Ph.D. thesis to reconstruct ocean surface velocities. In particular, time average (3 days) SST microwave fields from AMSR-E sensor and daily SSH fields were used. The study focuses from October 1, 2002 to May 18, 2005, because there were four altimeters available, which improves the location of ocean currents (Pascual *et al.* , 2006) (see Figure 1.5).

The following sections provide a general description of the remote sensors and algorithms used to retrieve the data set. Understanding the physical basis of the algorithms is necessary to identify the characteristic features and sources of errors of the information derived from them.

4.1 AMSR-E

The Advanced Microwave Scanning Radiometer for the Earth Observing System (AMSR-E) orbits the Earth on the EOS Aqua satellite in a sunsynchronous, near-polar orbit and has sampled the global ocean with 89% coverage each day and 98% coverage every 2 days from 1 June 2002 to 4 October 2011, when the AMSR-E antenna stopped spinning.

AMSR-E is a total-power microwave radiometer for six frequency bands from 6.9 GHz to 89 GHz (see table 4.1). Each frequency band is monitored by vertical and horizontal polarized wave. The aperture diameter of AMSR-E antenna is 1.6 m, and its spatial resolution is about 5 km in the 89 GHz band, and about 60 km in the 6.9 GHz band of the largest wavelength. It conically scanned and kept a nominal angle of incidence of 55° on the earth surface to be constant and in order to minimize the effect of sea surface wind on the sea surface temperature and accomplished a swath width of about 1450 km. A more detailed description of AMSR-E sensor is given by Kawanishi *et al.* (2003).

The AMSR-E footprint size for SST measurements is about 56 km, and the accuracy is estimated to be about 0.4° C. Sidelobe contamination at 6.9 GHz with the AMSR-E antenna extends about 75 km from land and ice, both of which are easily identified as brightness temperatures that are considerably warmer and less polarized than ocean brightness temperatures. AMSR-E retrievals of SST are based on measurements of brightness temperature at 6.9 GHz.

Table 4.1: AMSR-E Main Characteristics

Items		Characteristics					
Observation Frequency		6.925 GHz	10.65 GHz	18.7 GHz	23.8 GHz	36.5Ghz	89.0 GHZ
Spatial Resolution		50 km		25 Km		15 Km	5 km
Band Width		350 MHz	100 MHz	200 MHZ	400 MHz	1000 MHz	3000 MHz
Polarization		Horizontal and Vertical					
Incidence angle		55°					54.5°
Cross polarization		less than -20 dB					
Swath Width		more than 1450 km					
Dyanmic range		2.7-340 K					
Precision		1 K as target					
Sensitivity		0.34K	0.7K	0.7K	0.6K	0.7K	1.2K
Quantifying Bit Number		12 bit	10 bit				
Data Rate		87.392 Kbps					
Electric Power		350 ± 35 W					
Weight		324 ± 15 kg					
Size	Antenna Unit	1.95 x 1.7 x 2.4 m					
	Control Unit	0.8 x 1.0 x 0.6 m					

Rain-contaminated measurements are identified and excluded from further analysis using collocated measurements at 36.5 GHz.

The ocean algorithm is based on the physical Radiative Transfer Model (RTM) described in Wentz & Meissner (2000). The RTM consists of an atmospheric absorption model for water vapour, oxygen and liquid cloud water and a sea surface emissivity model that parametrizes the emissivity as function of sea surface temperature, sea surface salinity, sea surface wind speed and direction. The details of the physical RTM have been described in Wentz & Meissner (2000). Some components of the model have been updated. These are the dielectric constant of sea and cloud water (Meissner & Wentz, 2004), the isotropic wind induced sea surface emissivity (Meissner & Wentz, 2005) and the wind directional signal of the sea surface emissivity (Meissner & Wentz, 2002, 2005). In early 2011, new atmospheric corrections were developed by Meissner and Wentz 2012 based on WindSat and still SSM/I measurements. The retrievals (see Figure 4.1) consist of a set of two-stage regression algorithms. The first-first stage is a set of regressions trained with global data. The first-stage retrievals provide reasonably good estimates of SST, wind, vapour, and cloud. However, because of the non-linear relationships between brightness temperature and the geophysical parameters, the retrievals coming from the global regressions are not optimal. In the second stage, a set of regressions that have been specially trained for a localized range of environmental conditions in the neighbourhood of the first-stage retrievals is used.

In this Ph.D. thesis, Microwave SST fields are obtained from version 7 of the AMSR-E ocean products produced by Remote Sensing Systems (RSS, `www.remss.com`), which have a spatial resolution of $1/4 \times 1/4$ degrees. Additionally, in order to evaluate the quality of the reconstruction a 3-day average sea surface wind speed from version 7 of the AMSR-E ocean products produced by RSS is used. This field is given in the same spatial grid as the SST field

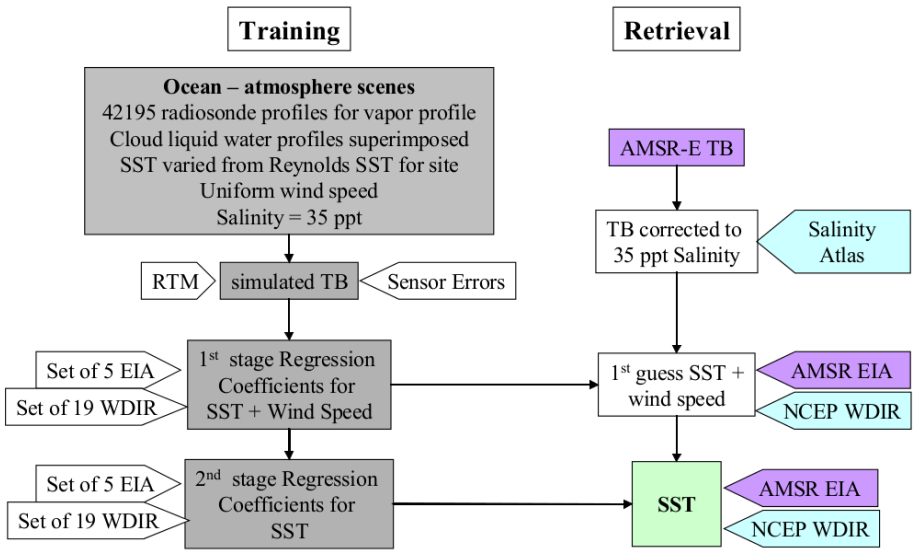

Figure 4.1: Schematic diagram showing the SST algorithm training and retrievals (Credits Wentz & Meissner (2007))

described before. Figure 4.2 shows an example of the 3 days average of SST and Sea wind surface at a global scale provided by RSS.

4.2 AVISO Data

AVISO (*Archiving, Validation and Interpretation of Satellite Oceanographic data*) distributes satellite altimetry data from Topex/Poseidon, Jason-1, ERS-1 and ERS-2, EnviSat missions, and DORIS precise orbit determination and positioning products.

4.2.1 Along-track

The product generation process is composed of four steps: computation of raw Sea Level Anomaly (SLA) η' , cross-validation, filtering and sub-sampling, and generation of by-products. Since the geoid is not well known yet, the sea surface height (h) cannot be used directly, the sea surface height anomalies are used instead. They are computed from the difference of the instantaneous SSH minus a temporal reference $\langle h \rangle$:

$$\eta' = h - \langle h \rangle, \tag{4.1}$$

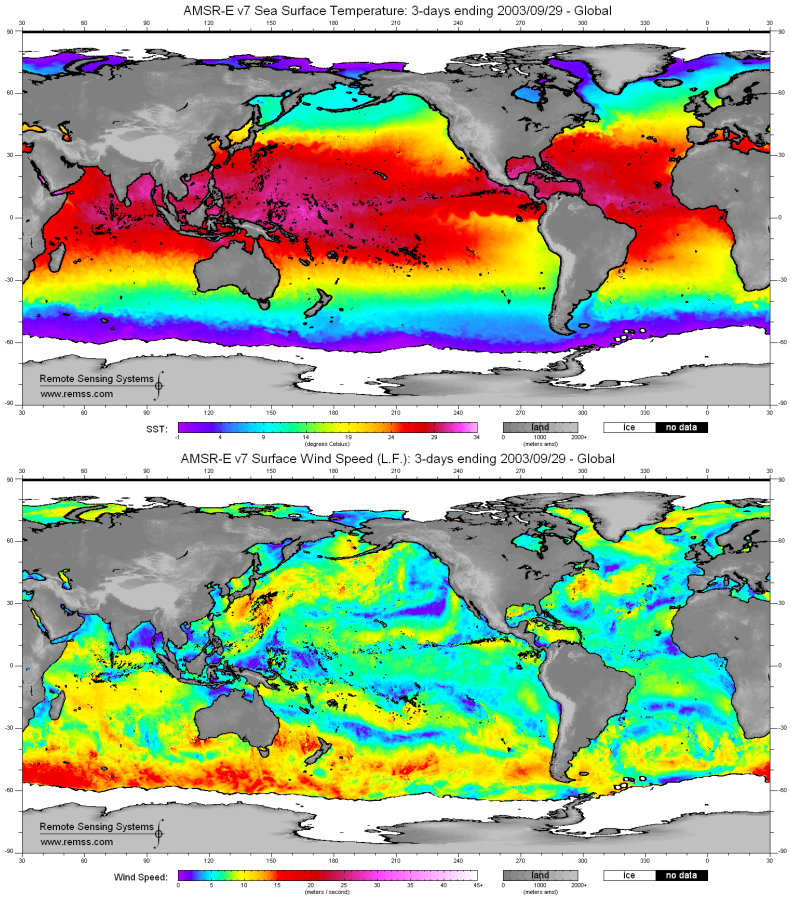

Figure 4.2: Example of SST and Wind 3day products from RSS `www.remss.com`

this temporal reference $\langle h \rangle$ can be a Mean Profile (MP) in the case of repeat track analysis or a gridded Mean Sea Surface (MSS) when the repeat track analysis cannot be used. The repeat track analysis takes profit of the satellite orbit for which the ground track periodically repeats itself at intervals of few days. The computation of the MP is not a simple average from the same ground track on the longer period as possible. For more details consult (Handbook, 2014a). The errors affecting the SLAs, MPs and MSS have different magnitudes and wavelengths. The computation of the SLAs and their errors associated are detailed in (Dibarboure *et al.* , 2012). After the repeat track analysis, the cross-validation technique is used as the ultimate screening process of isolated and slightly erroneous measurements.

Residual noise and small scale signals are then removed by filtering the data using a Lanczos filter. As data are filtered from small scales, a sub-sampling is finally applied. Along-track SLA are then produced. Note that the filtering and sub-sampling is adapted to each region, as a function of the characteristics of the area, and of the assimilation needs. Along-track Absolute Dynamic Topography (ADT), η , products are obtained as follows:

$$\eta = \eta^{'} + \langle \eta \rangle, \tag{4.2}$$

where $\langle \eta \rangle$ is the Mean Dynamic Topography (MDT). The Mean Dynamic Topography is the

part of Mean Sea Surface Height due to permanent currents, so MDT corresponds to the Mean Sea Surface Height minus the Geoid (see Figure 3.7).

4.2.2 Maps

The merging process is two-fold: mapping and generation of by-products. A mapping procedure using optimal interpolation with realistic correlation functions is applied to produce SLA and ADT maps (respectively, MSLA and MADT products) at a given date. The procedure generates one map for each altimeter mission, but also a combined map merging measurements from all available altimeter missions (Ducet *et al.* , 2000). From version 3 onwards, the mapping process takes into account an updated suboptimal Optimal Interpolation parameterization to minimize transition artefacts.

The problem is to determine the value of a field θ, in that case θ is the sea level anomaly relative to a given mean, at a point in time and space, given various measurements of the field unevenly spread over time and space Φ_{obs^i}, $i = 1, ..., n$. The best least squares linear estimator $\theta_{est}(x)$ is given by (Bretherton *et al.* , 1976)

$$\theta_{est}(x) = \sum_{i=1}^{n} \sum_{j=1}^{n} A_{ij}^{-1} C_{xj} \Phi_{obs^i}, \tag{4.3}$$

with $\Phi_{obs^i} = \Phi_i + \epsilon_i$, where Φ_i is the true value and ϵ_i the measurement error. Here, $\mathbf{A}$ is the covariance matrix for the observations themselves, and $\mathbf{C}$ is the covariance vector for the observations, and the field to be estimated.

Combining data from different missions significantly improves the estimation of mesoscale signals (Le Traon & Dibarboure, 1999; Le Traon *et al.* , 2001; Pascual *et al.* , 2006). Several improvements were made compared to the version used by (Le Traon *et al.* , 1998). An improved statistical description of sea level variability, noise and long wavelength errors is used. Covariance functions including propagation velocities that depend on geographical position were thus used. For each grid point, the zonal and meridional spatial scales, the time scale and the zonal and meridional propagation velocities were adjusted from five years of TP+ERS combined maps. In addition to instrumental noise, a noise of 10 of the signal variance was used to take into account the small scale variability which cannot be mapped and should be filtered in the analysis. Long wavelengths errors (LWE) due to residual orbit errors but also tidal or inverse barometer errors and high frequency ocean signals were also derived from an analysis of TP and ERS data. The combined map is used to generate by-products such as geostrophic currents or absolute dynamic topography.

Since April 2011, gridded daily Delayed Time (DT) products are available to the users: all the gridded Delayed-Time products have been computed with a daily temporal resolution. This means that while the processing system is the same as before, the maps were reprocessed for every day. This ambitious reprocessing was motivated by the fact that the weekly resolution used so far for DT maps was insufficient wherever the time decorrelation scale is close to 15 days, especially when end-users want to perform a simple linear time interpolation between

consecutive maps.

In this Ph.D. thesis altimeter SSH fields correspond to daily Delayed-Time Maps of Absolute Dynamic Topography (DT-MADT-upd) produced by Ssalto/Duacs and distributed by AVISO (`www.aviso.oceanobs.com`), which have a spatial resolution of $1/3 \times 1/3$ degrees (Handbook, 2012). This data set is generated with up to 4 satellites avalaible at a given time (see Figure 1.4). Particularly, from October 2002 to May 2005 there were available up to 4 altimeters: T/P, Jason1, Envisat and Geosat Follow-On. This period was selected because product's quality is enhanced thanks to a better sampling (Pascual *et al.* , 2006).

4.3 Mixed layer depth climatology

The mixed-layer is the layer between the ocean surface and a depth where the density is about the same as at the surface. The mixed-layer owes its existence to the mixing initiated by waves and turbulence caused by the wind stress on the sea surface. An effect of mixing is to make both properties of water, temperature and salinity, thus density, more uniform. In this thesis, two different Mixed Layer Depth (MLD) climatologies were used. One provided by IFREMER-LOS and available at `http://www.ifremer.fr/cerweb/deboyer/mld/Surface_Mixed_Layer_Depth.php`. The other one, provided by JAMSTEC and available at `http://www.jamstec.go.jp/ARGO/argo_web/MILAGPV/index_e.html`.

4.3.1 IFREMER-LOS

The Laboratoire d'Océanographie Spatiale (LOS) of the Institut Français de Reserche pour l'Exploitation de le MER (IFREMER-LOS) provides a monthly climatology of MLD with global coverage. The data are given in a regular $2° \times 2°$ grid, and the methodology used to construct the data sets is the one presented by de Boyer Montégut *et al.* (2004) with possible adjustments and evolutions.

The surface MLDs are estimated directly on individual profiles with data at different observed levels. MLD is defined through the threshold method with a finite difference criterion from a near-surface reference value. A linear interpolation between levels is then used to estimate the exact depth at which the difference criterion is reached. The reference depth is set to 10 m to avoid a large part of the strong diurnal cycle in the top few meters of the ocean. The temperature criterion chosen is 0.2°C absolute difference from surface. The fixed criterion in density is 0.03 kg/m^3 difference from surface (see de Boyer Montégut *et al.* (2004) for further details about the choice of the criterion).

4.3.2 JAMSTEC

Japan Agency for Marine-Earth Science and Technology (JAMSTEC) produces a global data set of gridded mixed layer depth (MLD) using Argo temperature and salinity profiles, named *MILA GPV (Mixed Layer data set of Argo, Grid Point Value)*. Since quality of the profile data which

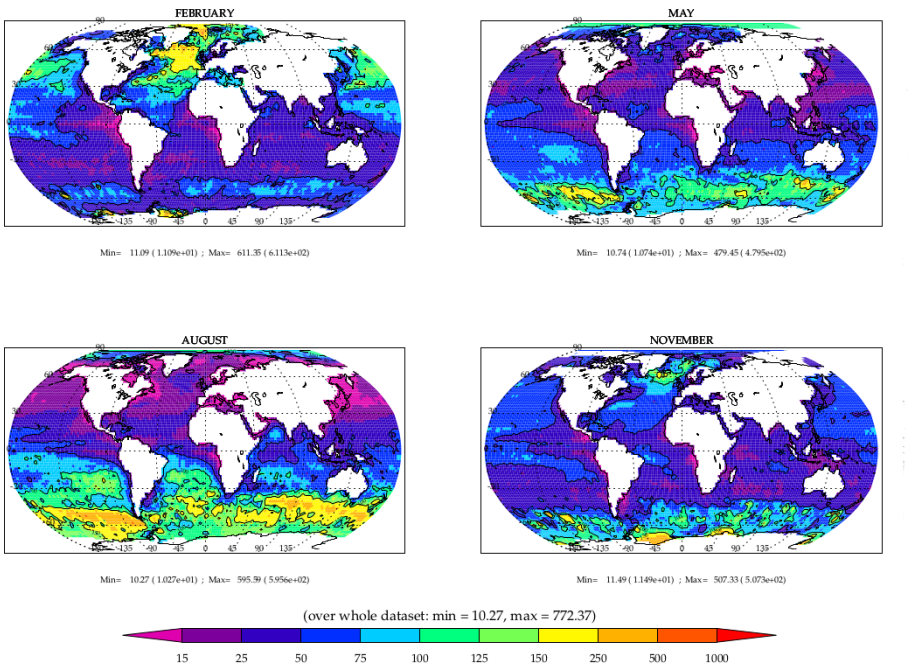

Figure 4.3: MLD climatology. Annual climatology of the MLD provided by IFREMER-LOS `http://www.ifremer.fr/cerweb/deboyer/figures/mld_DT02_c1m_reg2.0.pdf`.

covered fully in the ice-free global ocean is high and uniform and vertical resolution of the profiles is fine (at least 5 dbar in the surface layer), error of MLD is expected to be smaller. Although the coverage of Argo float array was not so good in the earlier stage of Argo project, observing floats almost covered in the World Ocean after 2004. The Argo quality controlled profile data is obtained from Argo Global Data Archive Center (GDAC). To make MLD data set, the finite difference method is used based on sea surface temperature and sea surface potential density. Among the values in the difference of temperature and potential density, mixed layer is chosen with the minimum value between the two values. Two pairs of the temperature and potential density criteria are applied, which are generally used in a lot of researches. The grid point value of MLD is calculated using a median after estimated MLD for individual profiles. Users can use the two data set for their research goals.

4.4 Acoustic Doppler Data Profiler

Acoustic Doppler Current Profilers (ADCPs) are a common component within shipboard instrumental packages onboard many scientific (UNOLS, NOAA) and Navy fleets. During the late 1980s, the data quality was limited by lack of continuous Global Positioning System (GPS) coverage and uncertainties in the ship‘s heading information. By the mid 1990s, the quality improved significantly due to the 24-hour GPS coverage, differential GPS techniques, and the advent of GPS heading sensors. With reliable heading and navigation data, absolute currents in the upper ocean are determined. The data provide fine resolution in time (∼5 minutes), depth (∼10m), and horizontal distance (∼2 km) throughout the duration of a cruise.

The growing database allows a fresh view of upper ocean velocity structure on a variety of temporal and spatial scales. The National Oceanographic Data Center (NODC) ensures the long term preservation and facilitates access to these important data.

The NODC established the Joint Archive for Shipboard ADCP (JASADCP) at the University of Hawaii for the acquisition, review, documentation, archival, and distribution of shipboard ADCP data sets. Figure 4.4 shows the track of the cruises available within the period under study October 2002 - May 2005.

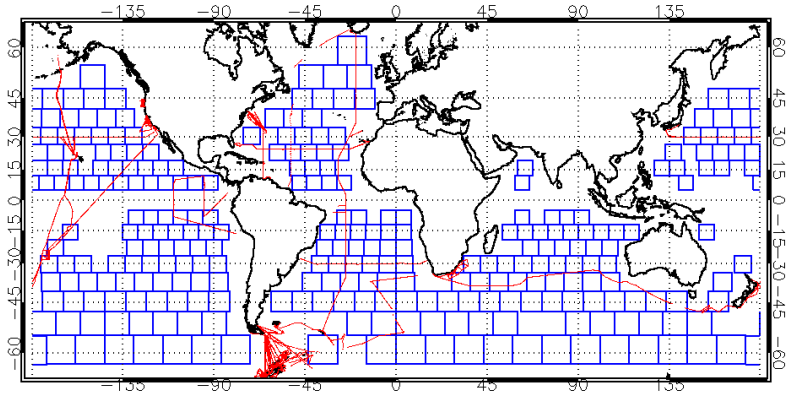

Figure 4.4: Map of available ADCP data within the period under study (October 2002 - May 2005)

4.5 Procedures

In order to assess the capability of microwave SST observations to retrieve ocean surface currents, 952 daily global maps spanning from October 1, 2002 to May 18, 2005 were analyzed. As mention previously, this period was selected because there were four altimeters available, which improves the location of ocean currents (Pascual *et al.* , 2006).

Since AMSR-E SST observations and altimetric maps have diferent spatial resolutions, daily SSH altimetric maps were interpolated onto the AMSR-E SST grid. Daily global SST and altimetric maps were divided into 273 boxes of approximately 800 × 800 km (see Figure 4.4). Boxes with land pixels and latitudes higher than 65° to avoid the ice influence on the SSH measurements were discarded. Moreover, since the geostrophic approximation is not verified near the equator, currents have not been estimated in the equatorial band between 5°S and 5°N. SSH and SST were then projected onto a flat surface using a local Mercator projection and, then re-interpolated onto a double-periodic Fourier grid using mirror symmetry. In order to remove the mean large-scale background flow, SST field was detrended by substracting a fitted plane surface to daily observations.

The flow was reconstructed from the resulting daily SST and SSH maps using two different approaches: (i) by eSQG approach equation (2.56), and (ii) by building a transfer function with SST and SSH observations equations (2.67) and (2.68). The flow reconstructed from altimetric observations using equation (2.60) was also retrieved and used as a reference in order to evaluate the performance of the reconstruction by the two different approaches. All the reconstructed flow were band-pass filtered using a Lanczos fiter in the wavelength range [λ_{min}-400 km]. The mininum cutoff wavelength (λ_{min}) depended on the latitude, taking account of variation in the assumed typical scales of the ocean signal: 300 km equatorward of 10°N-S, 200 km between 10° and 30°N-S, 100 km between 30° and 50°N-S, and 70 km above 50°N-S. This band corresponds to the one applied to along-track altimeter data in the mapping process (Le Traon *et al.* , 1998). The 400 km upper limit is selected to focus on the mesoscale part of the ocean turbulance.

Two different metrics were used in order to quantify the quality of the flow reconstruction: correlation coefficients and the root mean square error (RMSE from now on). In general, unless otherwise specified, the evaluation of the performance of the flow is centered on comparing the stream function. Thus, the correlation between the stream functions retrieved from eSQG and altimetric observations, respectivelly, will be referred as eSQG correlation for easy reading. Similarly, the correlation between the stream functions retrieved from a transfer function estimated with simultaneous SST and SSH observations and altimetric observations, respectivelly, will be referred as combined correlation. A statistical t-test was applied to the obtained correlations with a 5% significance level. Only significant correlations were taken into account when averaging.

Chapter 5

Capability of microwave SST to reconstruct currents

5.1 Introduction

In this chapter, the capability of Sea Surface Temperature (SST) observations to reconstruct surface currents at a global scale is investigated.The methodology consists of estimating the stream function by taking the phase from SST, and the amplitude spectrum from the SSH and then comparing it with the stream function derived from altimetric measurements.

Recent studies have unveiled that the relationship between SST and SSH may differ from k^{-1} as the SQG theory predicts (Isern-Fontanet *et al.* , 2014). To overcome this potential limitation we have proposed exploiting the synergy between current SSH and SST measurements by combining the phase of SST, i.e. the relative position of structure, with the amplitude of SSH measurements, i.e. the distribution of energy among scales. However, before attempting to combine SST images with along-track SSH measurements it is necessary to first identify the conditions and geographical areas where SST can be used to retrieve ocean currents. Indeed, the main limitation on the use of SST to derive currents using the above approach is that both two-dimensional SSH and SST have to be in phase. Recent studies based on numerical simulations have revealed that the phase shift between SST and SSH is minimum for deep Mixed Layers (ML) (Isern-Fontanet *et al.* , 2008, 2014). Nevertheless, a global study on the matter has yet to be undertaken.

The main objective of this chapter is to assess the capability of SST to derive ocean currents at a global scale. The novel ingredients with respect to (Isern-Fontanet *et al.* , 2006) and (Isern-Fontanet *et al.* , 2014) is the global extension of the study and the combination of SST and SSH to explore potential improvement of SQG flow reconstruction.

5.2 Methodology

As it was seen in section 2.5, the total solution to the PV inversion problem at the ocean surface can be written using the formalism of a transfer function (TF) as:

$$\hat{\psi}(\vec{k}) = F_T(k)\hat{T}_s(\vec{k}), \tag{5.1}$$

where the TF $F_T(k)$ only depends on the modulus of wavenumber k. When Surface Quasi-Geostrophic (SQG) approximation (Held *et al.* , 1995; Lapeyre & Klein, 2006a) is valid, this TF can be written as:

$$F_{sqg}(k) = -\frac{g\alpha'}{n_e\rho_0 f_0}k^{-1}, \tag{5.2}$$

where ρ_0 is a reference density, α' is an effective thermal expansion coefficient and n_e an effective Prandtl ratio.

In addition, the other approach proposed (Isern-Fontanet *et al.* , 2014), referred in this Ph.D. thesis as combined approach, takes into account the synergy between microwave and altimeter observations and combines the phase of SST measurements and the amplitude of SSH measurements. This points to build the transfer function between SST and the stream function as:

$$F_T(k) = \frac{g}{f_0}\frac{|\hat{\eta}(\vec{k})|}{|\hat{T}_s(\vec{k})|}. \tag{5.3}$$

By construction, the stream function retrieved from this transfer function only differs from the stream function retrieved from altimetric observations (equation 2.60) by the relative position of flow patterns. This allows to investigate into which areas and under which conditions the structures observed in SST and SSH maps are coherent. In addition, it is possible to assess the capability of using SST observations to reconstruct the flow.

The reconstruction of the flow by eSQG and combined approaches were performed at a global scale from daily SST and SSH observations (see section 4.5 for further details) and compared to the one retrieved from altimetric observations by means of correlation. A statistical Student t-test was applied to the obtained daily spatial correlations with a 5% significance level. Only significant correlations were taken into account when averaging.

5.3 Sample boxes

A first analysis was applied to two boxes, one located in the Gulf Stream (GS) area and the other one in the Antarctic Circumpolar Current (ACC). The box located in the GS is largely similar to that used the same box as in (Isern-Fontanet *et al.* , 2006), although smaller in our study. Figure 5.1 shows the comparison between the velocity fields reconstructed from SST using eSQG and the combined method (equations 5.2 and 5.3) and the velocity fields reconstructed from SSH. These two examples correspond to the days for which the highest combined approach correlations were found. In particular, the GS box corresponds to February 1, 2003 and had a correlation of 0.944. The ACC box corresponds to October 3, 2002 and had a correlation of

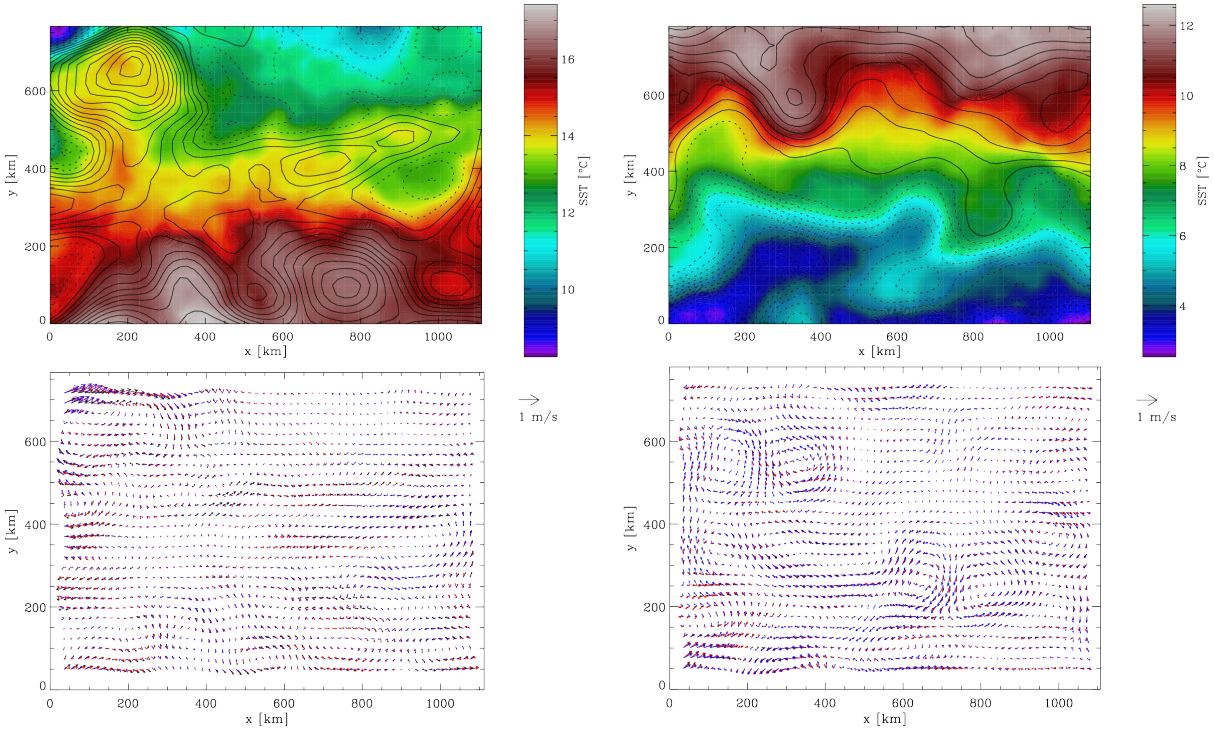

Figure 5.1: Velocity reconstruction of the sample boxes. Top: SST image with Absolute Dynamic Height contours superimposed (in black) Bottom: Reconstructed velocity field: from altimetry (black), SQG (blue) and Combined approach (red). Left: Gulf Stream Current box, latitude between 41.16° and 48.03° and longitude between −41.00° and −31.00° (February 1, 2003). Right: ACC box, with latitude ranging between −48, 12° and −41.12° and longitude between −30.63° and −20.67° (October 3, 2002).

0.982. Notice that the agreement is better between altimetry and the combined approach, than it is between altimetry and the eSQG solution.

The analysis of the temporal evolution of correlations reveals that the correlations obtained for the combined approach are higher than those obtained for the eSQG reconstruction (see figure 5.2). Only few exceptions can be found when correlations are low. Besides, the temporal evolution of correlations for the GS box shows a clear seasonal signal. This is confirmed by the estimation of the Lomb periodogram (Press *et al.* , 2007), which shows a large peak at 256 days (Figure 5.3). For the box in the ACC the seasonal cycle was less evident, although it was still present as indicated by the peak in the Lomb periodogram at 319 days. Here we used the Lomb periodogram rather than the more classical Fourier transform due to the presence of gaps in the time series of correlations. It is interesting to note that this seasonal variability is qualitatively similar to the variability of the MLD.

5.4 Global comparison to eSQG

Results shown in the previous section suggest that correlations tend to be higher for the combined approach than for the eSQG. This result is confirmed when the correlations for all boxes are compared (figure 5.5). We further computed the direct correlation between SST and SSH for the

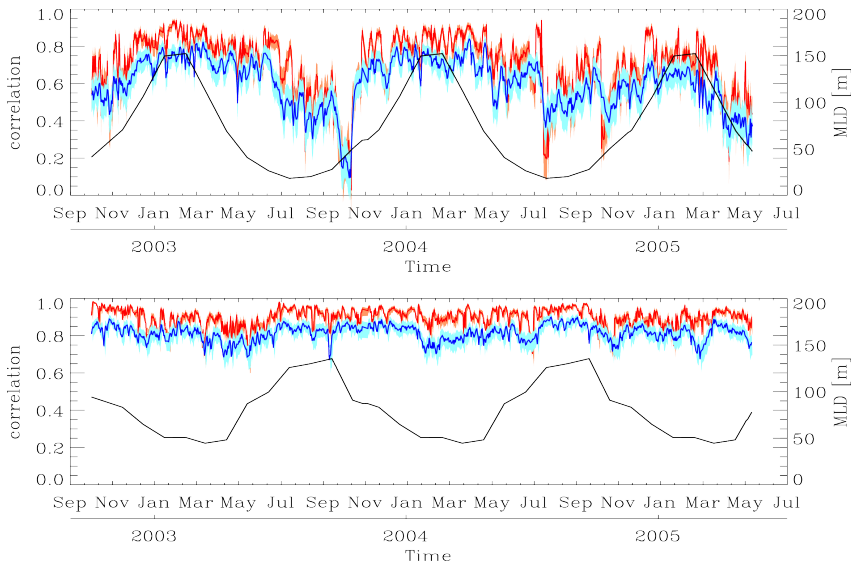

Figure 5.2: Temporal evolution of correlations. Temporal evolution of correlations (solid line) and the 95% confidence interval with t-distribution (shadow) for the combined approach (red) and correlations for the SQG reconstruction (blue) (October 2002 to May 2005). Black line corresponds to the temporal evolution of the mean mixed layer Depth (MLD) (right vertical axis). Top: Gulf Stream Current box, latitude between 40.97° and 48.17° and longitude between −57.43° and −41.14°. Bottom: ACC box, latitude ranging between $-48,17°$ and −40.97° and longitude between −30.63° and −20.67°.

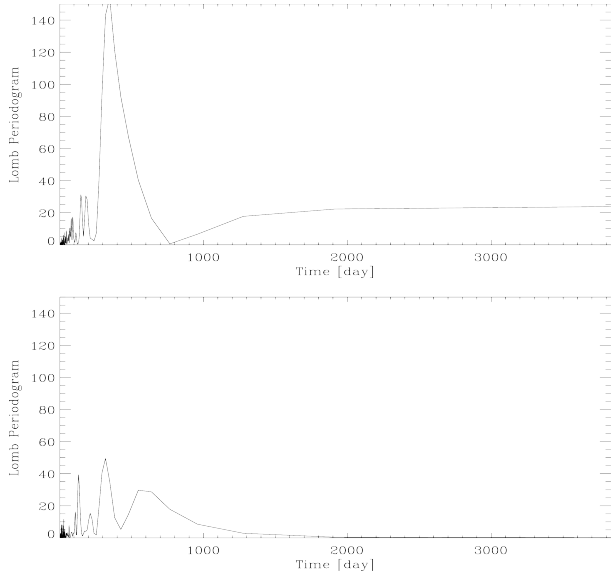

Figure 5.3: Lomb periodogram of correlations. Lomb periodogram of temporal evolution of correlations for the combined stream function(October 2002 to May 2005) shown in Figure 5.2. Top: Gulf Stream Current box, latitude between 40.97° and 48.17° and longitude between −41.14° and −30.86°. Bottom: ACC box, with latitude ranging between $-48,17°$ and −40.97° and longitude between −30.63° and −20.67°.

band between λ_{min} and 400 km, where λ_{min} depends on latitude as it was presented in section 4.5, to assess to which extent SST and SSH isolines are parallel. The correlations between eSQG stream function and altimetric stream function are significantly higher than direct correlations

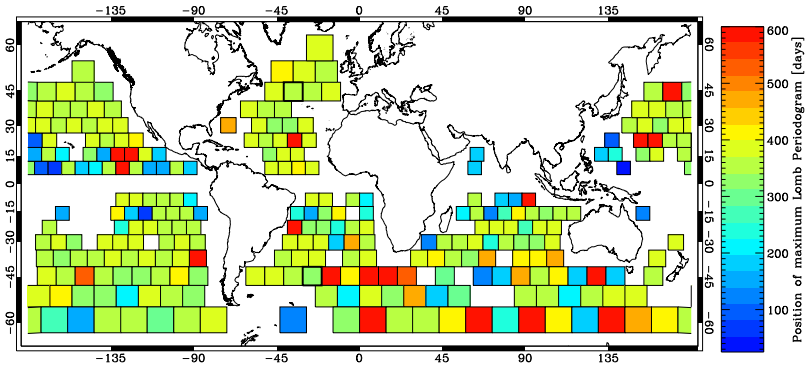

Figure 5.4: Position of the maximum peak of Lomb periodogram of temporal evolution of correlations for the combined stream function.

between SST and SSH in 12.5% of cases, which makes evident that SST anomaly is not a proxy of the stream function. It is also worth highlighting that, in the case of eSQG method no correlations higher than 0.9 were obtained, while in the case of the combined approach, some correlations do exceed this value. Indeed, correlations between the combined stream function and the altimetry stream function are significantly higher than correlations between eSQG stream function in 62.6% of the cases.

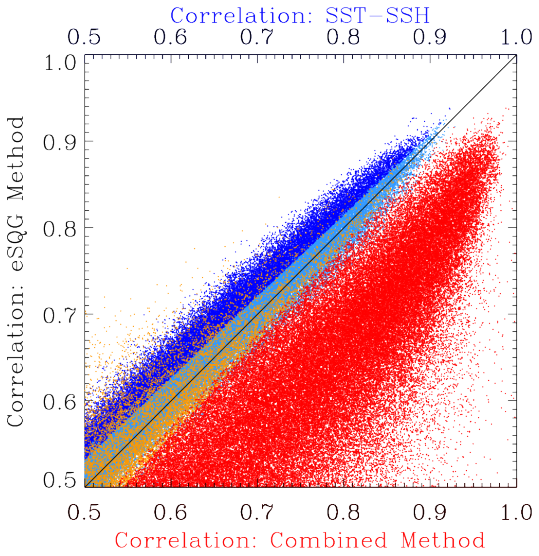

Figure 5.5: Performance of the flow reconstruction: combined approach vs eSQG Scatter plot of eSQG correlations vs. combined correlations (red points indicate that the combined correlation between is significantly higher than the SQG correlation respect to significance level 0.05, orange indicate that correlations are not significantly higher or lower). Scatter plot of eSQG correltion vs. the correlation of SSH and SST measurements (band pass filtered 100-400 km) (blue points indicate that eSQG correlation is significantly higher than correlation of SSH and SST measurements respect to significance level 0.05, light blue points indicates that correlations are not significantly higher or lower.

5.5 Spatio-temporal analysis

Monthly mean correlations for the combined stream function were computed for all boxes with the objective of identifing the areas best suited for the reconstruction of ocean dynamics using SST. Results shown Figure 5.6 clearly reveals that the reconstruction is better in regions near the major extratropical current systems such as the Gulf Stream, the Kuroshio, and the Antarctic Circumpolar Current (ACC), where intense mesoscale activity can be observed. On the other hand, lower correlations (ranging between 0.2 and 0.4) are obtained at low latitudes ($15°N - S$). Although, in some cases, they can increase up to 0.6 in winter months, January to March in the northern hemisphere, and June to August in the Southern hemisphere. However, some differences are found depending on the area. For instance, in the Northern hemisphere, the Kuroshio region presents consistently lower correlations than does the Gulf Stream region, even in boreal winter season when the combined reconstruction is enhanced. This example can be juxtaposed with an area in the southern hemisphere, in the ACC region, where the combined stream function retrieval seems perform reasonably well throughout the entire year with slightly higher correlation in austral winter months.This seasonal variability is confirmed by the estimation of the Lomb periodogram. Most of the boxes presented the maximum peak of the Lomb Periodogram in the range of 300 to 400 days (Figure 5.4), with a few exceptions in which the peak is present within this period but it is not the maximum peak.

The average correlation for winter months, from January to March in the northern hemisphere and from June to August in the Southern hemisphere, was computed for the stream function, both components of the velocity field and vorticity ($\zeta = \nabla^2\psi$). Only significant correlations were taking into account when averaging. In most of the boxes the number of correlations averaged range between 130 and 271, with the exception of 7 boxes in which less than 100 correlations were averaged (white contour in figure 5.7). We focused on the winter season since it is the period of the year for which reconstruction is best , as shown in figure 5.6. Results show that all parameters present similar geographical patterns (figure 5.7). Furthermore, they also show that higher correlations correspond to the stream function, while the lowest correspond to the vorticity. Indeed, the capability of reconstructing vorticity is moderate. The highest mean correlation for vorticity is 0.79 and corresponds to the box selected in section 5.3 located in the ACC. For the box located in the GS region, this correlation is 0.67. For most of the boxes located in the southern hemisphere (111 of the 176 boxes), higher mean correlations are obtained for the zonal component of the velocity, when compared with the meridional component; whereas in the southern hemisphere, half of the boxes have higher mean correlations for the zonal component of velocity (49 of the 97 boxes).

In order to evaluate if the combined method reproduces the temporal variability of the currents retrieved by the altimeters, we computed the Eddie Kinetic Energy (EKE), defined as

$$E_{EKE} = \frac{1}{2}[\sigma_u^2 + \sigma_v^2], \tag{5.4}$$

where σ_u^2 and σ_v^2 are the temporal variance of the the zonal and meridional components of the velocity field, respectively. We then computed the spatial correlation between the EKE

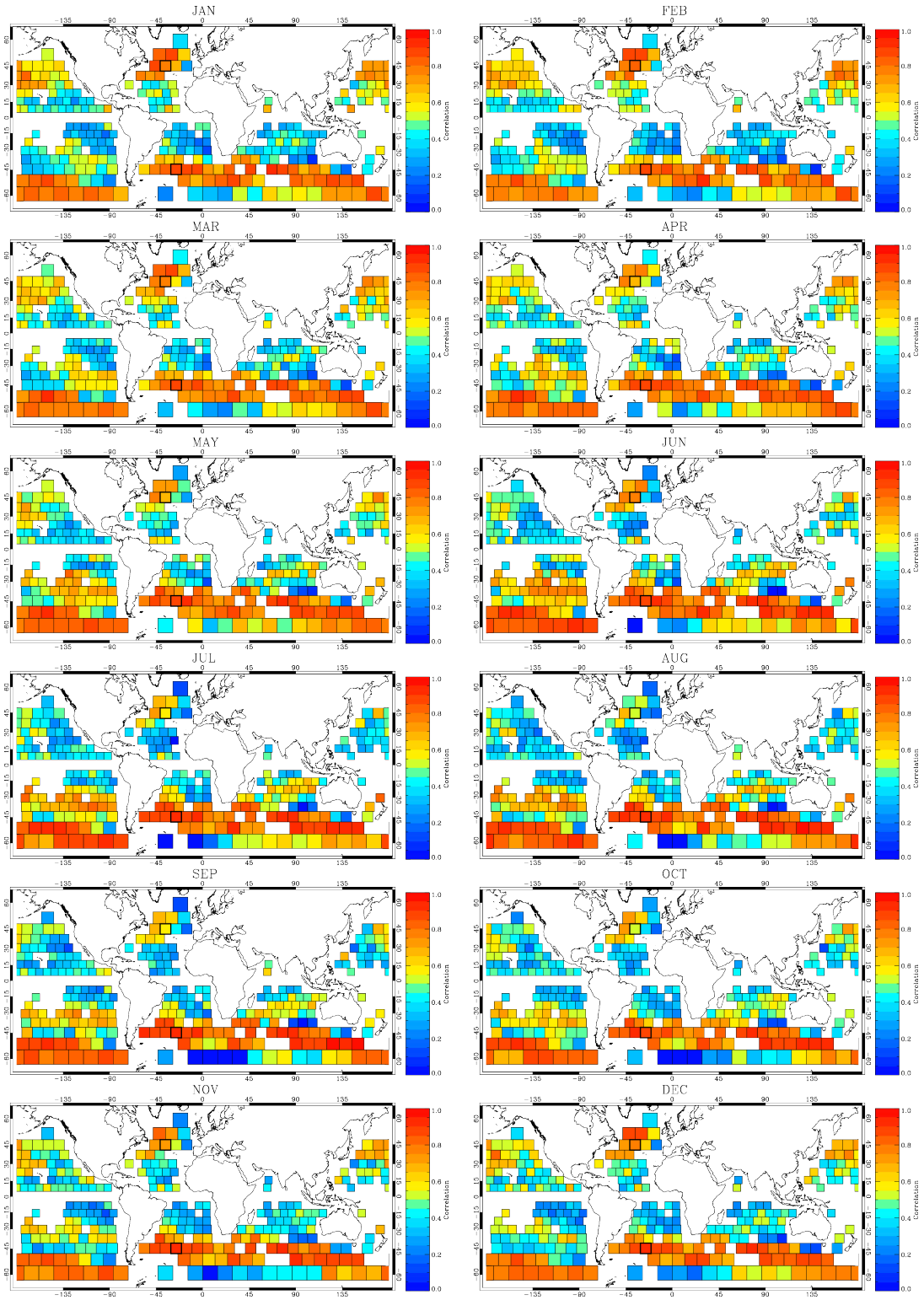

Figure 5.6: Global monthly mean correlation between stream functions retrieved by SSH measurements and Combined method. Wide line delimits selected boxes in Figure 5.2.

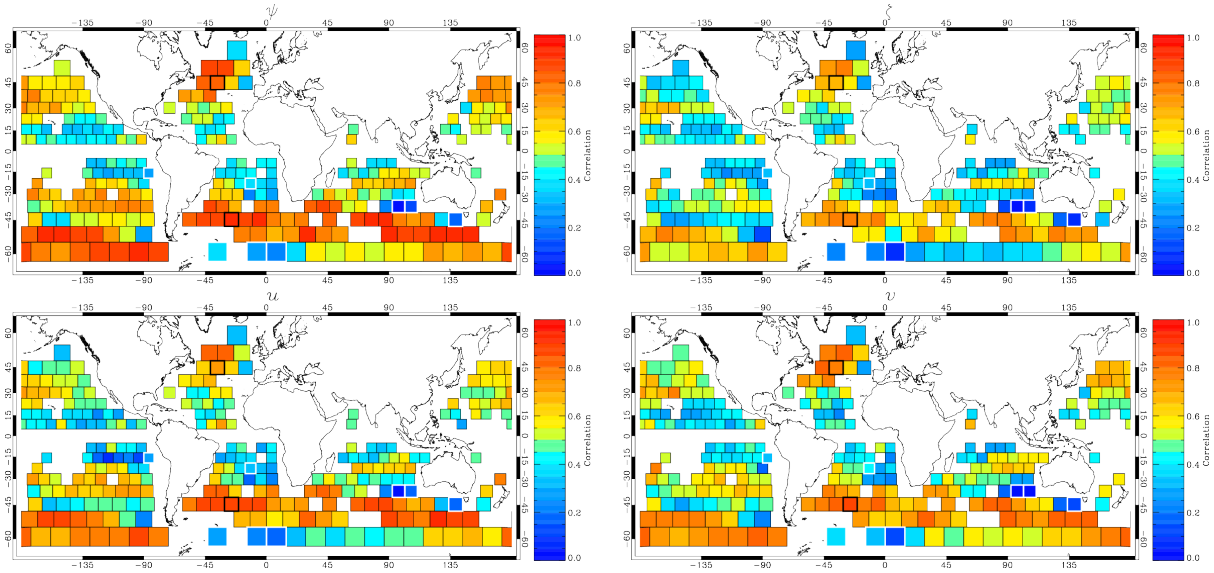

Figure 5.7: Winter mean correlations between the combined method and altimetry. From left to right and from top to bottom: stream function (ψ), vorticity (ζ), zonal velocity (u) and meridional velocity (v). For Northern hemisphere January, February and March were considered. For Southern hemisphere: June, July and August. Wide black line delimits selected boxes in Figure 5.2. Wide white line delimits boxes that have less than 100 significant correlations.

for the flow reconstructed from SST (equation 5.3) and the EKE for the flow reconstructed from SSH (Figure 5.8). Results show that in high energetic regions, the correlations between combined EKE and altimetry EKE exceed 0.95 (Figure 5.8). Moreover, it can be observed that EKE correlations have similar geographical patterns to the correlations shown in Figures 5.6 and 5.7. In general, high EKE correlations boxes also have high stream function correlations and correspond to high energetic regions. This is not the case, however, for three of the boxes located in Kuroshio region, which have high EKE (0.10 m^2/s^2), and high combined winter correlations (between 0.71 and 0.75) but low EKE correlations (between 0.2 and 0.34). Nevertheless, for most of the boxes, the combined method reproduces the temporal variability of the currents retrieved from altimetric measurements quite well, even in the tropics, where correlations higher than 0.5 are obtained for most of the boxes.

To get insight on the link between EKE and the performance of the reconstruction from SST observations, we compared mean correlations for the combined stream function with the EKE (figure 5.9). Here again, results reveal that the combined method reproduces the temporal variability of the currents retrieved from altimetric measurements very well, even for those boxes that performance poorly (e.g. boxes with correlations lower than 0.5 (figure 5.7) have EKE correlations higher than 0.6 (figure 5.8)).

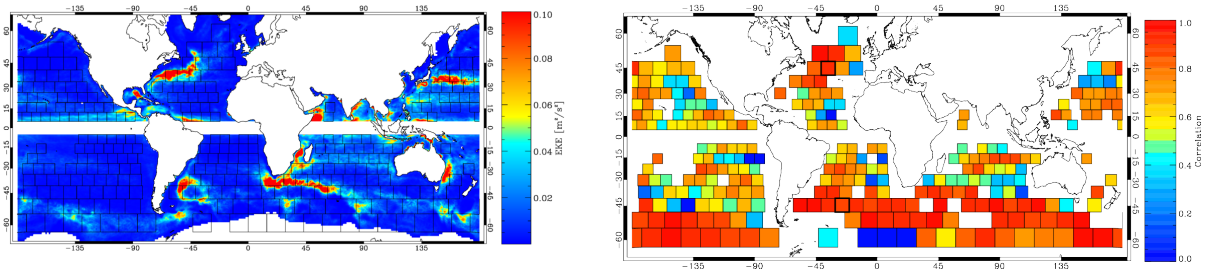

Figure 5.8: Eddy Kinetic Energy. From right to left: Eddy Kinetic Energy from October 2002 to May 2005. Correlations between Eddy Kinetic Energy of reconstructed velocities from altimetry measurements and from Combined method spanning from October 2002 to May 2005. Wide line delimits selected boxes in Figure 5.2.

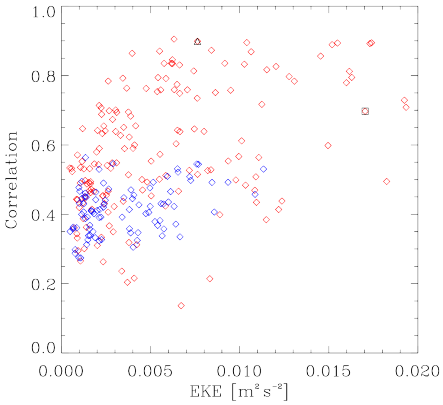

Figure 5.9: Scatter plot of the mean correlation for the combined stream function and the Eddy Kinetic Energy. Blue points correspond to boxes located in low latitudes (between ±20°), red points correspond for boxes located at higher latitudes. Black is used to represent the two selected boxes in the local study: triangle (△) for ACC box, and square (□) for the GS box.

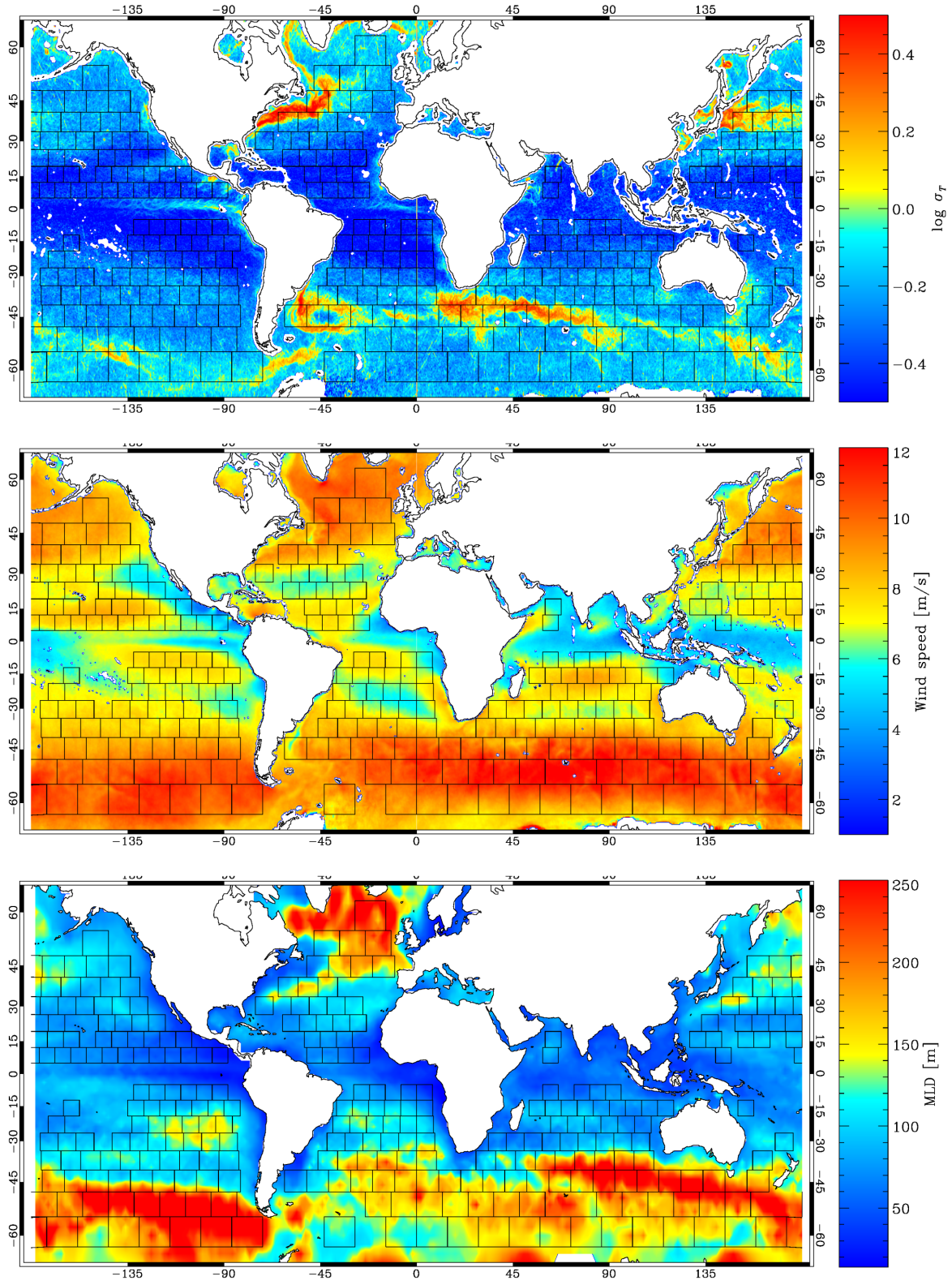

Figure 5.10: Enviromental conditions. From top to bottom: standard deviation of the thermal gradient, mean wind and RMS of the MLD. All fields were estimated for the period under study with the exception of the MLD, which was estimated from a climatology.

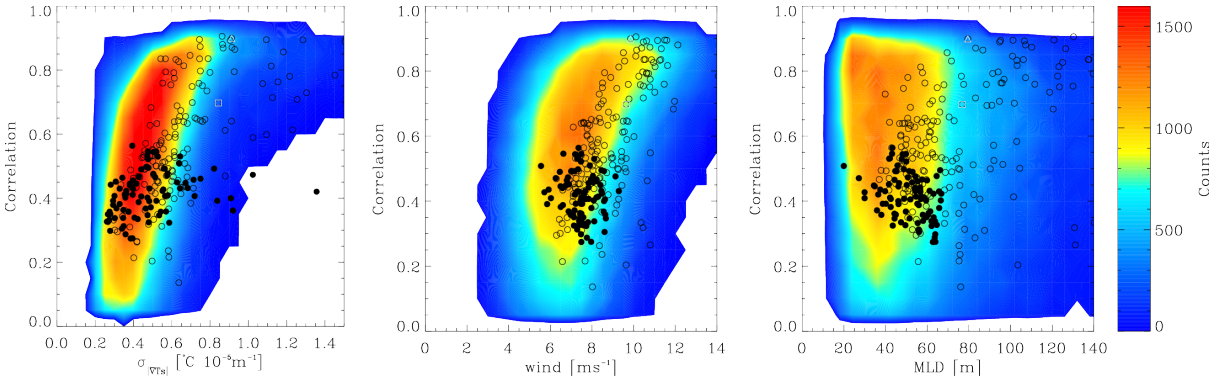

Figure 5.11: Impact of enviromental conditions in the flow reconstruction. From left to right: two dimensional histogram of the combined stream function correlations and: standard deviation of the thermal gradient, the RMS of the wind and the mixed layer depth, respectively. Circles correspond to the mean correlations for each box. Filled circles correspond to boxes located in low latitudes (between $\pm 20°$), circles correspond to boxes located at higher latitudes. White is used to represent the two selected boxes in the local study: triangle ($\triangle$) for ACC box, and square ($\square$) for the GS box.

5.6 Dependence on environmental conditions

In addition to characterizing the areas in which SST is better suited to reconstructing the flow, it is also necessary to identify under which environmental and dynamical conditions this is possible. Based on previous results (Isern-Fontanet *et al.* , 2006, 2008), we have defined a set of parameters to characterize such conditions: the standard deviation of the thermal gradient, the RMS of the MLD and mean wind (Figure 5.10). All fields were estimated for the period under study (May 2002 to October 2005). Comparing Figure 5.10 with the temporal global mean correlation (Figure 5.6), it can be observed that the reconstruction is better in high thermal gradient regions. The RMS of the MLD also presents similar geographical patterns to the mean correlation map shown in Figure 5.7, with higher correlations found in areas with deeper mixed layer. In fact, Isern-Fontanet *et al.* (2008) showed that the success of eSQG reconstruction depends on the quality of the SST as a proxy of the density anomaly at the base of the mixed layer, which occurs after a mixed layer deepening period.

In order to find out which of these environmental conditions have a greater impact on the reconstruction, the two dimensional histogram of the stream function correlations for each box and all temporal sets versus the thermal gradient, the RMS of the MLD and mean wind is shown, respectively, in Figure 5.11. The scatter plot of the mean correlation for each box has been overplotted on the 2D histogram. For geographical identification purposes, the mean correlations for boxes located in low latitudes are differently marked from those in high latitudes. Results clearly indicate that the performance in low latitudes is poorer, where thermal gradients, wind and depth of mixed layer are low. As it can be seen in Figure 5.11, each of the studied parameters appears to play an important role in the reconstruction. The greater the thermal gradients, the higher the obtained correlations. The same is observed in the case of wind speed and MLD, although regarding MLD, this dependence is less evident. It may be recalled here

that SST and wind are daily observations, whereas the MLD is a climatology that is interpolated in the studied period.

5.7 Discussion

In section 5.4, we showed that using the information from the spectrum of SSH significantly improves the flow reconstruction in comparison to the application of the eSQG approach. This is not a surprising result, considering we use more information to reconstruct the flow. The result also additionally suggests that the transfer function between SST and SSH does not necessarily follow the eSQG predictions. Previous theoretical (Lapeyre & Klein, 2006a; Lapeyre, 2009; Klein & Hua, 1990) and numerical studies (Isern-Fontanet *et al.* , 2014) have already unveiled deviations from the eSQG predictions, particularly for large scales. In this study we focused on the assessment of the capability of SST to retrieve ocean currents and have therefore not analysed the characteristics of the transfer function, which has been left for a future study (Chapter 6). Nevertheless, our results confirm the potential for a new approach to derive ocean currents based on exploiting the synergy between SST and SSH measurements proposed by Isern-Fontanet *et al.* (2014). As things currently stand, satellite-derived SST images can provide information about the location of surface currents but information about the intensity of such currents is difficult to obtain. On the other hand, while along-track SSH measurements can provide information on the intensity of surface currents, its sampling geometry hampers the reconstruction of two-dimensional patterns when an insufficient number of altimeters is used (Pascual *et al.* , 2006). Thus, an ideal approach would be one which could combine the phase from microwave SST with the amplitude spectrum from along-track SSH, thereby allowing for the retrieval of the ocean currents even when only limited number of altimeters is available.

It is also worthy mentioning that, the underlying assumption in the eSQG and our approach is that temperature and density anomalies are negatively correlated, i.e. warm waters have associated lower density anomalies. However, this may not be the case if salinity is the dominant contribution to the density anomaly. In such situations it is possible to find the opposite situation, which would carry negative correlations between the reconstructed stream function and SSH. We have observed that only 0.12% of the correlations range between -1 and -0.8 and were significant at 0.05 confidence level. Besides, if cold-core and warm-core anticyclonic eddies are both present in the same area, observed 327 correlations may be low. This could explain the lower mean correlation obtained in the Kuroshio area (Figure 5), when comparing to other extratropical current systems regions (Hosoda & Hanawa, 2004).

In this study we impose the spectrum of the reference field, i.e. SSH, on SST. This implies that, we are actually comparing the phase of SST measurements with the phase of altimetric maps. Consequently, the combined method will perform better when the phase of SST properly reflects the oceanic structures detected by altimeters. A recent study conducted by Hausmann & Czaja (2012), focusing on the SST/SSH relationship following eddy tracks, found that the eddy SST signature is characterized by a westward phase shift of SST anomaly with respect to rotating eddy cores. This phase shift is more pronounced for eddies originating in quiescent

regions of the subtropical gyres, but is also clearly established for more energetic regions, such as the GS and ACC regions. These outcomes are consistent with our results, and it may explain the geographical patterns of the obtained correlations between the combined method and altimetry stream functions (Figures 5.6 and 5.7), with higher correlations in regions near the major extratropical current systems. In fact, it is interesting to note that even in the case of the box that performed better, the ACC box, the highest correlation did not reach 1 (see Figure 5.2). Furthermore, the dynamics in the Mixed Layer can also introduce a phase shift between the SST and the SSH as pointed out by previous studies (Isern-Fontanet *et al.* , 2008, 2014). Taking these studies into account, we have also investigated the role of the ML. Results confirmed that the deeper the ML, the higher the obtained correlations. In this study we have used a climatology of MLD. However, time-dependent MLD data owing to the ARGO float observations (Hosoda *et al.* , 2010) could potentially be used as an indicator of where and when the proposed methodology could be applied operationally.

The analysis of the temporal evolution of correlations showed a clear seasonal variability that is qualitatively similar to the variability of the ML, with higher correlations in winter when ML is deeper. This outcome was confirmed by a recent work (Reul *et al.* , 2014) centered in the Gulf Stream region that investigated the ability of the ESA SMOS microwave salinity sensor to complement altimetry, thermal and ocean color imagery to characterize dynamics and variability of GS fronts and rings. Furthermore, they found higher correlations between Sea Surface Salinity (SSS) and SSH, than between SST and SSH during the summer period. This result suggests that SSS satellite observations could complement satellite SST and SSH observations for providing a better characterization of ocean surface dynamics.

The proposed methodology has several advantages. The stream function is obtained by combining a single image of SST and SSH, and it has the same resolution as the original field. Microwave SST measurements have low resolution when compared to IR SST measurements, but the main advantage of using microwave sensors is their capability to measure SST through clouds (Hosoda, 2010). This property is a distinct advantage over infrared measurements of SST, which are obstructed by clouds, and makes microwave sensors specially suited for global studies. The excellent time coverage is another principal strength of using microwave measurements, and ocean remote sensing data in general, when compared with most traditional ocean current observation methods (current meters, ADCP, drifting buoys). It is important to stress that both remote sensing and in-situ observations are complementary methods. Furthermore, additional work should be carried out in order to validate reconstructed currents by the proposed combined method with in-situ data and along-track altimeter data. It is worth mentioning that, despite this work is being centered on the period when four altimeters were available and thus the location of ocean current in the ADT altimetric maps is enhanced, the altimetric maps may contain structures that are not present in SST images, due to the interpolation, noise or other corrections applied in the process of generating these maps. This reinforces the need for a validation using in situ data (see Appendix A for a comparison of the reconstructed velocity fields with ADCP velocity data).

In a recent study, Tandeo *et al.* (2014) also attempted to reconstruct ocean dynamics using

satellite SST and SSH observations. More specifically, they developed a class regression model to decompose a local transfer function between SST, SSH and surface current into different dynamical modes. Then, they applied this methodology to the Agulhas region during 2004, and also comparing the latent reconstruction of ocean surface velocity to velocities retrieved from MADT altimetry measurements. They found a good agreement with a correlation coefficient of 0.72 for surface currents. When we compare these results with our approach we find similar linear correlations. Indeed, if we consider the three boxes that cover the area studied in Tandeo *et al.* (2014) and same period 2004, we find mean correlations of the stream function ranging between 0.75 and 0.8. In the case of the zonal component we obtained correlations ranging between 0.71 and 0.76, and between 0.61 to 0.7 for the meridional component. Our approach has an advantage when compared to the method they propose: it is intuitive and simple to implement, in principle. Recently, Wang *et al.* (2013) proposed a method that exploits the knowledge of the SST and SSH to reconstruct the 3D velocity field, i.e. it assumes that the 2D SSH field is known. On the contrary, in our approach we only assume that the SSH spectrum is known, which is then combined with an SST images to reconstruct the surface stream function and, consequently, the SSH. Therefore, although both methods combine information from SST and SSH, they have different objectives.

Finally, it is interesting to compare our results with the previous study of Isern-Fontanet *et al.* (2006). They investigated the application of the eSQG approach to microwave SST in approximately the same area of the GS (37N-48N 51W-35W) as the one selected in section 5.3. In their study they did not investigate the temporal evolution of correlation but rather estimated the mean correlation. They showed that the thermal gradients played a role in the capability of reconstructing the flow. In fact, when the correlations were estimated for strong gradients, they improved significantly (0.71 for zonal velocity and 0.69 for meridional velocity). If the combined method is applied to the same area, the mean correlations , taking into account the whole image, are similar to the eSQG correlations estimated for strong gradients (0.7 for zonal velocity and 0.63 for meridional velocity). However, mean correlations for the combined stream function increased up to 0.8 for strong gradients. A possible explanation of this could be the low sensitivity of microwave radiometers to detect thermal gradients (Robinson, 2004; Chelton & Wentz, 2005).

5.8 Conclusions

In this chapter we have found that SST provided by microwave radiometers can be used to retrieve ocean currents during winter, near the major extratropical current systems, which are characterized by an intense mesoscale activity and the presence of strong thermal gradients. We have also found that surface ocean current reconstruction based on eSQG approach can be improved if the information about the energy spectrum provided by altimeters is used. On the one hand, this suggests that the direct application of the eSQG approach may not be entirely accurate. On the other hand, this points to the potential development of a new method of reconstructing ocean currents based on the combination of the phase of SST images with the

energy spectrum derived from along-track altimeteric measurements.

Chapter 6

Mean transfer function

In the previous chapter, it was shown that the reconstruction of ocean surface currents from microwave SST observations using the eSQG approach can be significantly improved when the information from the spectrum of SSH is used (see chapter 5). This result additionally suggests that the transfer function between SST and SSH does not necessarily follow the eSQG predictions. In order to further investigate this deviation, the aim of this chapter is to analyse the spectral properties of the transfer function between SST and SSH. For this purpose, a mean transfer function for each of the analysed boxes is computed based on the results presented in the last chapter. Once the spectral properties of the mean transfer function are characterized, the reconstruction of ocean surface currents from this characterized mean transfer function is then evaluated by comparing it with geostrophic ocean currents retrieved from altimetry measurements.

6.1 Spectral characterization of the mean transfer function

From a dynamic point of view, the spectrum of the velocity field represents the distribution of kinetic energy within a range of spatial scales and is a tool used largely in order to characterize the underlying dynamic processes. Under the geostrophic balance, it is possible to relate the kinetic energy with the SSH (see section 2.2). In this context the spectral slopes of SSH altimetric observations have been widely used to further investigate ocean surface dynamics (Le Traon *et al.* , 2008; Xu & Fu, 2011, 2012). In a similar way, the aim of this chapter is to further investigate the spectral properties of the transfer function (denoted as TF from now on) between the SST and the SSH. In this sense, it is worth recalling that the validity of the SQG approach in terms of the TF implies a spectral slope of k^{-1}, see equation (2.69).

As it was seen in section 2.5, the total solution to the PV inversion problem at the ocean surface can be written using the formalism of a TF as:

$$\hat{\psi}(\vec{k}) = F_T(k) e^{i\Delta\theta_T(\vec{k})} \hat{T}_s(\vec{k}), \tag{6.1}$$

where $F_T(k)$ is the amplitude of the TF:

$$F_T(k) = \frac{g}{f_0}\frac{\langle|\hat{\eta}|\rangle_k}{\langle|\hat{T}_s|\rangle_k}, \tag{6.2}$$

where $\langle\cdot\rangle_k$ indicates that the average is taken over those wavevectors with the same modulus. And the term $\Delta\theta_T(\vec{k})$ accounts for the phase shift between SST and the stream function, as in Isern-Fontanet *et al.* (2014):

$$\Delta\theta_T(\vec{k}) = \arccos\left[\frac{\Re(\hat{\eta}\hat{T}_s^*)}{|\hat{\eta}||\hat{T}_s|}\right], \tag{6.3}$$

where * indicates the complex conjugate.

It is interesting to note that in the study presented in the last chapter, the stream function was constructed by imposing the spectrum of the reference field i.e. SSH, on SST. This would imply that, we were actually comparing the phase of the SST measurements with the phase of altimetric maps. Consequently, the combined approach performs better when the phase of the SST properly reflects the oceanic structures detected by altimeters, which means that the phase shift $\Delta\theta_T(\vec{k})$ was minimal. Thus, the mean TF was computed taking into account only the days in which the phase shift were smaller, based on the results obtained in the last chapter. For that purpose, the mean transfer function for each box was computed by averaging in the wavenumber domain daily transfer functions for those days with combined correlations higher than 0.85.

Table 6.1: Estimated spectral slopes of sample boxes Spectral slope estimated in the wavelength range [100-400km] (α) and [100-250km] (α_H)

	longitude		latitude			
Box	min	max	min	max	$\alpha \pm \sigma_\alpha$	$\alpha_H \pm \sigma_{\alpha_H}$
GS	41.16°	48.03°	−41.00°	−31.00°	-0.61±0.38	-1.04±1.22
ACC	−48, 12°	−41.12°	−30.63°	−20.67°	-0.75±0.42	-0.89 ±0.81
Agulhas	−40.97°	−33.78°	27.69°	36.92°	-0.66±0.29	-0.67±0.87
Kuroshio	33.78°	40.97°	147.69°	156.92°	-0.71±0.41	-0.75±0.8

The mean transfer function and the mean phase shift for the four selected boxes (see Table 6.1) are presented in Figure 6.1 and 6.2, respectively. For most boxes, the spectrum of the mean transfer function presents a unique negative slope for scales between 400 and 100 km. This is, indeed, the case with the ACC, Kuroshio and Agulhas boxes. However, there are a few exceptions in which the spectrum of the mean transfer function presents two well-differentiated spectral slopes, as in the case of the GS box (Figure 6.1). Figure 6.2 reveals that at larger scales the phase shift is smaller. The shift remains important, however, particularly for the cases of the GS and Kuroshio boxes, where the minimum phase shift of the mean TF is slightly lower than $\pi/3$.

The spectral slopes α of the mean transfer function were computed via a least squares fit of a power law between 400 and 100 km for each box. The selected wavelength range (100-400 km)

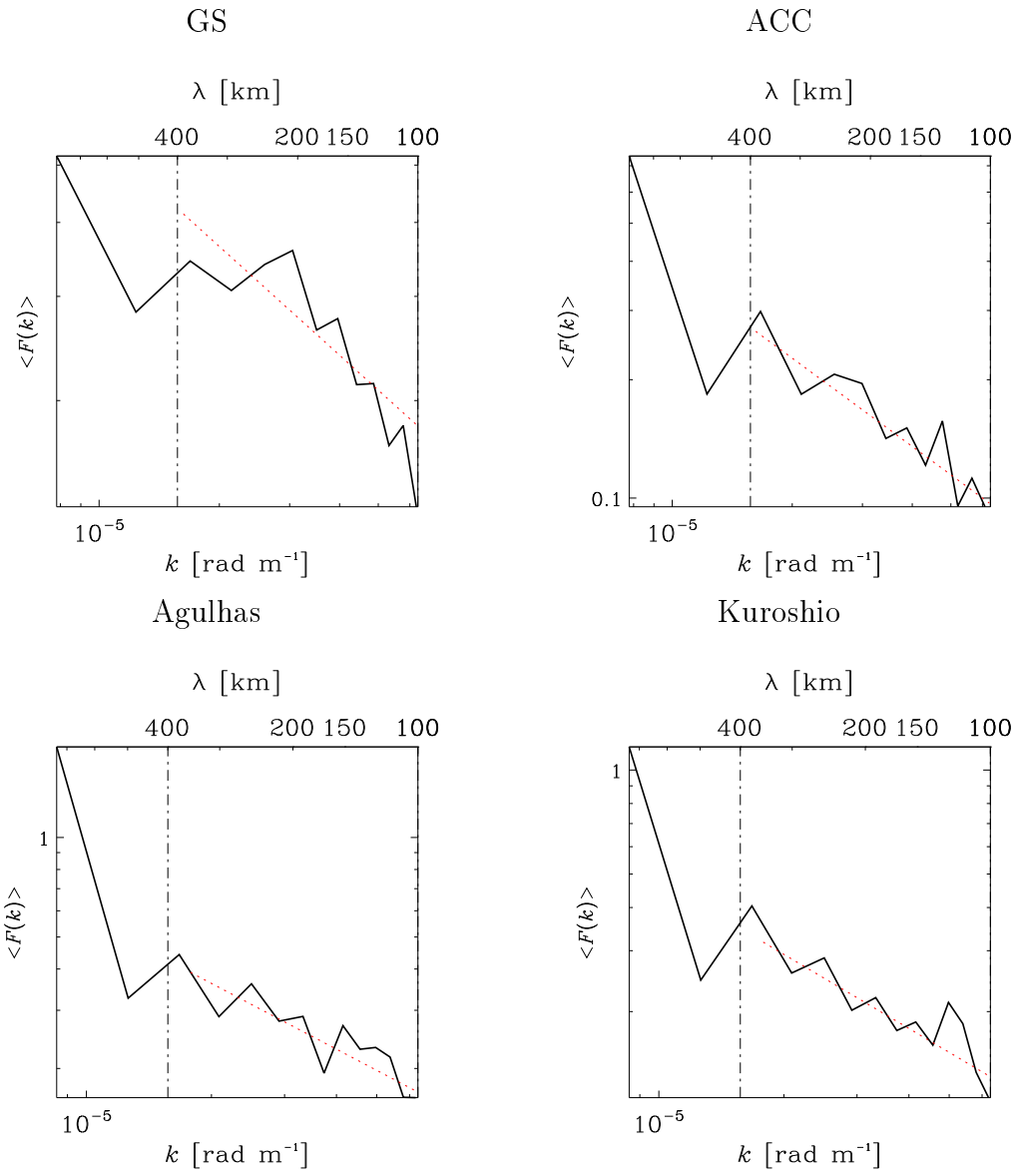

Figure 6.1: Amplitude of the mean transfer function. Amplitude of the mean transfer function (black solid line) and k^{α} model (red dotted line). From top to bottom and left to right: GS, ACC, Agulhas and Kuroshio Current box (see Table 6.1)

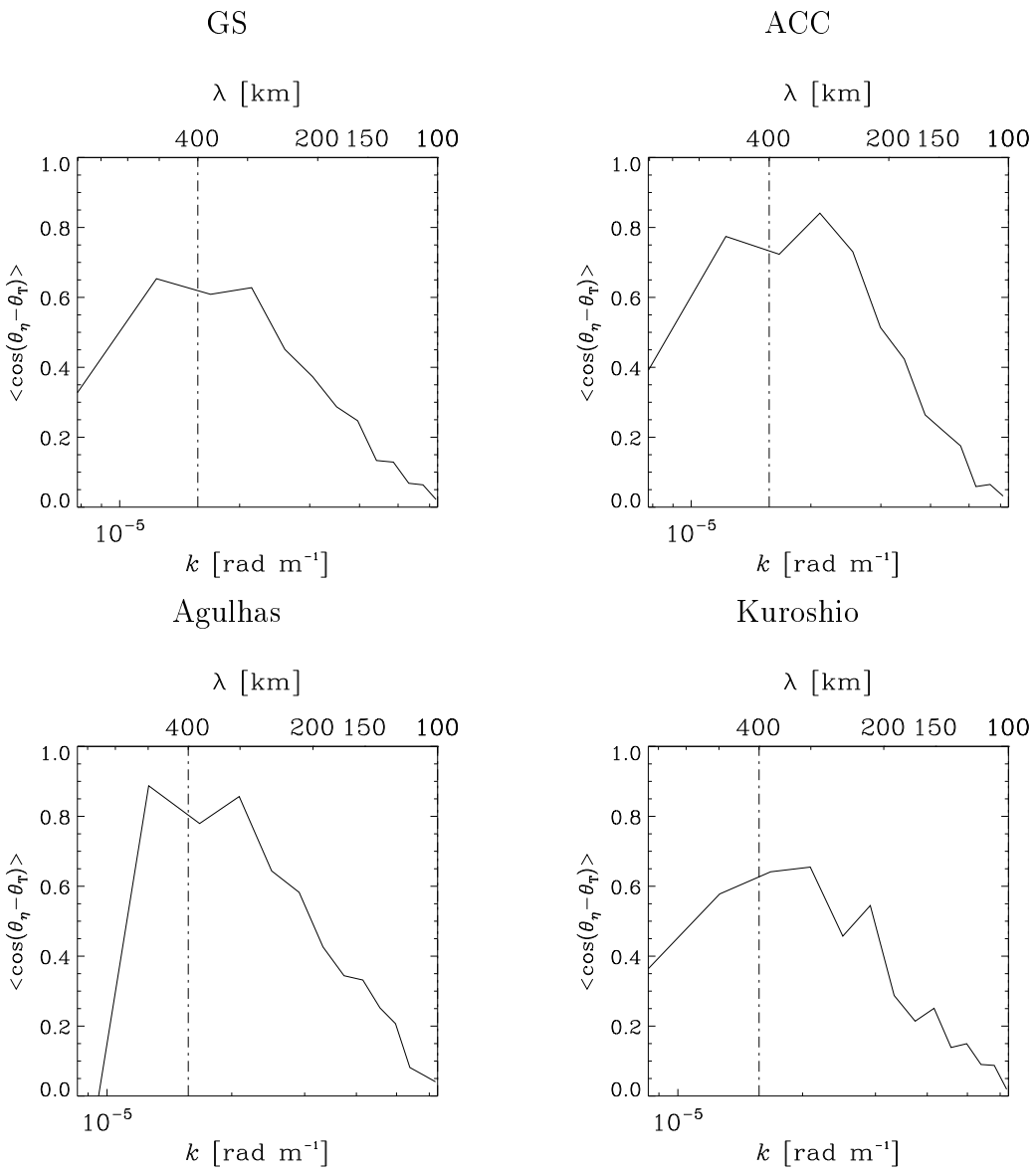

Figure 6.2: Mean phase correlation. From top to bottom and left to right: GS, ACC, Agulhas and Kuroshio Current box (see Table 6.1)

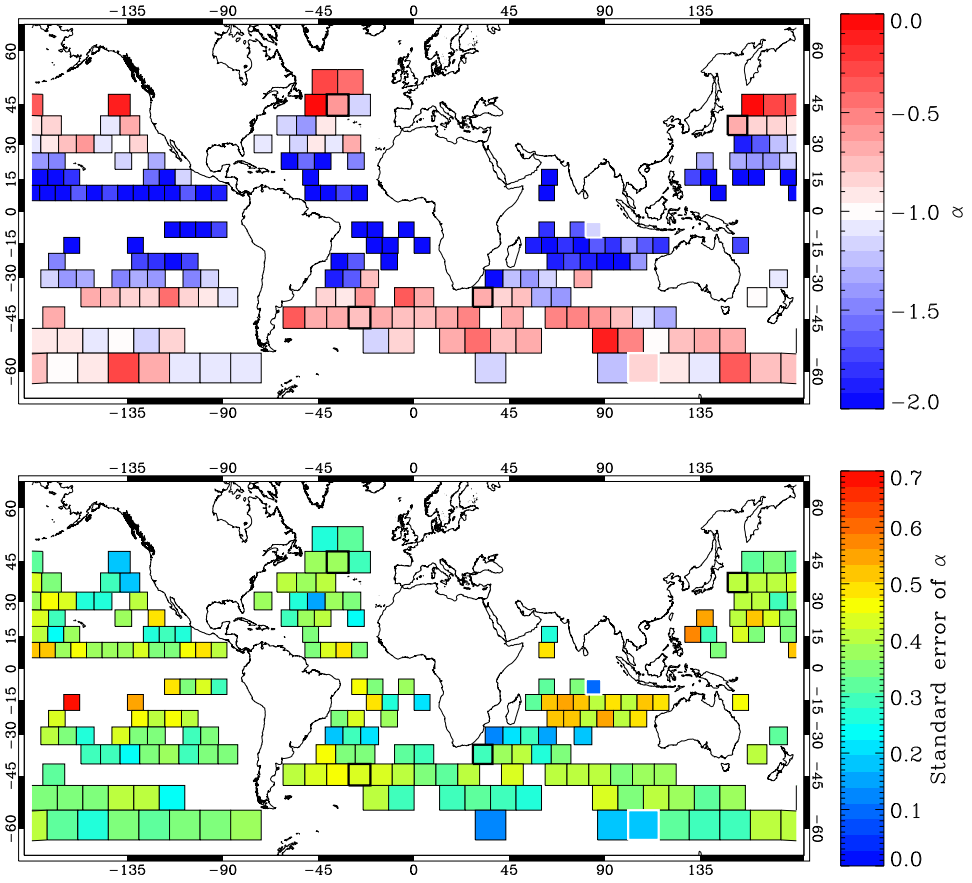

Figure 6.3: Spectral slope of the mean transfer function. Top: spectral slope α. Bottom: Standard error of α. Wide black lines delimite the selected boxes: GS, ACC, Agulhas and Kuroshio (see table 6.1) and wide white lines delimit boxes in which goodness-of-fit is poor (see Appendix B).

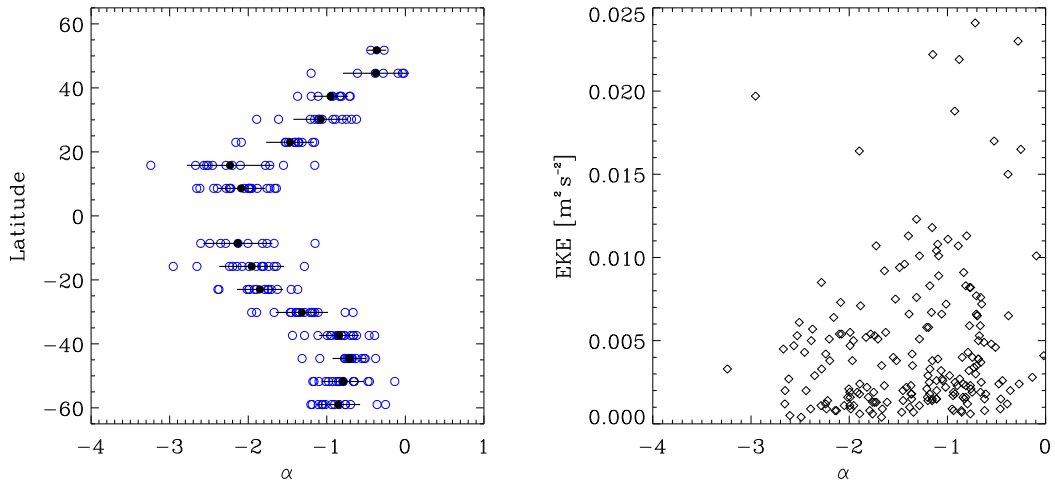

Figure 6.4: Latitudinal variation of the spectral slope α and Spectral slope vs EKE. Left: Spectral slope (α) as a function of latitude. Blue circles indicate the spectral slope of each box. Black filled circles show the mean spectral slope per latitude and the bar shows the standard deviation per latitude. Right: Scatter plot of the estimated spectral slope (α) versus Eddie Kinetic Energy

to compute the spectral slope is the same one as in the previous chapter. The 100 km represents a lower limit, below which the spectrum of altimetric data is dominated by measurement noise (Xu & Fu, 2011). The 400 km upper limit is selected to focus on the mesoscale part of the ocean turbulence. Results shown in Figure 6.3 reveal a spectral slope slightly flatter than the k^{-1} power law predicted by SQG theory at high latitudes. Near the major extratropic current systems like the Gulf stream, the Antarctic Circumpolar Current, or the Kuroshio, the spectral slope is approximately between -0.6 and -0.75 (see table 6.1). Boxes located at low latitudes present a steeper spectral slope of between -1.5 and -2. The standard error of the estimated spectral slopes provided in Figure 6.3 is, in most of cases, of the same order as the spectral slopes (for more details on the estimation of the standard error see Appendix B). Table 6.1 summarizes the estimated spectral slopes and the standard error of the four selected boxes, whose mean transfer functions were presented in the last section.

To further investigate the latitudinal variation of the spectral slope, we computed its latitudinal mean. Results shown in Figure 6.4 reveal that the spectral slope of boxes located in the Southern hemisphere are closer to k^{-1} than are boxes located in the Northern hemisphere. Boxes that present a spectral slope near k^{-1} in the Southern hemisphere are in a latitude range between 60°S and 37°S, whereas in the northern hemisphere this range is from 30°N to 40°N.

The comparison of the spectral slopes with the mean Eddie Kinetic Energy shown in Figure 6.4 suggests that the mean TF is closer to the k^{-1} spectral slope predicted by SQG theory in high energy regions, whereas low energetic regions present a transfer function steeper than k^{-1}.

The flatter response of the mean TF for larger scales of the GS box and other cases not shown, led us to re-compute the spectral slope of the mean TF for smaller scales. The spectral

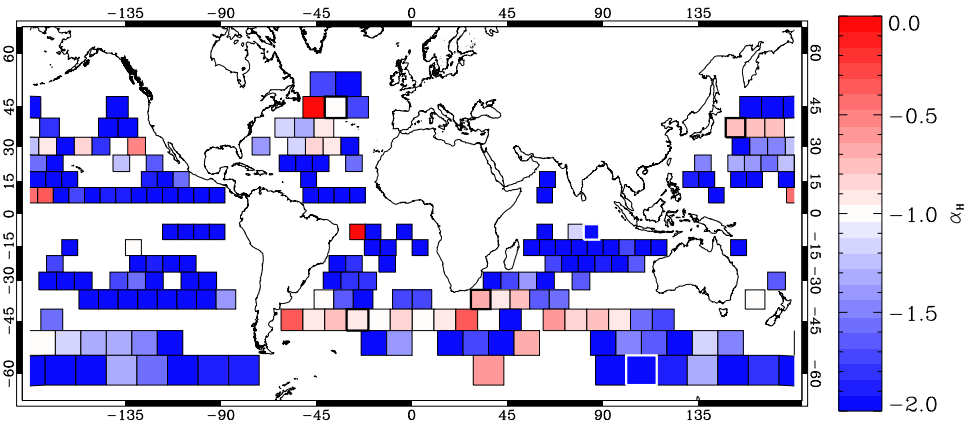

Figure 6.5: High frequency spectral slope of the mean TF. High frequency spectral slope α_H of the mean transfer function, computed in the range [100km-250km]. Wide lines delimite the selected boxes: GS, ACC, Agulhas and Kuroshio (see table 6.1)

slopes computed in the wavelength range [100-250 km], (Figure 6.5) are generally steeper than those computed taking in to account a wider range (Figure 6.3). This is particularly true in the case of the GS and ACC where the spectral slope is closer to k^{-1}. For the Kuroshio and Agulhas boxes the spectral slope in the higher wavenumber range (denoted as α_H in table 6.1) is similar to the one previously shown for a wider range.

6.2 Flow reconstruction from characterized mean TF

The performance of the flow from daily microwave SST observations by means of a TF that follows a k^{α} model inspired by the family of two-dimensional fluid models proposed by (Pierrehumbert *et al.* , 1994) is evaluated using the spectral slopes estimated in the last section. With this purpose in mind, its performance is compared to the flow reconstructed from altimetric observations, by computing spatial correlation coefficients. The obtained correlations for all variables of the flow: the stream function, both components of the velocity field and the vorticity are compared to the correlations obtained from the eSQG approach. Results shown in Figure 6.6 reveal that the reconstruction in terms of the mean transfer function does not significantly improve eSQG reconstruction. However, for correlations higher than 0.85, the stream function retrieved from mean transfer function presents higher correlations than that retrieved using the eSQG approach in the 51.9 % of the cases. This percentage is reduced to 30.5 % and 22.5 % for longitudinal and meridional components of the velocity field, respectively.

In order to identify the regions where the reconstruction of the flow by the mean transfer function slightly improves the flow reconstruction from eSQG, the mean difference per box

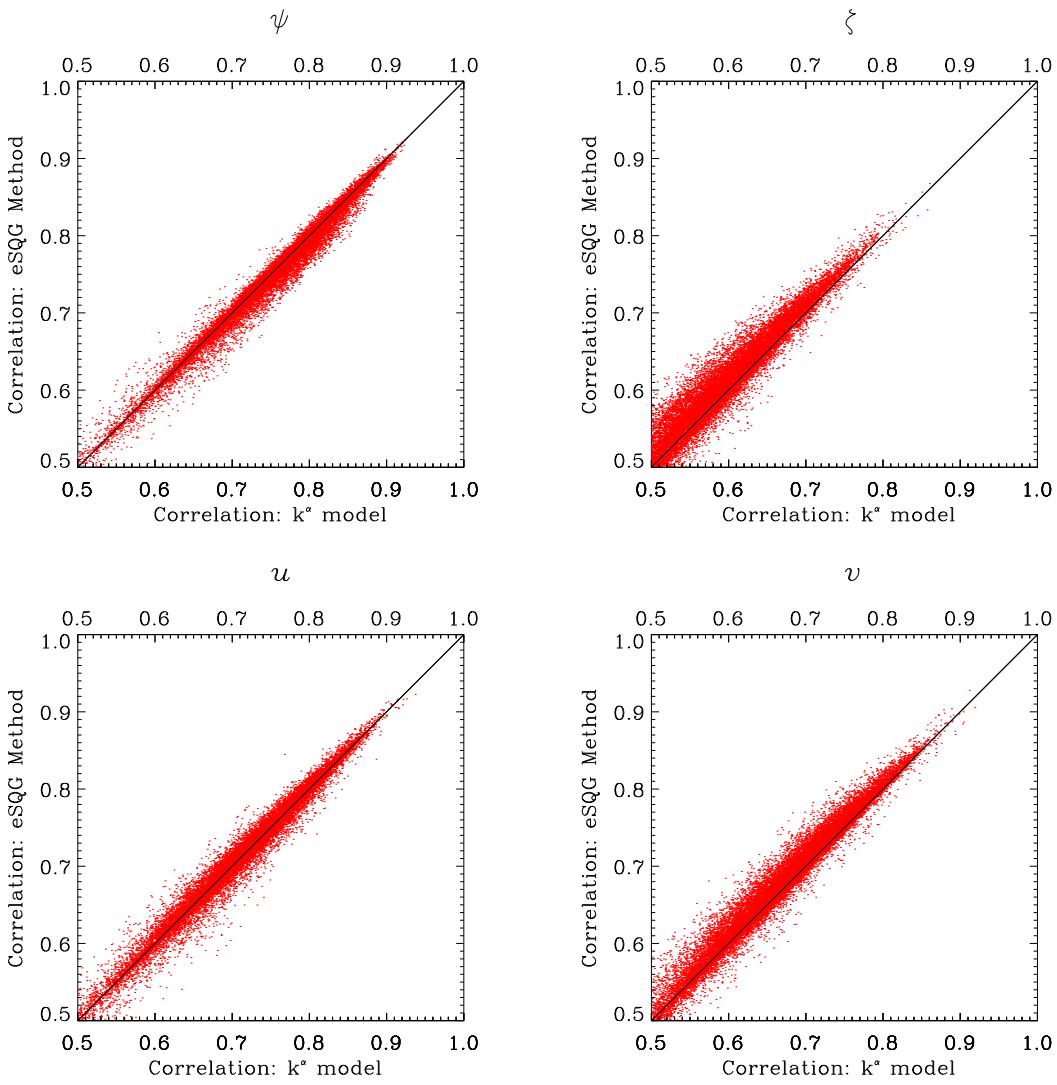

Figure 6.6: Comparison of flow reconstruction: eSQG vs k$^{\alpha}$ models. Scatter plot of correlations of variables retrieved from eSQG and k$^{\alpha}$ model. All correlations take as reference variables retrieved from SSH. Variables shown from top to bottom and left to right: stream function (ψ) , vorticity (ζ), zonal (u) and meridional (v) velocity components.

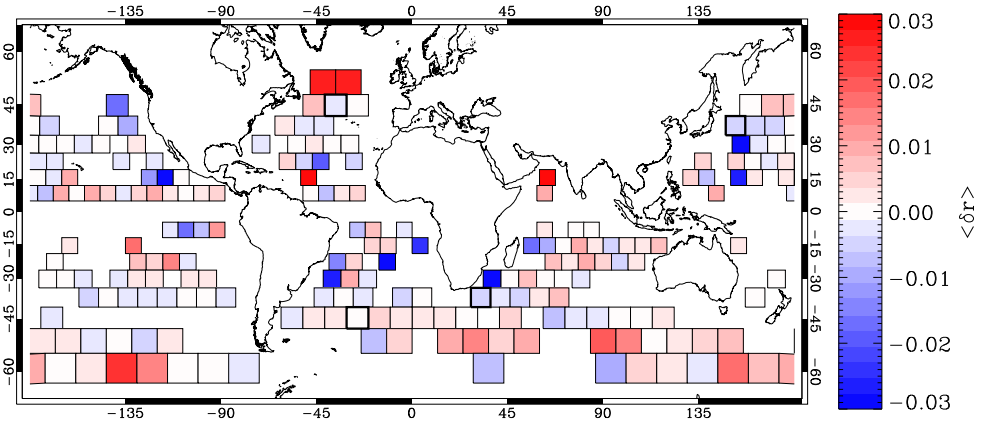

Figure 6.7: Difference between the k$^\alpha$ and eSQG stream function correlations. Mean difference between the k$^\alpha$ stream function correlation and eSQG stream function correlation.

Table 6.2: Velocity reconstruction performance: Correlation between the retrieved velocity components from altimetric observations and from SST observations by: the combined approach, the eSQG approach and the k^α mean transfer function.

	combined		eSQG		k^α	
Box	u	v	u	v	u	v
GS	0.82	0.78	0.68	0.67	0.67	0.65
ACC	0.85	0.83	0.74	0.75	0.74	0.74
Agulhas	0.83	0.75	0.70	0.61	0.67	0.60
Kuroshio	0.81	0.72	0.64	0.57	0.63	0.56

between both correlations is computed as:

$$< \delta r >=< r_\alpha - r_{-1} >, \tag{6.4}$$

where r_α is the correlation between the stream function retrieved by the mean transfer function and the stream function computed from altimetry observations, and r_{-1} is the correlation between stream function retrieved using the eSQG approach and stream function computed from altimetey. Only days with combined correlations higher than 0.85 were considered to compute the mean difference (6.4). Indeed, the same days whose TF were averaged to compute the mean TF are taken into account in order to compute the mean difference correlation. Figure 6.7 indicates that even in regions where the spectral slope is steeper than the k^{-1}, the flow reconstruction performance of the characterized mean transfer function is similar to the performance of flow reconstruction by means of the eSQG approach. This result leads us to raise questions about the sensitivity of the spectral slope in the flow reconstruction.

The performance of the velocity field reconstruction from the mean characterized TF is compared to the performance of the other two reconstruction approaches presented in the last chapter: (i) the combined approach, which uses simultaneous information from SST and SSH observations, and (ii) the eSQG approach. Table 6.2 shows the correlation between the retrieved velocity components for the three methods, and the velocity components retrieved from altimetric observations for the same days that were taken into account when estimating the spectral slope in the last section. Results show that the reconstruction from the eSQG approach and from a mean k^{α} model have similar performances, which can be further enhanced by using simultaneous SST and SSH observations (combined approach).

6.3 Discussion

The spectral slope of the mean transfer function between SST and SSH observations was estimated at a global scale. Results revealed a mean transfer function spectra flatter than the theoretical k^{-1} eSQG transfer function in boxes located at high latitudes and near the major extratropic current systems. A priori, and based on the analysis of the validation of the eSQG approach presented in the last chapter, a transfer function closer to k^{-1} would be expected in these regions. Previous theoretical (Lapeyre & Klein, 2006a; Lapeyre, 2009; Klein & Hua, 1990) and recent numerical studies (Isern-Fontanet *et al.* , 2014) have already unveiled deviations from the eSQG predictions, particularly for large scales. The slight deviation of the transfer function from a eSQG model could be due to a flatter response of the larger scales, as observed in the case of the GS box (Figure 6.1). Indeed, a similar study conducted in the Mediterranean Sea using numerical simulations (Isern-Fontanet *et al.* , 2014) revealed an eSQG-like slope transfer function for small scales and a flat response for high scales in most analysed basins. This motivated us to recompute the spectral slope of the mean transfer function for high wavenumbers (α_H), that is, for wavelengths in the range of [100-250 km]. Results shown in Figure 6.5 reveal steeper spectral slopes than the ones computed taking into account a wider wavelength range (Figure 6.3). In that case, a slope k^{-1} predicted by the eSQG theory is obtained in most of boxes located in the ACC and GS regions, whereas a flatter spectral slope is still observed in the Kuroshio region.

Another aspect that influences the estimation of the spectral slope is the size of the box. It limits the maximum wavelength to be resolved and the spectral resolution, specifically for low wavenumbers. In order to study the impact of the size of the boxes, we redefined the limits of the boxes by doubling their size up to 1600 km $\times$ 1600 km, but keeping the same mid latitude and longitude. The spectral slope for each box was then recomputed, following the same procedure described in section 6.1. The new estimated spectral slopes changed slightly as compared to the ones previously estimated (see Figure 6.8). In fact, the correlation coefficient between them is 0.88. It goes without saying, however, that doubling the size of the box obviously has an impact on the standard error of the estimated spectral slope, which is reduced by a factor of between 1.5 and 2. This result indicates that there is a correlation between TF computed from the two different sizes. Otherwise, the standard error should theoretically be reduced by a factor of 2,

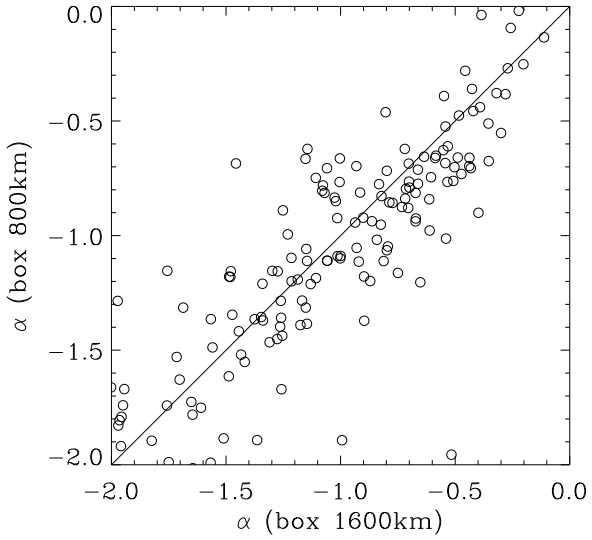

Figure 6.8: Impact of the size of the box on the spectral slope estimation. Scatter plot of estimated spectral slopes for 800 km side boxes versus spectral slopes for 1600 km side boxes.

since the box is 2^2 higher. Another effect of increasing the size of the box, and consequently the spectral resolution or the number of data points in the low wavenumber range, is that in some cases the change of slope at low scales is less evident than for a smaller box, such as the GS. Conversely, in cases where a unique spectral slope was observed for smaller cases in the wavelengths range between [100-400 km], the mean TF computed for a larger box now presents two well-differenciated spectral slopes, as in the case of ACC box (see Figure 6.9).

Turbulence theories are usually validated in the wavenumber domain by computing the spectral slope of the kinetic energy. In this sense, altimetric observations provide measurements of kinetic energy and have been used for that purpose. The validity of the SQG approach implies an energy spectrum with slopes as $k^{-5/3}$ (Blumen, 1978), and a spectrum as $k^{-11/3}$ for Sea Surface Height (SSH). Le Traon *et al.* (2008) showed that spectral slopes in the mesoscale band in high energetic areas are significantly different from a k^{-5} law, predicted by Quasi-Geostrophic turbulence, but they very closely follow the $k^{-11/3}$ slope, which indicates that the surface SQG is a much better dynamical framework than the QG turbulence theory to describe the ocean surface dynamics. This was confirmed by Xu & Fu (2011), who evaluate the SSH wavenumber spectrum on a global scale from altimetric observations. However, results in low energy areas revealed shallower slopes. In a later study, Xu & Fu (2012) investigated the effect of altimeter instrument noise on the estimation of the wavenumber spectral slope. They found that spectral slopes became significantly steeper after removing the noise. Sasaki & Klein (2012) further investigated the SSH wavenumber spectra in the North Pacific using numerical simulations and showed that even in low energy areas SSH had spectra of the type k^{-4}, close to SQG predictions,

and suggested that instrumental noise could hide such slopes. Furthermore, they showed that the scales for which the k^{-4} slope could be seen depends on the energy level. The spectral analysis of the TF function between SST and SSH shown in this chapter suggest that the TF presents an spectral slope close to a k^{-1} as the SQG theory predicts, but slightly flatter in energetic regions. The estimated spectral slope was closer to k^{-1} in energetic regions if its was estimated in a lower wavelengths range.

The analysis of the performance of the flow reconstruction in terms of a mean transfer function revealed that it does not significantly improve the reconstruction from an eSQG approach. This could be due to the fact that a mean transfer function may not adequately reproduce the variability of the transfer function spectra. In fact, Isern-Fontanet *et al.* (2014) found that the different response in transfer function originates from a different slope of SSH (see their figure 8). Clearly, further work should be carried out in order to study the temporal variability of the spectral slope and its sensitivity to the flow reconstruction by a k^{α} transfer function model. This result also suggests that the SQG reconstruction is statistically a good approach to retrieve surface ocean currents when no simultaneous SST and SSH observations are available.

Finally, after a qualitative inspection of the mean transfer frequency response of all boxes, we found that it resembles the amplitude, or gain, of the frequency response of a low-pass filter. In some cases, the frequency response of the mean transfer function decades 20 dB per decade, which then behaves as a first-order low-pass filter. In fact, the gain of the frequency response of a first-order Butterworth low pass filter

$$G^2(\omega) = \frac{1}{1 + \left(\frac{\omega}{\omega_c}\right)^2} \tag{6.5}$$

is comparable to the interior contribution to the total solution of the PV inversion, equation (2.59); where w_c is the cut-off frequency, at which energy flowing through the system begins to be reduced rather than passing through. Typically, it is defined as the frequency at which the output of the system is -3dB of the nominal input. Such a model would also fit in with the two-differentiated spectral slope transfer function unveiled by (Isern-Fontanet *et al.* , 2014). It opens the door to considerig new models which could adjust the transfer function between SST and SSH.

6.4 Conclusions

The spectral properties of the mean transfer function between SST and SSH observations were characterized at a global scale. The estimated spectral slope of the mean transfer was slightly flatter than SQG slope in energetic regions near the major extratropic current system, whereas in the tropical regions it was steeper, around k^{-2}. However, when evaluating the performance of the flow reconstruction in terms of the mean transfer function, it did not significantly improve the reconstruction based on the eSQG approach in any particular region. Thus, further work should be carried out in order to investigate the the temporal variability and sensitivity of the

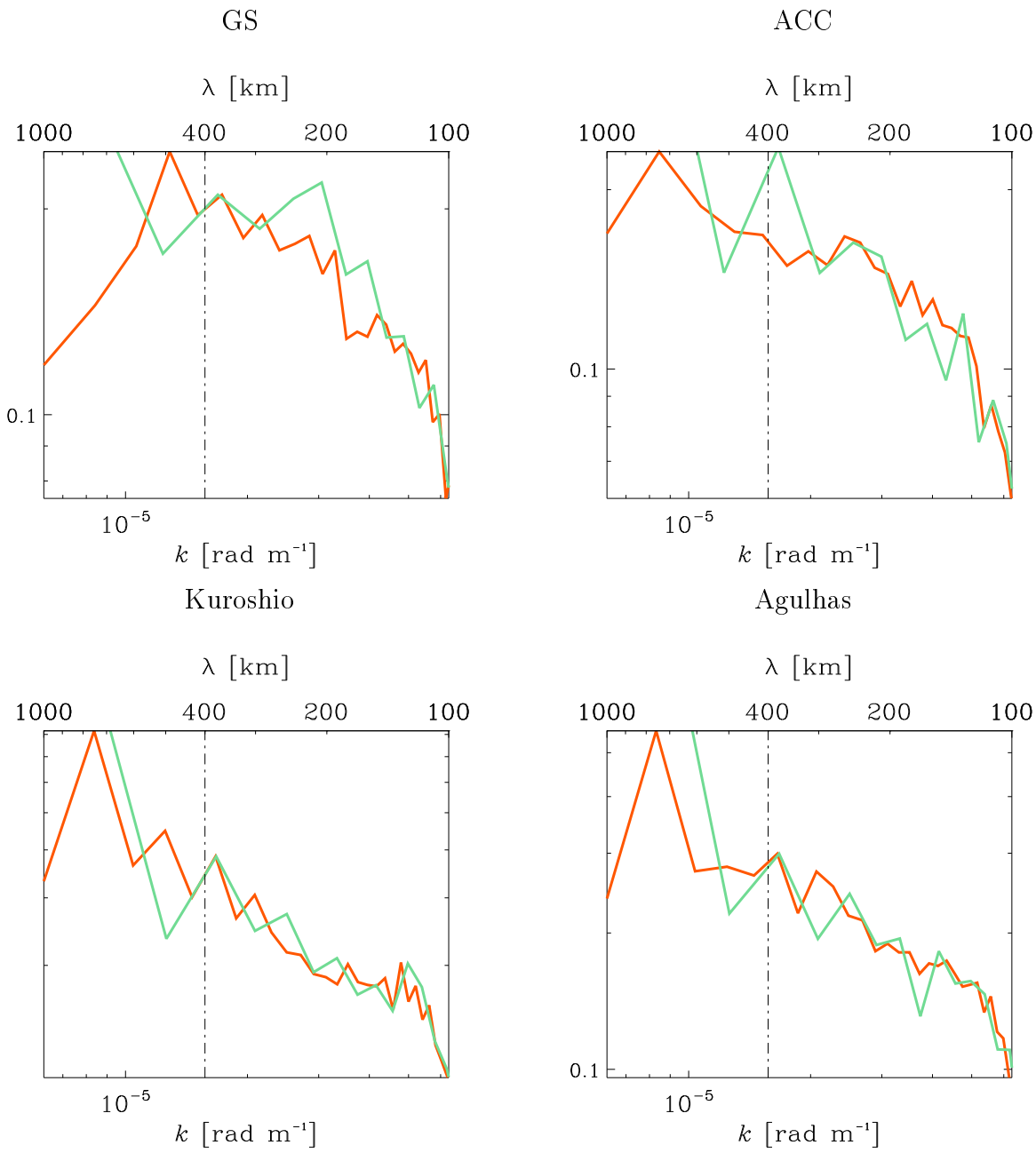

Figure 6.9: Impact of the size of the box in the spectral slope estimation. Mean transfer function for boxes of 800km (green thick line) and for boxes of 1600 km (orange thick line). From left to right and top to bottom: GS, ACC, Agulhas, and Kuroshio (see table 6.1)

spectral slope (α) in the flow reconstruction, in terms of a transfer function that follows a k^{α} model in the wavenumber space.

Chapter 7

Instantaneous Transfer Function

In the last chapter, the spectral properties of a mean transfer function were characterized as a first attempt at developing the capability to reconstruct ocean currents from SST observations shown in Chapter 5. However, the evaluation of the performance of the flow reconstruction showed that the retrieval from a modelled mean transfer function did not improve the reconstruction using the eSQG approach. The aim of this chapter is to further investigate to which extent this low performance may be due to the fact that a mean transfer function cannot reproduce the temporal variability of the transfer function. In this context, the spectral properties of the transfer function are daily characterized. In addition, we propose and evaluate an adjustment of the spectral slope in the real domain using two different metrics. The first metric being the maximization of correlation between the flow reconstructed from SST by the transfer function and the flow retrieved from SSH altimetric observations; the second being the minimization of the RMSE of both flows.

7.1 Spectral analysis

The temporal evolution of the phase shift between SST and SSH as a function of k was investigated using a spectral correlation coefficient $r(k)$ based on equation (6.3),

$$r(k) \equiv \langle \cos \Delta\theta_T \rangle_k. \tag{7.1}$$

Despite performing the spectral analysis for all defined boxes, only the temporal evolution of the spectral properties for the sample boxes allocated in the GS and ACC currents are shown in Figures 7.1 and 7.2, respectively. Results for both boxes revealed smaller shifts for scales longer than 200 km. Nevertheless, some differences can be appreciated. While in the case of the ACC these smaller shifts are present throughout the analysed period, in the case of the GS box the smaller phase shifts correspond to winter months (December-March). Although the phase shift at long wavelengths is smaller, it remains important. For spectral correlations $r(k)$ larger than 0.85 in the wavelength range between 400 km and 200km, the phase shift is between $\pi/18$ and $\pi/6$ in the case of the GS Box, whereas in the case of ACC box, the minimum phase shift

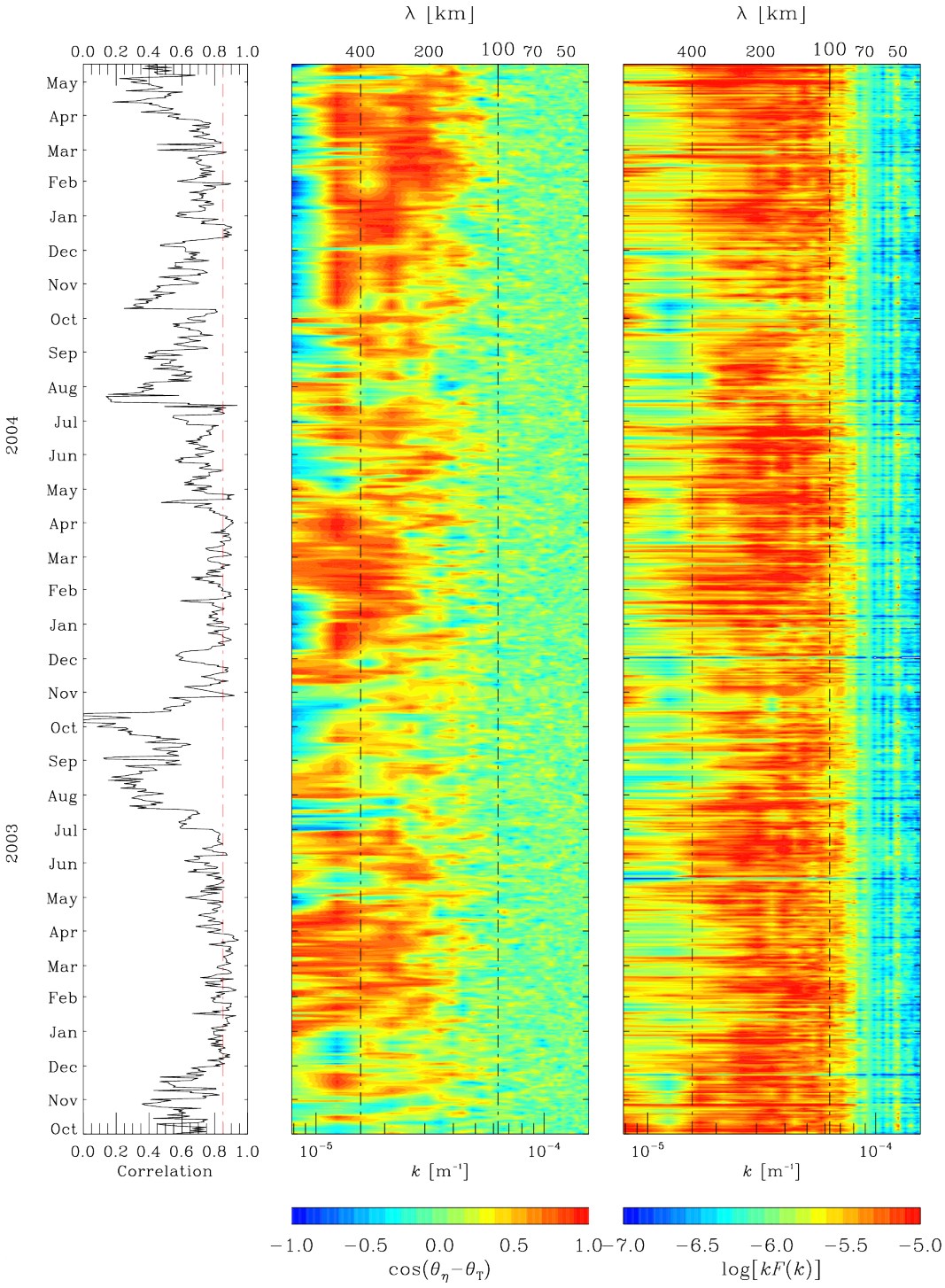

Figure 7.1: Temporal evolution of spectral properties of the TF (GS box) Left: Time series of correlations for the combined stream function between ψ_{CMB} and ψ_{alt}. Middle: Spectral correlation between SST and SSH. Right: Amplitude of the transfer function between SST and SSH. Results correspond to the Gulf Stream Current box (see table 6.1)

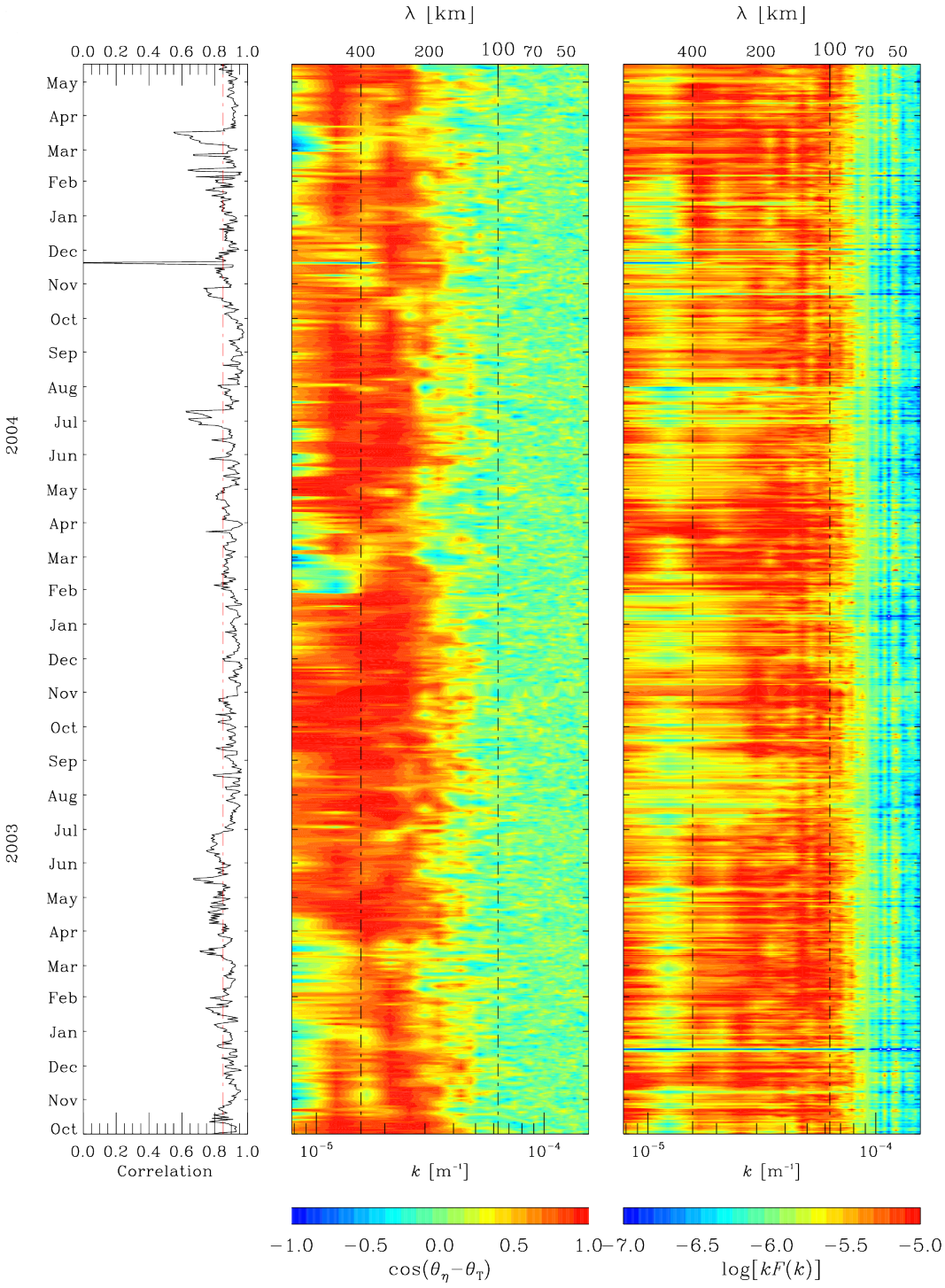

Figure 7.2: Temporal evolution of spectral properties of the TF: Left: Time series of correlations for the combined stream function between ψ_{CMB} and ψ_{alt}. Middle: Spectral correlation between SST and SSH. Right: Amplitude of the transfer function between SST and SSH. Results correspond to the box allocated in the ACC region (see table 6.1)

decreases to roughly zero ($\pi/36$). It is interesting to note that the period with smaller phase shifts corresponds to the period in which spatial correlations between combined and altimetry stream function where found to be higher as computed in chapter 5. These correlations are shown in the left plots of Figures 7.1 and 7.2. It is important to recall that the stream functions were band-pass filtered between 400 km and λ_{min} (100 km in these cases) before computing the spatial correlation coefficients, whereas, in the case of the phase shift and the modulus of transfer function between SST and SSH, no filtering was applied. Two vertical lines delimit the range of wavelengths that contribute to the temporal evolution of spatial correlations in Figures 7.1 and 7.2.

In addition to the phase shift, the characteristics and temporal evolution of the modulus of the transfer function were investigated. The amplitude of the transfer function $F_T(k)$ between SST and SSH is computed, as seen in the previous chapter, by averaging in spectral space over bands of constant wavenumbers k:

$$F_T(k) = \frac{g}{f_0} \frac{\langle |\hat{\eta}| \rangle_k}{\langle |\hat{T}_s| \rangle_k}, \tag{7.2}$$

where $\langle \cdot \rangle_k$ indicates that the average is taken over those wavevectors with the same amplitude. Results shown in Figures 7.1 and 7.2 reveal that the amplitude of the transfer function is characterized by negative slopes and presents an evident temporal variability. In order to further study the spectral properties of the modulus of the transfer function, the spectral slope of daily transfer function was estimated in the same way as in the previous chapter. That is, the spectral slope was computed via a least squares fit of a power law between 400 and 100 km. Once the spectral slopes were characterized daily, the flow was reconstructed using a transfer function that follows a k^α model, where α is the daily estimated spectral slope. Results will be presented in section 7.3

7.2 Daily spectral slope fit in the real domain

Since our objective is to retrieve the flow in real space, here the spectral slope was fit daily following two different metrics in the real domain: (i) maximizing the correlation between the flow retrieved by a k^α TF model, and the flow retrieved by altimetric observations, and (ii) minimizing the RMSE between these two flows. The flow was then reconstructed from daily SST observations by means of a k^α model, with α spreading from -5 to 1, with a 0.076 step. The two previous metrics were computed for each α step. Figure 7.3 illustrates the above described methodology for the box allocated in the GS region. The temporal evolution of the two metrics are shown as a function of the spectral slope. Also shown is the temporal evolution of the spectral slope which minimizes the RMSE and maximizes the correlation. In contrast to previous chapters, the variable here compared is the SSH, since its magnitude [m] is more intuitive than that of the stream function [m^2/s]. In fact, it is only relevant when using the RMSE metric, since the correlation is dimensionless and correlations of stream function are equivalent to those of SSH, as they are linearly related variables.

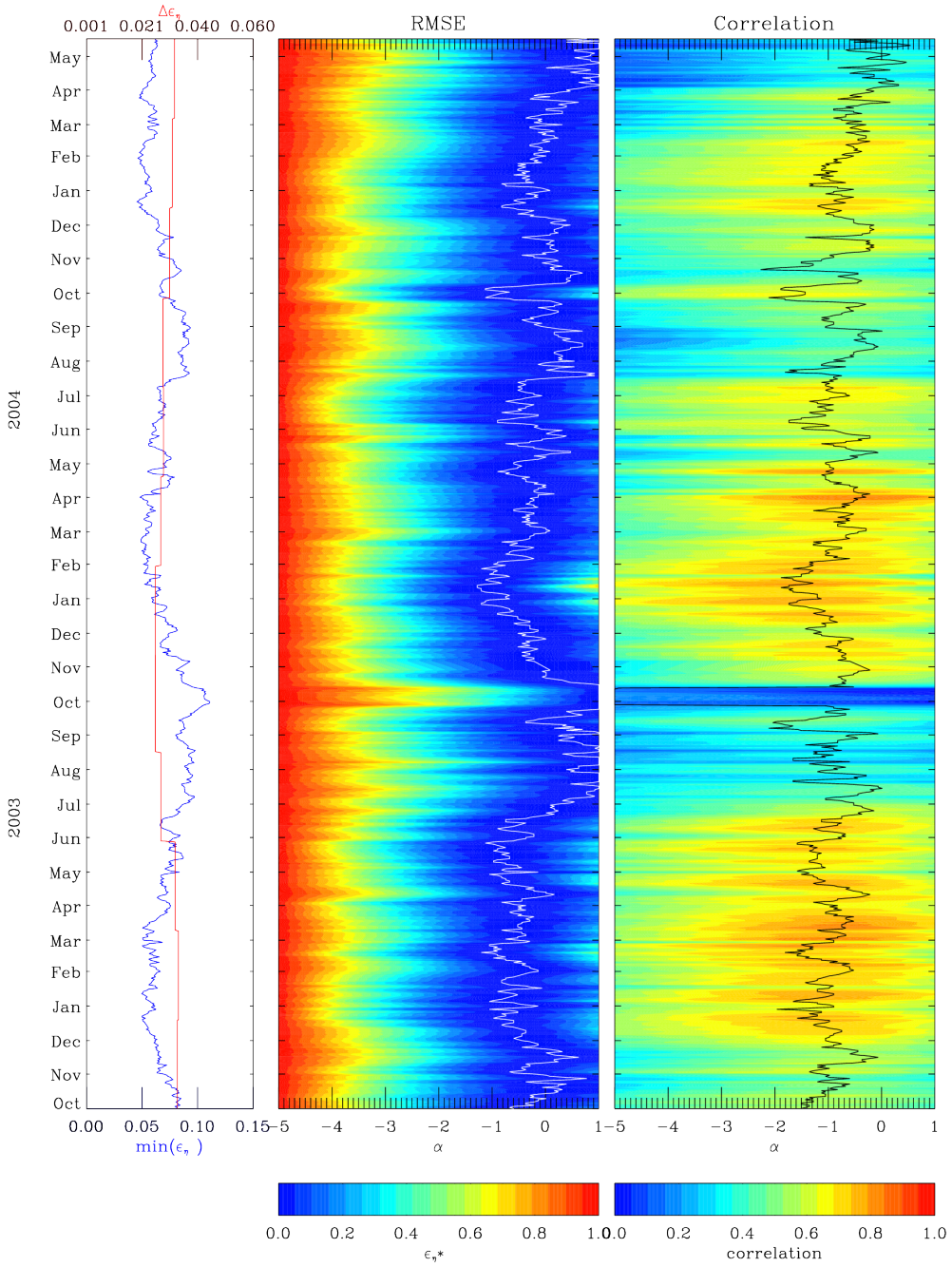

Figure 7.3: Temporal evolution of the metrics in real domain: Left: Time series for the minimum RMSE between η altimetry observations and SSH retrieved using the k^{α} model (blue) and difference between maximum and minimum RMSE (red). Middle: Normalized RMSE between η altimetry observations and SSH retrieved using the k^{α} model as a function of the spectral slope. The temporal evolution of the spectral slope which minimizes RMSE is plotted in white. Right: Correlation between η altimetry observations and SSH reconstructed using the k^{α} model. The temporal evolution of the spectral slope which maximizes correlation is shown in black. Results for **GS** box.

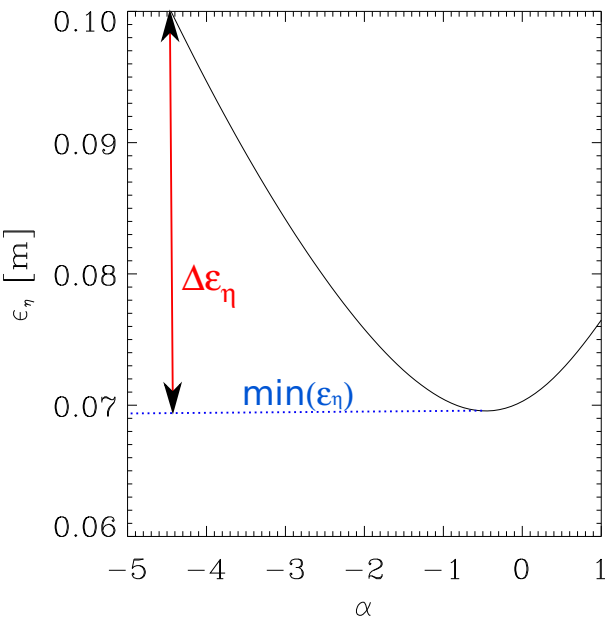

Figure 7.4: RMSE normalization. RMSE between SSH altimetry observations and SSH retrieved by the k^α model as a function of the spectral slope α.

It is worth noting, that due to the high temporal variability of the SSH RMSE, and in order to better observe the temporal evolution of SSH RMSE shown in Figure 7.3, it was normalized as:

$$\bar{\epsilon}_\eta = \frac{\epsilon_\eta - \min(\epsilon_\eta)}{\Delta\epsilon_\eta}, \tag{7.3}$$

where ϵ_η is the RMSE of SSH, $\bar{}$ denotes normalized and $\Delta\epsilon_\eta = \max(\epsilon_\eta) - \min(\epsilon_\eta)$. Figure 7.4 shows a daily profile of the SSH RMSE as a function of the spectral slope in order to exemplify the normalization that was daily performed.

The previous procedure was applied daily to the same boxes used in previous chapters. Thus, two different temporal sets of spectral slopes were obtained:

- α daily fit r_η: which maximizes the spatial correlation of SSH
- α daily fit ϵ_η: which minimizes the RMSE of SSH.

7.3 Daily flow reconstruction

The performance of the flow reconstruction by means of both fitted spectral slopes was assessed in the same way as in previous chapters. Figure 7.5 compares the reconstruction of the stream function by terms of a k^α model transfer function, taking into account the fitted spectral slopes in the real domain using the two different metrics proposed, with the reconstruction of the eSQG stream function. Results show that the flow reconstruction from the fitted spectral slopes slightly improve the eSQG reconstruction. In fact, Figure 7.5 is similar to Figure 6.6, the only difference being that in the case of Figure 7.5 all correlations are higher than the obtained correlations for

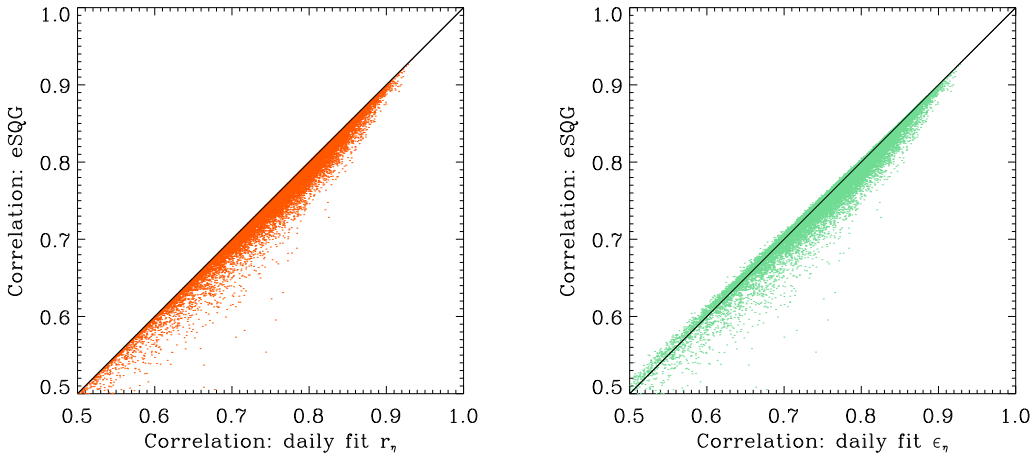

Figure 7.5: Comparison of reconstructed flow from two different metrics. Scatterplot of correlation between SSH retrieved by SQG and altimetry η observations versus correlation between altimetry η observations: and SSH retrieved by a k^α model considering: α which maximizes correlation (left) and α which minimizes RMSE (right).

eSQG reconstruction. This may be expected, since the spectral slope is fitted by maximizing the correlation between the retrieved field and altimetric observations. It is important to note that although a spectral slope was daily fitted using both previously describedv metrics, we only focused on days in which SST and SSH were closely in phase, based on the study performed in Chapter 5. For this reason, Figure 7.5 presents only the obtained correlations for those days on which the obtained correlation for the combined approach presented in Chapter 5 was higher than 0.85. Figure 7.5 reveals that the performance of the reconstructed flow by means of the spectral slopes fitted by the two metrics proposed is similar, although the spectral slopes fitted by minimizing the RMSE are slightly flatter than those fitted maximizing the correlation as shown in Figure 7.6. Indeed, for an estimated spectral slope of k^{-1} in the case of maximizing the correlation, a spectral slope of -0.5 can be retrieved in the case of minimizing the RMSE. This fact can also be observed in Figure 7.3 which shows the temporal evolution of the fitted spectral slopes using the two different metrics for the GS box. In this particular case, the mean spectral slope by maximizing the correlation is -0.82 and by minimizing the RMSE the mean spectral slope is found to be -0.49. Both metrics do, however, have similar performances when reconstructing the flow. For this reason, we will further analyse and focus on the flow reconstruction from spectral slopes fitted by maximizing correlation.

Maximizing correlation of different variables of the flow

Throughout this Ph.D. thesis the evaluation of the performance of the flow reconstruction has focused on the stream function, since velocity field and vorticity are derived from it, as shown

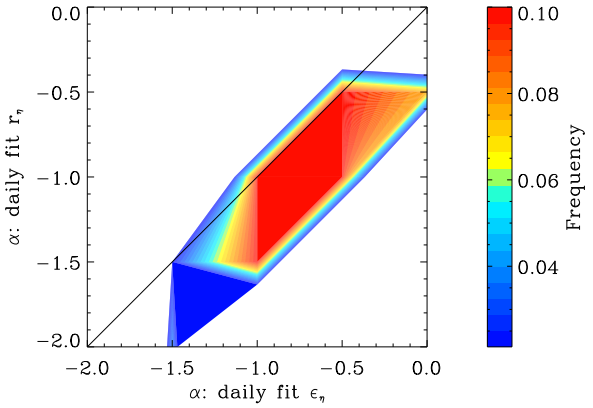

Figure 7.6: Comparison of spectral slopes fitted using two different metrics. 2D histogram of spectral slopes fitted by minimizing RMSE ϵ_η and by maximizing correlation r_η.

by:

$$\psi = \frac{g}{f_0}\eta, \tag{7.4}$$

$$u = -\frac{g}{f_0}\frac{\partial \psi}{\partial y}, \tag{7.5}$$

$$v = \frac{g}{f_0}\frac{\partial \psi}{\partial x}, \tag{7.6}$$

$$\zeta = -\frac{g}{f_0}\left(\frac{\partial^2 \psi}{\partial x^2} + \frac{\partial^2 \psi}{\partial y^2}\right). \tag{7.7}$$

Nevertheless, in this section we question to which extent the procedure for adjusting the spectral slope in the real domain, presented in the last section, depends on the variable of the flow selected to maximize its correlation with the same variable retrieved from altimetric observations. Accordingly, the spectral slopes were fit in the real domain following the procedure presented in the last section by maximizing the correlation of the stream function ψ, both velocity components, u and v, and vorticity ξ, obtaining four different temporal sets of spectral slopes denoted as:

- α daily fit r$_\psi$: which maximizes the spatial correlation of the stream function, and is, in fact, equivalent to α daily fit r$_\eta$ shown in the last section.
- α daily fit r$_u$: which maximizes the spatial correlation of the zonal component of the velocity field.
- α daily fit r$_v$: which maximizes the spatial correlation of the meridional component of the velocity field.
- α daily fit r$_\zeta$: which maximizes the spatial correlation of the meridional component of the vorticity.

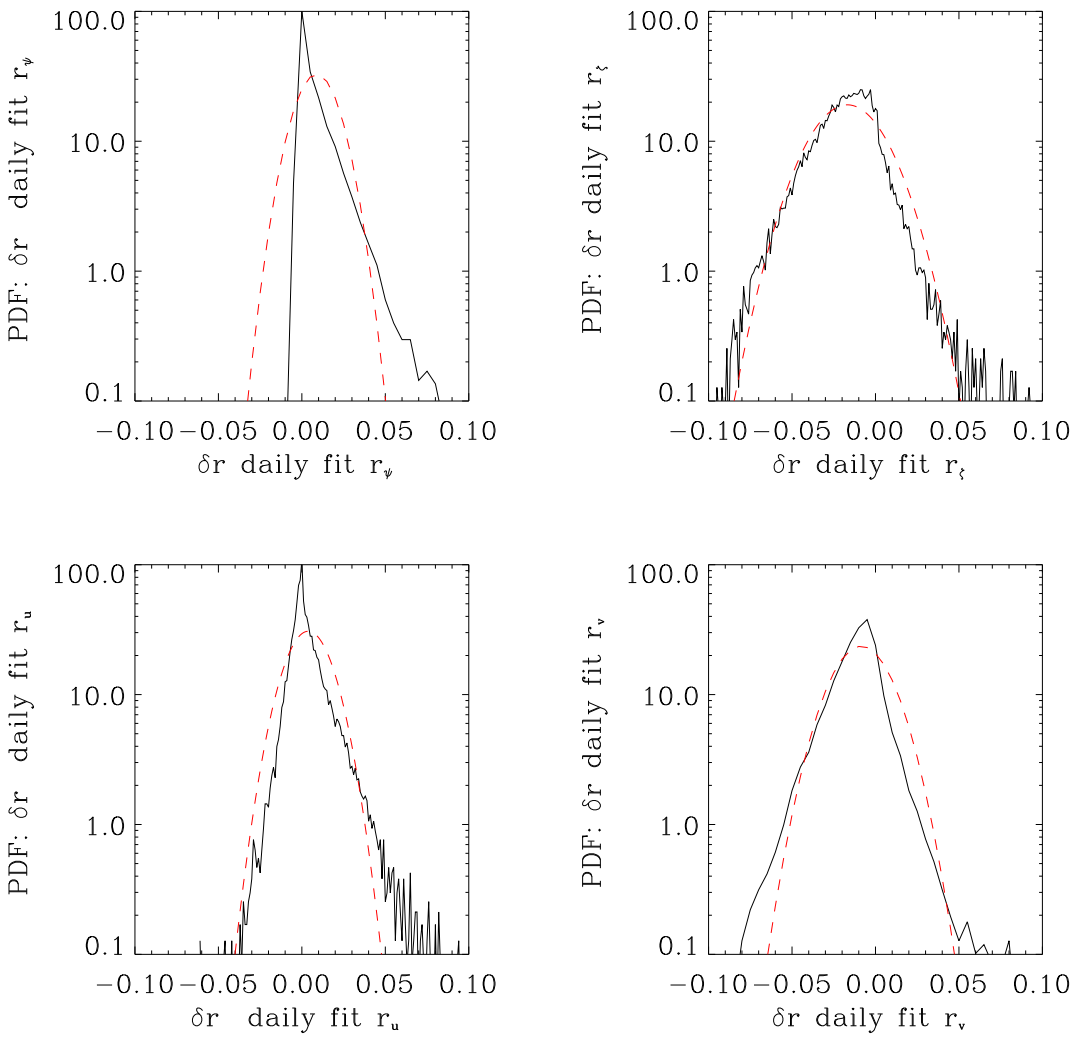

Figure 7.7: Comparison of the flow reconstructed by terms of a TF with α fit in the real domain using the eSQG approach: PDF of the difference of correlations δr with respect to eSQG, and correlations of a TF with spectral slopes fit in the real domain by maximizing correlations of (from top to bottom and left to right): Stream function, vorticity, zonal and meridional velocity components, respectively.

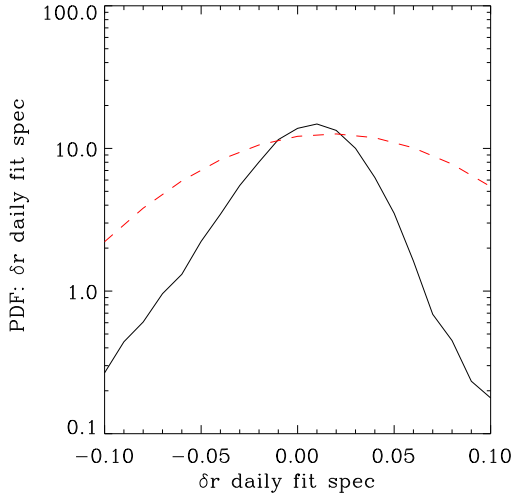

Figure 7.8: Comparison of the flow reconstructed using a TF with α estimated in the wavenumber domain with eSQG approach. PDF of the difference of correlations δr with respect to eSQG and correlations of a TF with spectral slopes estimated in the wavenumber domain.

Once more, the flow is reconstructed using a k^{α} transfer function from SST observations and, is then compared to the reference flow retrieved from altimetric observations by means of the spatial correlation coefficients. In order to compare the reconstruction of the flow by terms of the four fit spectral slopes with the eSQG approach, the difference of correlations has been computed in a similar way than to the previous chapter as:

$$\delta r = r_x - r_{eSQG}, \tag{7.8}$$

where r_{eSQG} corresponds to the correlations between the stream function retrieved from the eSQG approach and that retrieved from altimetric observations. Similarly, r_x corresponds to the correlations between the stream function retrieved from altimetric observations and that retrieved from SST observations using a TF with the spectral slopes previously fit. The x in the subindex can be substituted for ψ, u, v or ζ, indicating the variable whose correlation was maximized. According to the definition of δr a positive value indicates that the flow reconstructed by the fit transfer function improves the eSQG flow reconstruction.

To further assess the flow reconstruction from a TF with the four fit spectral slopes in the real domain, the PDF of the difference of the correlation δr was computed and is shown in Figure 7.7. The performance evaluation of the daily spectral slopes estimated in section 7.1 is again presented in this section, in order to better compare the variants flow reconstruction approaches. Figure 7.8 shows the PDF of the correlation difference for the flow reconstructed from a TF characterized by the spectral slopes estimated in the wavenumber domain. Results show that the improvement with respect to the eSQG reconstruction is not significant, since all four PDF show a mean close to zero. In the case of maximizing correlation of the stream function and the zonal velocity, the mean is positive, which indicates that the eSQG reconstruction is slightly

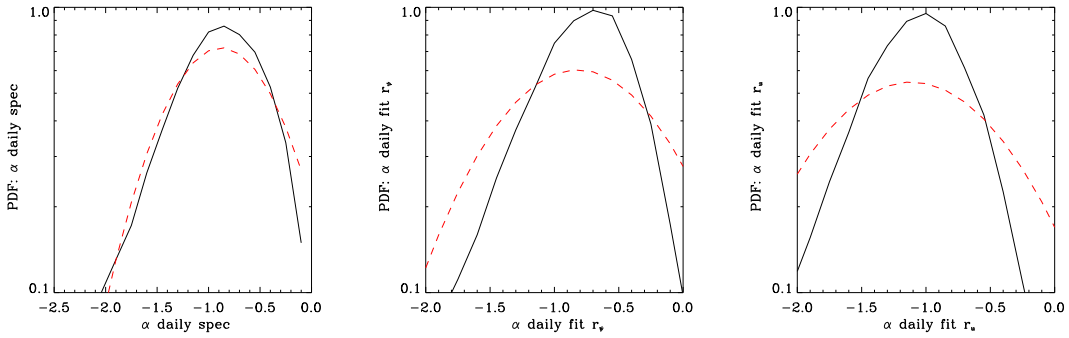

Figure 7.9: PDF of daily spectral slopes of the TF between SST and SSH From left to right: PDF spectral slope estimated in the wavenumber domain, PDF of spectral slope estimated in the real domain by maximizing correlation of stream function and PDF of spectral slope estimated in the real domain by maximizing correlation of zonal component, respectively.

improved, whereas in the case of the meridional velocity component and the vorticity this mean is negative, which indicates that the reconstruction is slightly worse than the eSQG. Furthermore, they present in general a positive skewness, which denotes an asymmetric distribution with a tail extending out towards a more positive r. This effect is more pronounced in the case of the maximization of the correlations of the stream function and the zonal component of the velocity. (see Table 7.1). For this reason, these two fit spectral slopes were selected in order to further analyse the geographical patterns of both the difference of correlation and the mean spectral slope per box.

Table 7.1: Moments of the difference of correlation δ_r: Difference of correlations δ_r as defined in equation (7.8) between eSQG and TF with spectral slopes by maximizing different variables of the flow: the stream function δr_ψ, zonal δr_u and meridional component δr_v , and vorticity δr_ζ.

	Mean	Variance	Skewness	Kurtosis
δr_ψ	8.8e-3	1.47e-4	3.49	23.85
δr_u	3.8e-3	1.7e-4	2.6	21.19
δr_v	-8.6e-3	2.8e-4	0.59	11.13
δr_ζ	-1.7e-2	4.3e-4	0.50	5.57
δr α mean spec	3e-3	1.2e-4	0.74	4.88
δr α daily spec	8.4e-3	9.9e-4	-0.47	2.06

Nevertheless, before analysing the geographical patterns of the difference of correlations and the mean spectral slope, it is interesting to get insight on the consistency between the different daily spectral slopes estimated in the spectral space and the ones estimated in the real space by maximizing the correlation of the stream function and the zonal component. To this end, the moments of the resulting daily spectral slopes were computed and are shown in Table 7.2. The mean spectral slope estimated in the real space by maximizing the stream correlation and the mean spectral slope estimated in the spectral domain are sligthly flatter than k^{-1}, whereas

the spectral slope estimated by maximizing the zonal velocity component correlations is much

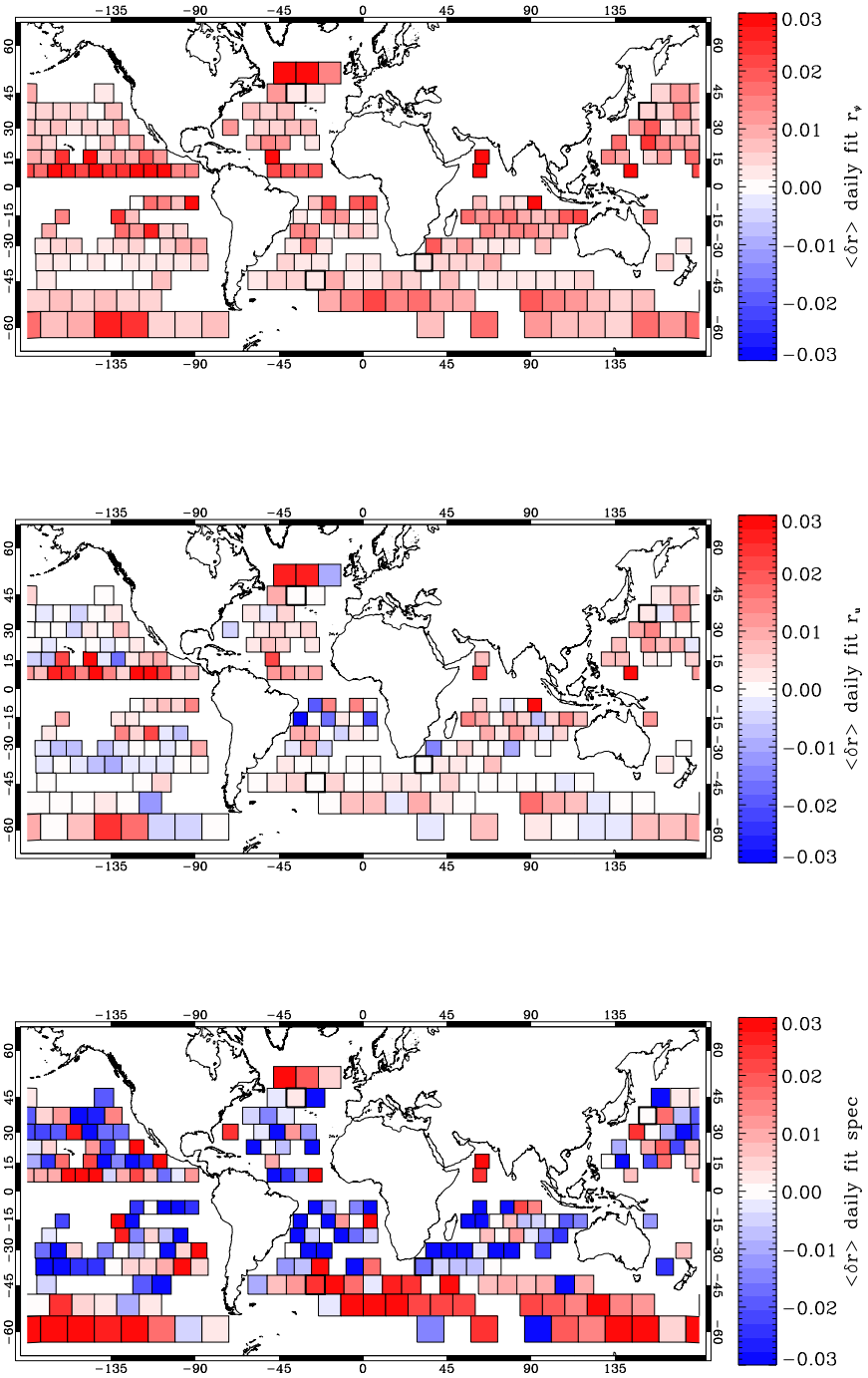

Figure 7.10: Mean difference between the k$^\alpha$ and the eSQG stream function correlations. Mean difference between the k^α stream function correlation, and the eSQG stream function correlation for: α maximizing correlation of the stream function (top), α fit maximizing correlation of zonal velocity component (middle), and α daily estimated in the wavenumber domain (bottom).

closer to k^{-1}, indeed the position of the maximum of the PDF in that case is very close to k^{-1}, as shown in Figure 7.9. However, the estimation of the spectral slope by maximizing the correlation of the zonal velocity is the least precise, with a variance of 0.53.

Table 7.2: Moments of the daily spectral slopes α. Moments of the daily spectral slopes estimated: in the space domain by maximizing the correlations of the stream function and the zonal component of the velocity, and that estimated in the spectral domain.

	Mean	Variance	Skewness	Kurtosis
$\alpha\ r_\psi$	-0.82	0.44	-2.25	10.33
$\alpha\ r_u$	-1.13	0.53	-1.98	8.73
α spec	-0.87	0.30	-0.77	1.48

Geographical analysis of the reconstructed flow

The geographical patterns of the performance of the flow reconstruction in terms of a daily TF with the spectral slope fit in the real domain, by maximizing the correlation of the stream function and the zonal velocity component, as well as the performance of a TF with spectral slope estimated in the wavenumber domain were analysed. The mean of the differences of correlation δr for every box, and for each of the three analysed methods are shown in Figure 7.10. Results confirm that in the case of the fit spectral slope by maximizing the stream function correlation, the eSQG correlation is slightly improved everywhere, even in the tropical regions. In the case of the fit spectral slope by maximizing the zonal component of the velocity field correlation, the improvement is more moderate with only a few exceptions where the reconstruction does not improve. While in the case of the flow reconstructed from daily spectral slopes estimated in the wavenumber domain the improvement is higher near the major extratropical current systems, and the performance at low latitudes is worse than in the two previous cases.

In order to facilitate their comparison with the estimated spectral slope of the mean TF computed in the last chapter, the daily spectral slopes estimated in the space and wavenumber domain were averaged. Results show that the mean spectral slope in the case of maximizing the stream function correlation is flatter than the mean of the daily spectral slope estimated in the wavenumber space and the mean spectral slope retrieved by maximizing the zonal velocity component correlation, especially in high energetic regions; while the spectral slope fit by maximizing the zonal velocity component correlation presents spectral slopes close or equal to k^{-1} near the major extratropic current systems, especially in the ACC. The mean spectral slopes fit by maximizing correlation of the stream function resemble the estimated spectral slopes of the mean transfer function shown in Figure 6.3. It is also interesting to note that in mid latitudes (30°-45°), particularly in the southern hemisphere, the mean of daily spectral slopes characterized in the wavenumber domain is closer to k^{-1} compared to the mean spectral slopes fit in the real domain. However, taking into account the standard deviation of the spectral slopes shown in Figure 7.12, the mean spectral slopes fit in the real domain seem to be slightly more precise in

energetic regions, whereas in lower energetic regions and low latitudes the mean spectral slopes estimated in the wavenumber space seem to be more precise than the fit in the real space.

Table 7.3: Velocity correlations

	eSQG		k^α spec		k^α space			
					r_ψ		r_u	
Box	u	v	u	v	u	v	u	v
GS	0.69	0.68	0.71	0.68	0.71	0.69	0.71	0.69
ACC	0.74	0.74	0.78	0.74	0.75	0.74	0.75	0.75
Agulhas	0.70	0.62	0.70	0.61	0.72	0.63	0.73	0.64
Kuroshio	0.68	0.58	0.68	0.58	0.69	0.60	0.69	0.61

To further evaluate the performance of the flow reconstruction, we focus now on the components of the velocity field. The performance of the reconstructed velocity field is analysed taking as a reference velocity field retrieved from altimetric observations using two metrics: the correlation coefficient and the RMSE. This evaluation is performed taking into account the cases in which SST and SSH are closely in phase, based on the study performed in chapter 5. Thus, once more, only days with the stream function combined correlations higher than 0.85 will be considered for computing the correlation coefficient and the RMSE with respect to velocity field retrieved from altimetric measurements. These metrics are computed for each of the three reconstructions presented throughout this chapter: (i) from the TF with daily spectral slopes estimated in the wavenumber domain (ii) from the TF with daily spectral slopes fit by maximizing the stream function correlations, and (iii) from the TF with daily spectral slopes fit by maximizing the zonal velocity component correlations. The metrics of the eSQG approach reconstruction are also computed to allow comparison. Results shown in table 7.3 and 7.4 confirm that the reconstruction from the three different daily TF show similar performance to the eSQG approach. It is worth to noting that while the performance in terms of correlations is similar for both components of the velocity, it is not so for the RMSE. A higher RMSE for the zonal component is observed for all four boxes and each of the approaches shown in table 7.4. This result can be generally observed for all boxes (see Appendix C).

Table 7.4: Velocity RMSE [cm/s]

	eSQG		k^α spec		k^α space			
					r_ψ		r_u	
Box	u	v	u	v	u	v	u	v
GS	11.34	8.95	11.23	9.07	11.33	8.98	11.27	8.94
ACC	7.38	5.23	6.86	5.33	7.37	5.28	7.34	5.24
Agulhas	18.18	15.89	18.84	16.16	18.08	15.80	17.99	15.76
Kuroshio	17.45	13.73	17.36	13.89	17.30	13.53	17.22	13.58

Finally, and as a summary, the performance of the velocity field reconstruction in terms of correlations and RMSE from all the approaches analyzed throughout this Ph.D. thesis are

summarized in tables 7.5 and 7.6 , respectively, for the four boxes selected in previous chapters. Results have evidenced that the velocity field reconstruction by the eSQG approach can be enhanced when the transfer function is built up from simultaneous observations of SST and SSH, the so-called combined approach. Furthermore, results have revealed that eSQG is not significantly improved by a transfer function that follows a k^{α} model and suggest that the SQG reconstruction is a good statistically approach to retrieve surface ocean currents when no simultaneous SST and SSH observations are available. For the shake of completeness, global results are presented in Appendix C.

Table 7.5: Velocity correlations

	combined		eSQG		k^{α} spec mean		k^{α} spec daily		k^{α} real r_{ψ}		k^{α} real r_u	
Box	u	v	u	v	u	v	u	v	u	v	u	v
GS	0.84	0.81	0.69	0.68	0.67	0.65	0.71	0.68	0.71	0.69	0.71	0.69
ACC	0.86	0.84	0.74	0.74	0.74	0.74	0.78	0.74	0.75	0.74	0.75	0.75
Agulhas	0.86	0.78	0.70	0.62	0.67	0.60	0.7	0.61	0.72	0.63	0.73	0.64
Kuroshio	0.84	0.75	0.68	0.58	0.63	0.56	0.68	0.58	0.69	0.60	0.69	0.61

Table 7.6: Velocity RMSE [cm/s]

	combined		eSQG		k^{α} spec mean		k^{α} spec daily		k^{α} real r_{ψ}		k^{α} real r_u	
Box	u	v	u	v	u	v	u	v	u	v	u	v
GS	8.68	6.99	11.34	8.95	11.48	9.15	11.23	9.07	11.33	8.98	11.27	8.94
ACC	5.63	4.13	7.38	5.23	7.40	5.31	6.86	5.33	7.37	5.28	7.34	5.24
Agulhas	13.33	12.55	18.18	15.89	18.46	16.21	18.84	16.16	18.08	15.80	17.99	15.76
Kuroshio	12.70	11.01	17.45	13.73	17.67	13.94	17.36	13.89	17.30	13.53	17.22	13.58

7.4 Summary and Conclusions

The spectral properties of the daily transfer function between SST and SSH observations were characterized following two different approaches. On the one side, the spectral slope was estimated in the wavenumber domain, and on the other, it was characterized in the real domain using two different metrics: the correlation coefficients and RMSE. Results reveal that both metrics in real space were similar in terms of the performance of flow reconstruction, even if flatter spectral slopes were found when using the RMSE metric. In general, while the daily spectral slopes may deviate from k^{-1}, the mean of the three estimated spectral slopes presents similar geographical patterns, although some slightly differences were observed, with values close to k^{-1} near energetic regions, such us the ACC. This suggests that, statistically the ocean surface dynamics follow the SQG theory in these regions. Nevertheless, the spectral slopes of the TF between SSH and SST obtained in tropical regions were steeper. Furthermore, the analysis of

the performance of the flow reconstruction revealed that the eSQG approach is not significantly improved, even by a transfer function that follows a k^{α} model, where the spectral slope is estimated daily. This outcome suggests that a k^{α} model is inadequate to fully describe the optimal TF between SST and SSH which would enhance the eSQG reconstruction of the flow, as seen in chapter 5.

One potential explanation why the k^{α} model transfer function may not fully describe the optimal TF is the phase shift between SST and SSH. In fact, previous studies based on numerical simulations have revealed that the phase shift between SST and SSH is minimal for deep Mixed Layers (ML) (Isern-Fontanet *et al.* , 2008, 2014). Another study conducted by Hausmann & Czaja (2012), focusing on the SST/SSH relationship following eddy tracks, found that the eddy SST signature is characterized by a Westward phase shift of SST anomaly with respect to rotating eddy cores. This phase shift is more pronounced for eddies originating in quiescent regions of the subtropical gyres, but is also clearly established for more energetic regions, such as the GS and ACC regions. The study of phase shift presented in section 7.1 reveals smaller phase shifts for wavelength larger than 200 km. The larger phase shift observed for smaller scales could be due to the fact that altimetric maps cannot resolved well smaller scales. Indeed, Ducet *et al.* (2000) compared the SSH wavenumber spectrum from the merged altimetric maps to that from the along-track data, which was considered to represent the intrinsic resolution of altimeter data, and estimated the resolution of the merged data to be about 150 km in wavelength. This clearly suggests that further work should be carried out using along-track data in order to validate the proposed approach to reconstruct ocean surface current presented in this Ph.D. thesis, and indicates that futher investigation is needed to determine whether the performance of the characterized transfer function could be improved. In this regard, such a study is already being planned to be conducted, using Infrared SST and along-track altimeter (Envisat, Sentinels 3), in the framework of a postdoctoral fellowship research project (OCEANUS) funded by ESA Living Planet Fellowship.

Finally, the analysis of the performance of the reconstruction from all the daily estimated TF revealed a systematic difference between both components of the velocity fields. The zonal component showed lower performance in terms of RMSE, while the difference between both components was not appreciated when computing the correlation coefficients (see tables 7.3 and 7.4). It is worth recalling that the proposed model of the TF requires that two different terms be estimated. On the one side the spectral slope and, on the other, a constant that sets the energy level and is estimated unsing altimetric observations. This constant may have no effect on the retrieval of velocity components, considering that the derivative operator is applied to retrieve the velocity field from the stream function (see equation 7.5 and 7.6). Thus, this difference could be due to the estimation of the spectral slope and related to the fact that the mesoscale and large scale might not be well separated. Furthermore, there may be is a North-South gradient still present in the SST field and, this variation in the North-South direction potentially specifically affecting the retrieval of the zonal component of the velocity. The outcome also suggests that the spectral slope might not be unique for each of the directions, which could necessitate estimating one spectral slope in each x-y direction.

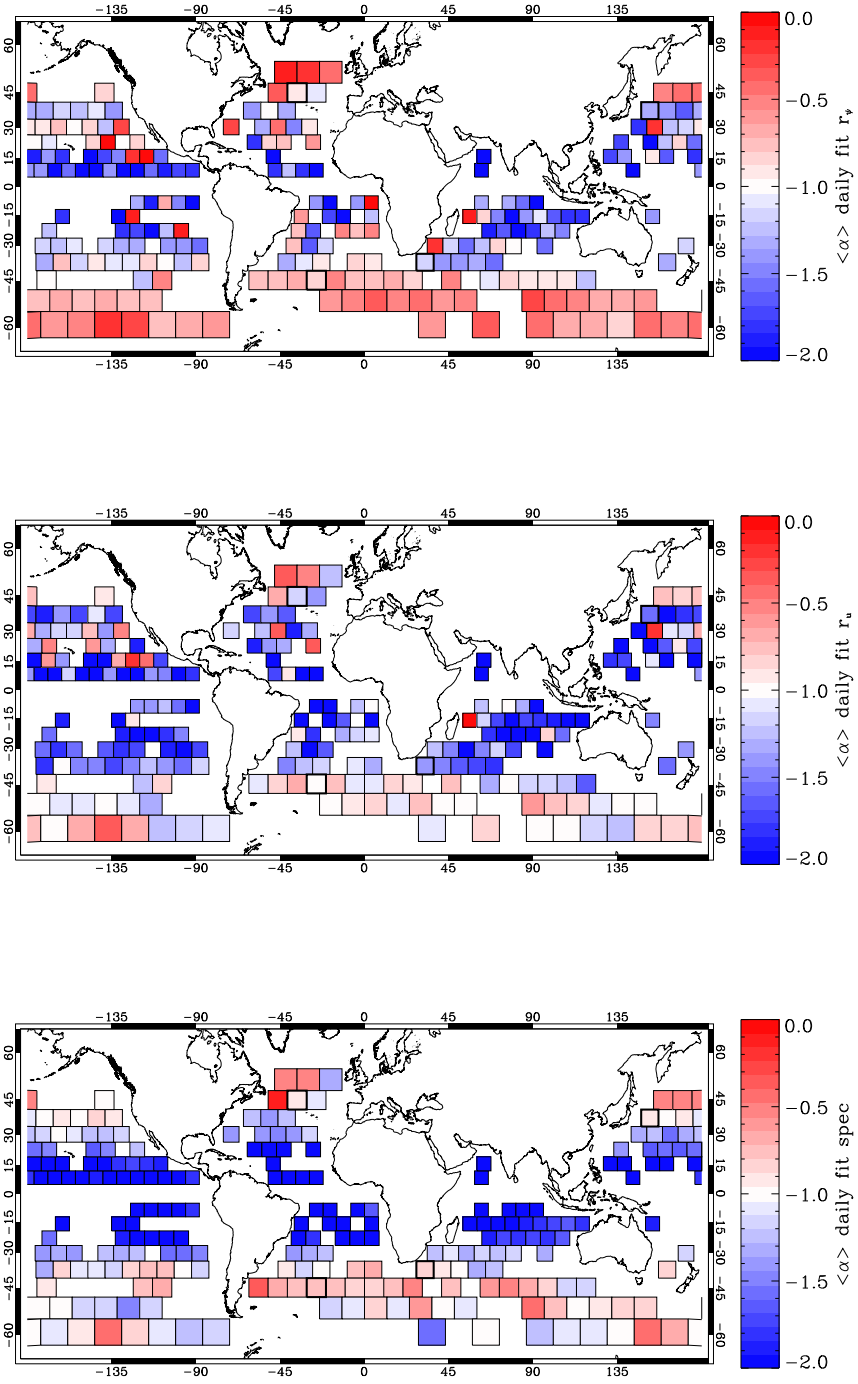

Figure 7.11: Mean of the daily spectral slope. Top: Mean of spectral slope fit in the real domain by maximizing the correlation of the stream function. Middle: Mean of spectral slope fit in the real domain by maximizing the correlation of zonal velocity component. Bottom: Mean of spectral slope estimated in the wavenumber domain

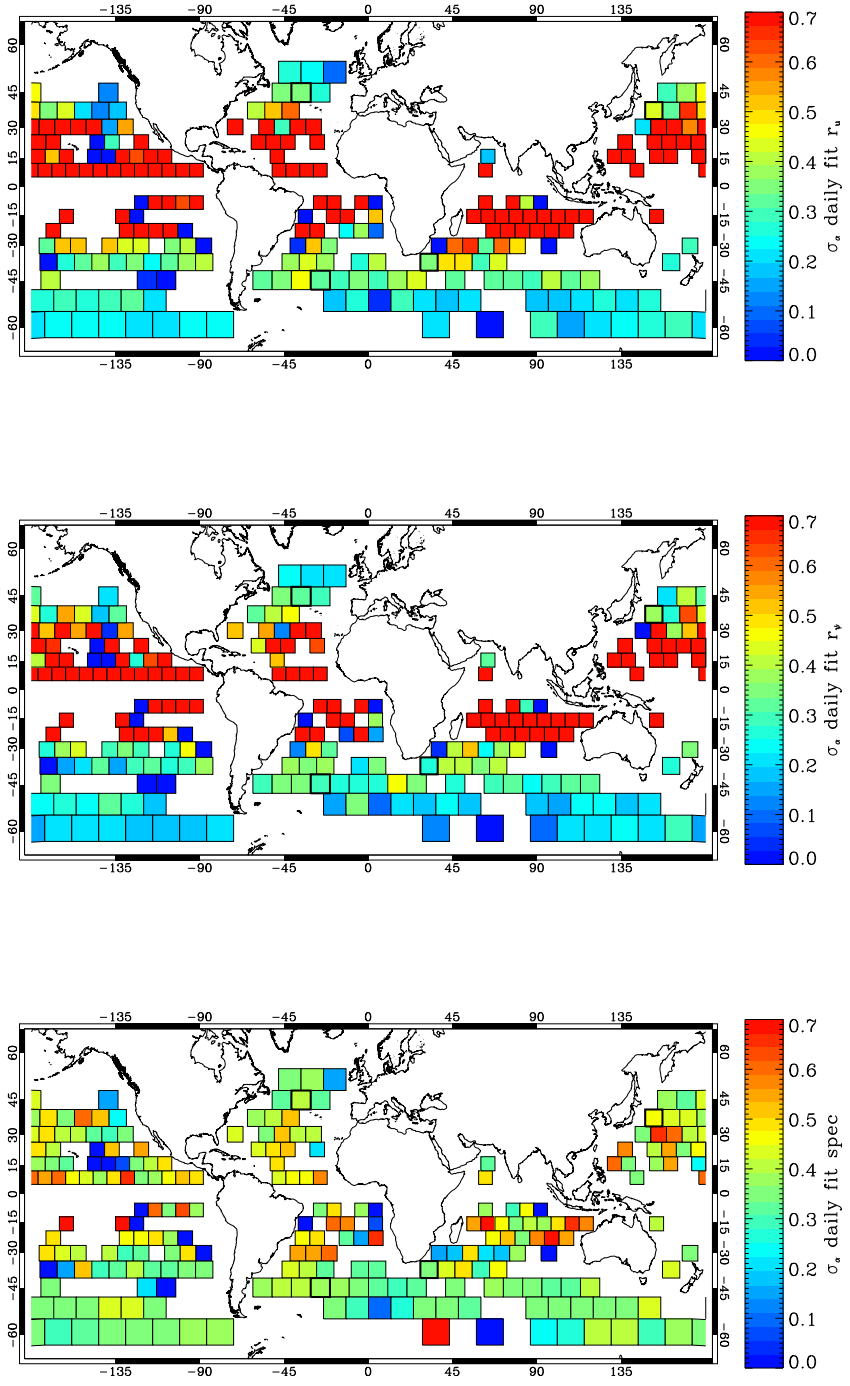

Figure 7.12: Standard deviation of the daily spectral slope. Top: Standard deviation of spectral slope fit in the real domain by maximizing the correlation of the stream function. Middle: Standard deviation of spectral slope fit in the real domain by maximizing the correlation of zonal velocity component. Bottom: Standard deviation of spectral slope estimated in the wavenumber domain.

Chapter 8

Conclusions and Perspectives

This Ph.D. thesis has assessed the capability of SST microwave radiometers observations to retrieve ocean surface currents. Two different approaches were analyzed at a global scale: on one side, the analysis of the validity of the SQG approach has been performed, and on the other, an approach based on the spectral properties between simultaneous SST and SSH observations has been analyzed. Both approaches have been compared with ocean surface currents retrieved from merged altimetric observations. The study has been focused on the period from October 2002 to May 2005, since during that period there were available four different altimeters, and the quality of the merged altimetric observations was enhanced.

8.1 Main conclusions

The reconstruction of the ocean surface currents from SST observations can be expressed in terms of a transfer function notation, that allows to convert SST maps into SSH, and thus, into currents. This transfer function can be theoretically derived using the SQG equations, assuming that the variability of density anomaly is dominated by the SST anomaly. The analysis of the validity of SQG at a global scale performed in Chapter 5 revealed that this dynamical model is valid near the major extratropic current system such us the Gulf Stream, the Antartic Circumpolar Current, Kuroshio currents. Besides, the potential of MW SST observations to reconstruct ocean surface currents was analyzed using a synergetic approach: the combination of the SST phase with the SSH spectra. Actually, we explored under which environmental conditions the phase of the MW SST is close to the SSH phase. Results presented in Chapter 5 showed that the phase of the MW SST can be used to retrieve ocean currents during winter, near the major extratropical current systems, which are characterized by an intense mesoscale activity and the presence of strong thermal gradients, and deep ML. Furthermore, the reconstruction of the velocity fields from an ideal transfer function built up from simultaneous SST and SSH observations revealed that the SQG approach can be enhanced.

With the idea to better characterize the transfer function, we studied the spectral properties of an empirical transfer function derived from simultaneous SST and SSH observations. As a first attempt, the spectral properties of a mean transfer function were characterized at a global

scale in Chapter 6. Results revealed a flatter response than the k^{-1} predicted by SQG theory near the major extratropical current systems, when the spectral slope was estimated in the wavelength range between 100-400 km. Nevertheless, the spectral slope was closer to k^{-1} in high energetic regions when restricting the analysis to short wavelengths (100-250 km). The flow was then reconstructed using a transfer function that followed a k^{α} model, with α being the estimated spectral slope of the mean transfer function. However, the evaluation of the performance revealed that the reconstruction considering the estimated spectral slope of the mean transfer function did not significantly improve the SQG reconstruction.

The temporal variability of the transfer function was further analyzed in Chapter 7. Contrary to the approach previously used, we adjusted the spectral slope in the real domain by using two different metrics: (i) by maximizing the correlation between the flow reconstructed from SST by the transfer function and the flow retrieved from SSH altimetric observations, and (ii) by minimizing the RMSE between both flows. Despite the daily spectral slopes may deviate from k^{-1}, the mean of the three estimated spectral slopes presented similar geographical patterns, with values approximately k^{-1} near energetic regions, such us the ACC. The above analysis revealed that at short scales the SQG approach is a reasonable good approach, at least, from a statistical point of view.

8.2 Key challenges and open issues

The research work presented in this Ph.D. thesis exploits the synergy of SST and SSH observations to retrieve ocean surface currents. However, it is worth highlighting that despite this work is centered on the period when four altimeters were available, and thus, the quality of altimetric maps is enhanced, they still may contain structures that are not present in microwave SST images, due to the performed interpolation, instrument noise or other corrections applied in the process of their generation. This reinforces the need of a validation using along-track altimeter data and *in-situ* data, which has only been explored in this Ph.D. thesis. In fact, on April 15, 2014, a new version of the SSALTO/Duacs products distributed by Aviso, so-called DUACS 2014, was released with several significant upgrades[1]. These changes contribute to improve the product quality as already unveiled by a recent work (Capet *et al.* , 2014) that investigated to which extent the new version of DUACS 2014 sea level anomaly product affects the description of mesoscale activity in the Eastern Boundary Upwelling Systems (EBUS). They found that DUACS 2014 product returns significantly higher eddy kinetic energy levels (+80%) within a 300 km coastal band, where mesoscale structures are known to induce important lateral physhical and biogeochemical fluxes. In addition, an automatic eddy detection algorithm detected more eddies in the EBUS (+37%), and lower eddy radius estimates, when DUACS 2014 products where applied in comparison with the former altimetry product, which was the one used troughout this Ph.D. thesis. Thus, appart from the validation using along-track altimery obser-

[1]Further information is provided in `http://www.aviso.altimetry.fr/en/data/product-information/updates-and-reprocessing/ssaltoduacs-product-changes-and-updates.html` Last visit: April 14, 2015, and Handbook (2014b)

vations, it would also be interesting to evaluate the performance of the new available DUACS 2014 product.

In addition, despite Microwave observations are suitable for global studies, their spatial resolution barely reach the 60-40 km, scales for which most of the ocean kinetic energy and its dissipation take place. The knowledge of these processes is critical for understanding global climate change. In that sense, the approach to reconstruct ocean surface currents presented in this Ph.D. thesis could be applied to higher spatial resolution SST images captured by infrared radiometers allowing to study small-scale processes and features. Envisat has provided, from 2002 to 2012, simultaneous SST infrared and altimetry observations that could be used to further investigate ocean surface currents retrieval approach presented and analyzed throughout this Ph.D. thesis. In addition, the new operational mission Sentinels 3 of ESA will ensure the continuity of simultaneous IR SST and high resolution altimeter observations that ensures the possibility of retrieving high resolution velocity fields by exploring and exploiting the synergy of both observations as shown in this Thesis. This is the main aim of OCEANUS, a research project funded by ESA Planet Fellowship that will allow to further investigate the research line opened by the work presented on this Ph.D. thesis. Furthermore, the impact of the spatial resolution and the radiometric accuracy of the MW sensors in the reconstruction of ocean surface currents proposed in this Ph.D. thesis should be investigated.

On the other hand, the proposed methodology has several advantages. Ocean surface currents are obtained by combining a single image of SST and SSH, and it has the same resolution as the original field. Despite microwave SST measurements have low resolution when compared to IR SST measurements, as mentioned above, the main advantage of using microwave sensors is their capability to measure through clouds. This property makes microwave sensors specially suited for global studies. Despite the AMSR-E halted its operation in October 4, 2011 when the instrument stopped rotating, the continuity of MW SST measurements are ensured. AMSR2 the single payload of the Global Change Observation Mission 1st - Water "SHIZUKU" (or GCOM-W1) (Imaoka *et al.* , 2010) was launched in May 18, 2012 and continues AMSR-E observations of water vapor, cloud liquid water, precipitation, SST, sea surface wind speed, sea ice concentration, snow depth, and soil moisture. The basic concept of AMSR2 is almost identical to that of AMSR-E with some important improvements. Major changes from AMSR-E include the larger main reflector with 2.0 m diameter, and the addition of 7.3 GHz channels for radio frequency interference (RFI) mitigation. Since AMSR2 and AMSR-E do not have overlapping operations periods, the intercalibration of AMSR2 with AMSR-E was performed statiscally with L1b brightness temperature observed in 2011. The comparison (Okuyama & Imaoka, 2015) revealed that AMSR2 exhibits a positive calibration difference up to 5 K compared to AMSR-E. This calibration difference appears to depend on the brightness temperature of the observed object.

In addition, it is interesting to note that the evaluation of the performance of the flow reconstruction in terms of correlations was performed considering entire images. However, results presented in Chapter 5 and in previous works (Isern-Fontanet *et al.* , 2006) showed that the thermal gradients played a role in the capability to reconstruct the flow. Thus, the performance

of the flow reconstruction might improve if only strong thermal gradients were considered. In fact, a recent work (Autret, 2014) focused on the analysis of SST fields observations from multi-sources satellite found out that lower resolution SST field provided by AMSR-E radiometer can be seen as a low pass filtered version of higher resolution SST field provided by MODIS infrared radiometer, with cut off wavelenght at 200 or 250 km approximately. This outcome has evidently an effect in the capability to detect thermal gradients, strong thermal gradients present in SST MODIS images are still present in AMSR-E SST images, although smoother, whereas weaker thermal gradients completely disappear.

The SQG approach implicitly assume that the surface density and the interior potential vorticity (PV) are correlated. In this case, SSH would resemble the surface density. In addition, due to the lack of Sea Surface Salinity (SSS) observations within the period under study, in this Ph.D thesis is assumed that the SST is the major contribution to density anomaly. Results presented in chapter 5 showed that this assumption may be valid in winter, near the major extratropic current systems. However, in presence of strong horizontal gradients of salinity, surface density may not always be dominated by temperature. Thus, furher work should be carried out to further assess the impact of using SSS in combination with SST to reconstruct ocean surface velocities. This assesment could be addressed, first, theoretically, and then using remote sensing observations of SSS. Indeed, the SMOS and the Aquarius missions provide a first opportunity to estimate the synoptic surface density fields on mesoscales in combination with MW SST observations, e.g. from AMSR2.

Finally, the ocean community is making a lot of efforts to monitor small features of ocean surface and currently there are planned space-borne missions, such as NASA/CNES SWOT and ESA's Wavemill based missions, that will provide high-spatial resolution, global measurements of ocean surface topography and ocean currents, respectively. However, these missions will begin to monitor the ocean surface in 2020, at the earliest, when the SWOT mission is planned to be launched. In the meantime, the approach presented in this Ph.D. thesis opens a door to the development of a methodology to reconstruct ocean surface currents based on mature technologies that could be applied to existent observations of SST and along-track SSH. Indeed, SST and SSH are two of the essential climate variables that have been monitored from space for over three decades and thus, constitute an interesting data set for climate change studies.

8.3 Future lines and perspectives

The work presented in this Ph.D. thesis evidenced the capability of SST MW observations to retrieve ocean surface currents, and the synergetic properties between SST and SSH observations. Nevertheless, as it was mentioned in section 8.2 there are still some key challenges and open issues that open future research lines.

Results presented in Chapter 5 points to the potential developement of a new method of reconstructing ocean currents based on the combination of the phase of SST images with the energy spectrum derived from algong-track altimetric measurements. The methodology presented in this Ph.D. thesis could also be applied to retrieve higher spatial resolution velocity fields,

when applying to IR SST images. In that sense, Envisat and the future Sentinels 3 missions offer a great oportunity to evaluate the proposed approach, since simultaneous SST and altimetric observations are provided. From a dynamic point of view, it would allow to study sub-mesoscale motions, which play essential role in upper-ocean vertical exchange processes.

On the other side, MW radiometers observations are suitable for global studies, although their spatial resolution is lower when compared with observations from IR radiometers. Results presented in Chapter 5 unveiled that SST gradients play a role in the capability of SST MW observations to reconstruct ocean surface currents. Thus, it would be interesting to study the impact of the spatial resolution and the radiometric accuracy of the MW sensors in the reconstruction of ocean surface currents following the approach analyzed in this Ph.D thesis.

The retrieval from SST observations using the SQG approach assumes that the suface density variability is dominated by the SST anomaly. However, this may be a strong assumption in the presence of strong horizontal gradients of SSS. Currently, the SMOS and Aquarius missions provide remote sensing observations of SSS, that together with SST observations, e.g. from AMSR2, could be used to estimate synoptic suface density fields, and to further assess the impact of using SSS in combination with SST to reconstruct ocean currents.

Finally, although the improvements of the velocity field reconstruction by the characterized transfer function were marginal, when compared to SQG approach, the study conducted in Chapters 6 and 7 showed new possibilities for improvement. First, further work should be carried on to the spectral characterization of the transfer function, e.g. the transfer function in some regions unveiled two different spectral slopes in the studied wavelength range. Thus, other transfer function models should be considered and studied. Furthermore, the analysis of the performance of the reconstruction from the daily estimated TF, presented in chapter 7, revealed a systematic difference between both components of the velocity fields. This outcome suggests that the spectral slope might not be unique for each of the directions, which needs to be considered for further investigation.

8.4 Original contributions

The original contributions of this Thesis are listed below:

- The analysis of the validity of eSQG flow reconstruction at a global scale using remote sensing observations from Microwave Radiometers.
- Analysis of the performance of a new approach to improve the estimation of surface currents from satellite observations through the combination of simultaneous SST and SSH measurements.
- Analysis of the spectral properties of the transfer function between SST and SSH observations at a global scale.
- Characterization of the parameters that define the transfer function between SST and SSH observations in order to adjust the reconstructed flow to the one retrieved from altimetric

observations.

8.5 Publications arising from this Thesis

A complete list of publications in peer-reviewed journals, conference proceedings, and workshops arising from this research is provided in Appendix D. Chapter 5 to 7 of this document are mainly based on the following publications:

Chapter 5

González-Haro, C., and J. Isern-Fontanet (2014), Global ocean current reconstruction from altimetric and microwave SST measurements, J. Geophys. Res. Oceans, 119, 3378−3391, doi:10.1002/2013JC009728.

Chapters 6 and 7

González-Haro, C., and J. Isern-Fontanet (2015), Spectral analysis of the transfer function between SST and SSH at a global scales , J. Geophys. Res. Oceans, In prep.

Appendix A

Comparison of the flow reconstruction with in-situ data

Both reconstruction methods, eSQG and the combined approach, were validated with ADCP data. Since the available ADCP data within the period under study are sparse comparing with the geographical coverage of the study, only one case study was found to be illustrative and is hereafter presented. It corresponds to a box allocated in the south hemisphere, specifically, latitude ranging between $-33,78°$ and $-40,97°$ and longitude between $46,15°$ and $55,38°$.

For comparison, the surface velocity field retrieved from the three different methods were interpolated along the track of ship. Figure A.1 shows the SSH satellite 2D field for the same day of the ADCP data (3 August, 2004) and the surface velocity field measured from ADCP data is also shown (left). From the dynamical point of view, this study case is interesting for comparition because of the presence of the eddy that is crossed by the transect of the ship. The three different retrievals from remote sensing data seem to properly detect the eddy. This result is confirmed by the scatter plot of both components of the velocity field (see Figure A.2).

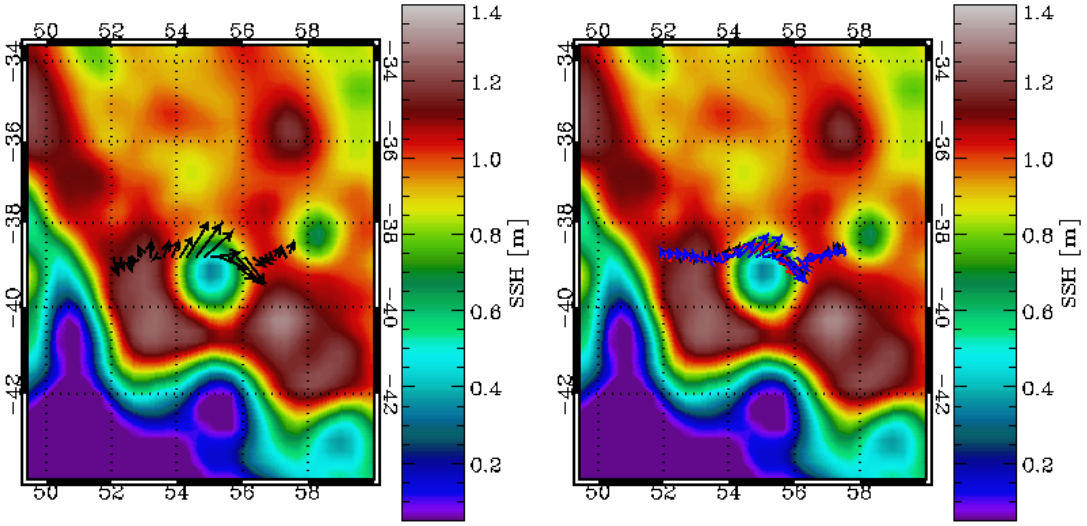

Figure A.1: SSH and ADCP velocity. Absolute dynamic height field corresponding to the date of the cruise (3 August, 2004). Left: ADCP surface velocity field. Right: Surface velocity field retrieved by: altimeter (black), eSQG (blue) and combined approach (red). All fields were interpolated along the transect of the cruise.

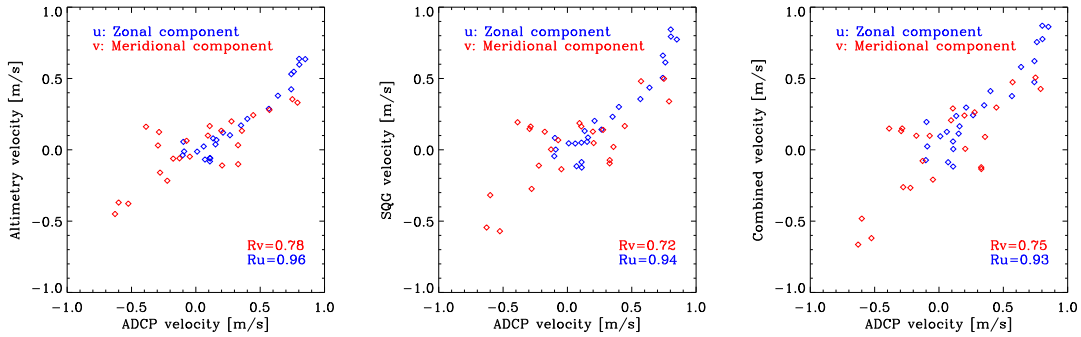

Figure A.2: Velocity comparison with ADCP data. From left to right: Scatter plot of velocity components measured from ADCP and velocity components retrieved from: altimetry (left), eSQG (middle), combined approach (right). Blue points correspond to zonal component and red points to meridional component.

Appendix B

Estimation of the spectral slope standard error

The spectral slope of the mean transfer function was computed for each of the defined boxes. For each box, daily transfer function spectra for those days with high correlations were averaged.

A linear equation was fitted to each averaged spectrum using a least squares method as follows:

$$y = \beta + \alpha x, \tag{B.1}$$

where $y = \log_{10} \overline{F}_T$ and $x = \log_{10} k$; $\overline{F}_T$ is the spectra of the mean transfer function at wavenumber k. The uncertainty of the mean transfer function, denoted as $(\sigma_{\overline{F}_T})$, is computed as the standard deviation of all the averaged spectra at wavenumber k.

Before attempting to compute the standard error of the spectral slope α , propagation of errors should be considered (Barlow, 1989). The variance ${\sigma_f}^2$ in the value of any function $f(x)$ is:

$${\sigma_f}^2 = {\sigma_x}^2 \left(\frac{\partial f}{\partial x_i} \right)^2. \tag{B.2}$$

In that case, the function is $f(x) = \log_{10} x$ and $\sigma_x = \sigma_{\overline{F}_T}$. Thus, the uncertainty that have to be taken into account when computing the standard error of the spectral slope is:

$$\sigma_f = \sigma_{\overline{F}_T} \frac{1}{\ln 10} \frac{1}{\overline{F}_T}. \tag{B.3}$$

Finally, the standard error in the spectral error can be computed as stated in section 15.2 of Press *et al.* (2007) , and using their same notation, as:

$$\sigma_\alpha = \sqrt{S/\Delta} \tag{B.4}$$

where S and Δ are given by:

$$S = \sum_{i=1}^{N} \frac{1}{{\sigma_{f_i}}^2}, \tag{B.5}$$

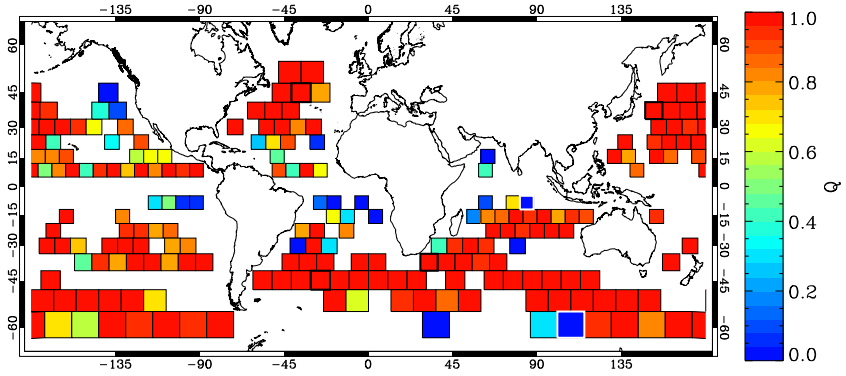

Figure B.1: The goodness-of-fit: Q probability. The probabilty Q that a value of chi-square as poor as the chi-square merit function should occur by chance . Wider black lines corresponds to selected boxes GS, ACC, Agulhas and Kuroshio (see table 6.1), white lines delimit boxes for which Q probability is lower than 0.001, and then the goodness-of-fit is poor.

$$\Delta \equiv SS_{xx} - (S_x)^2, \tag{B.6}$$

where N is given by the number of data points in the wavenumber range corresponding to wavelengths between 400 and 100 km, typically about 12 when boxes of 800 km are considered and 23 points for 1600 km boxes ; S_{xx} and S_x are computed as:

$$S_{xx} \equiv \sum_{i=1}^{N} \frac{{x_i}^2}{{\sigma_{f_i}}^2} \tag{B.7}$$

and,

$$S_x \equiv \sum_{i=1}^{N} \frac{x_i}{{\sigma_{f_i}}^2} \tag{B.8}$$

Following recommendations and the steps described in section 15.2 of Press *et al.* (2007), we are *still* not done. We must estimate the goodness-of-fit of the data to the model. Absent this estimate, we have not the slightest indication that the parameters have any meaning at all. The probabilty Q that a value of chi-square as poor as the chi-square merit function should occur by chance was computed by terms of the incomplete gamma function. If Q is larger than 0.1, then the goodness-of-fit is believable. It it is larger than 0.001, then the fit *may* acceptable if the errors are non normal or have been moderately underestimated. If Q is less than 0.001 then the model and/or estimation procedure can rightly be called into question.

Figure B.1 shows the probabilty Q for each box and evidences that the goodness-of-fit is believable for most of boxes with the execption of two boxes that are delimeted by white lines in Figure B.1.

Appendix C

Performance of velocity field reconstruction

The performance of the reconstructed velocity field is analysed taking as a reference velocity field retrieved from altimetric observations using two metrics: the correlation coefficient and the RMSE. This evaluation is performed taking into account the cases in which SST and SSH are closely in phase, based on the study performed in chapter 5. Thus, once more, only days with the stream function combined correlations higher than 0.85 will be considered for computing the correlation coefficient and the RMSE with respect to velocity field retrieved from altimetric measurements. These metrics are computed for each of the reconstructions presented throghout this Ph.D. thesis: (i) the combined approach that takes into account an ideal TF computed from simultaneous observations of SST and SSH, (ii) the eSQG aproach , (iii) the characterized mean transfer function between SST and SSH obserations, (iv) the characterized daily transfer fuction in the spectral space, (v) the characterized daily transfer function in real space by maximizing the stream function correlation and finally (vi) the characterized daily transfer function in real space by maximizing the zonal velocity correlation.

The correlation and RMSE for the zonal components are shown in Figures C.1 and C.3 , respectively and for the meridional component in Figures C.2 and C.4, respectively.

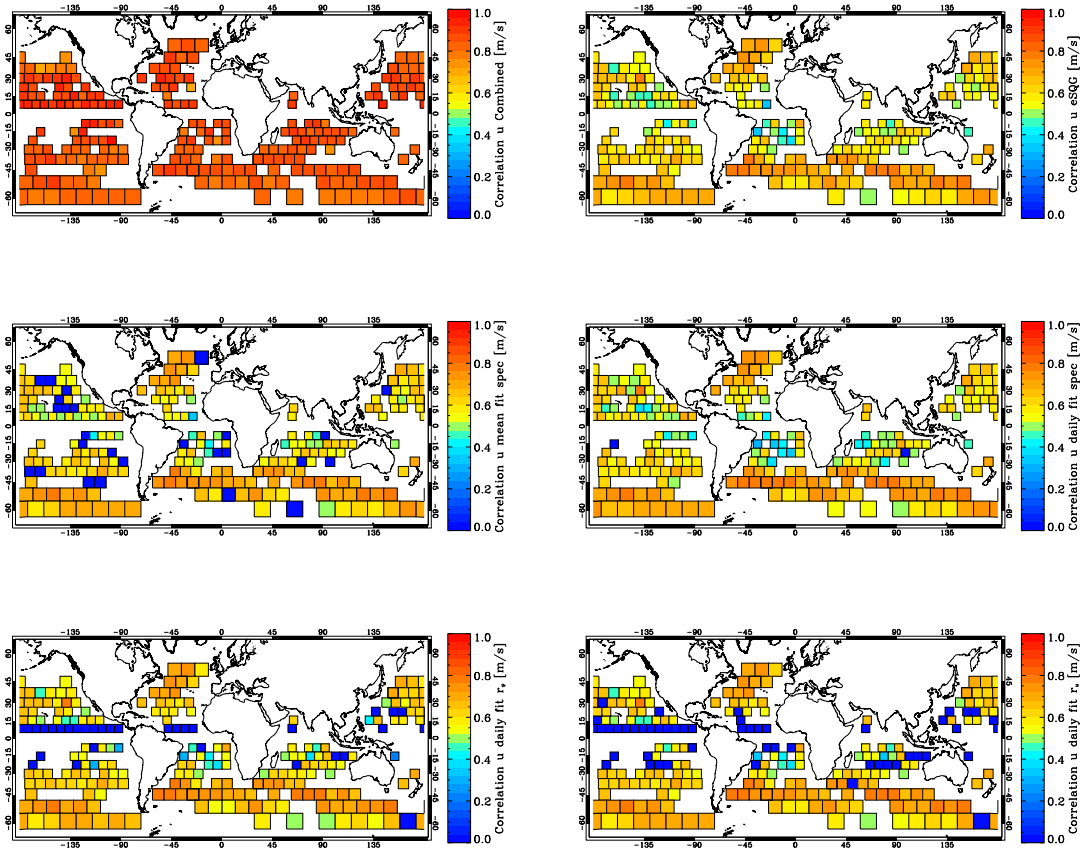

Figure C.1: Zonal velocity correlation. Correlations between zonal velocity component retrieved from altimetric observations and from (from top to bottom and left to right): the Combined approach, the eSQG reconstruction, the mean TF, the daily TF with α estmated in the wavenumber space, the daily TF with α estimated in the real space by maximizing the stream function correlation, and the daily TF with α estimated in the real space by maximizing the zonal velocity component.

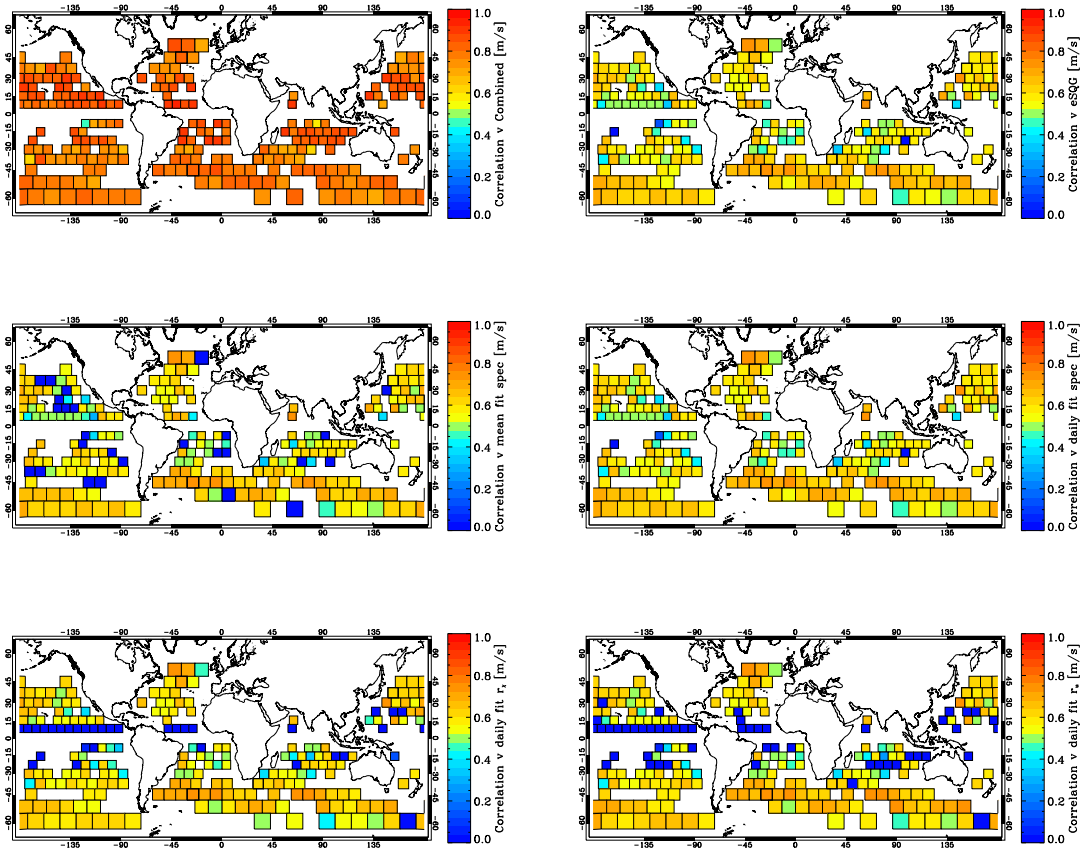

Figure C.2: Meridional velocity correlation. Correlations between meridional velocity component retrieved from altimetric observations and from (from top to bottom and left to right): the Combined approach, the eSQG reconstruction, the mean TF, the daily TF with α estmated in the wavenumber space, the daily TF with α estimated in the real space by maximizing the stream function correlation, and the daily TF with α estimated in the real space by maximizing the zonal velocity component.

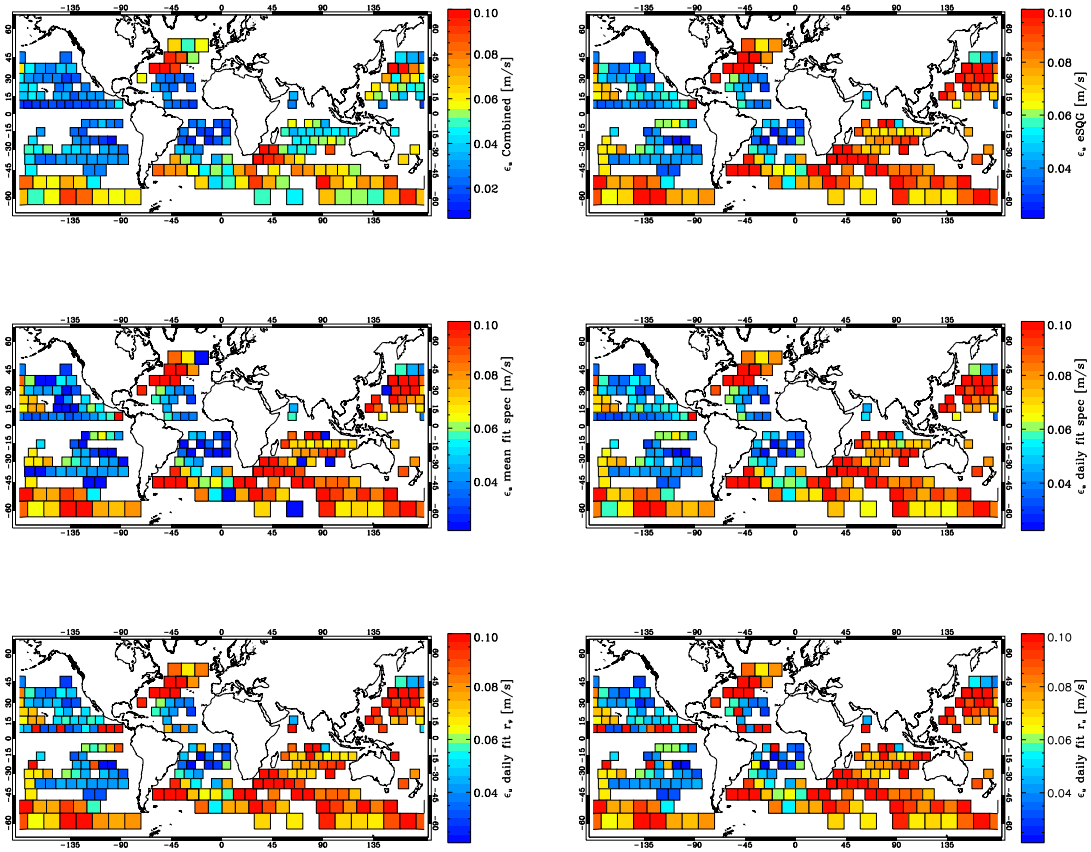

Figure C.3: Zonal velocity RMSE. RMSE between zonal velocity component retrieved from altimetric observations and from (from top to bottom and left to right): the Combined approach, the eSQG reconstruction, the mean TF, the daily TF with α estmated in the wavenumber space, the daily TF with α estimated in the real space by maximizing the stream function correlation, and the daily TF with α estimated in the real space by maximizing the zonal velocity component.

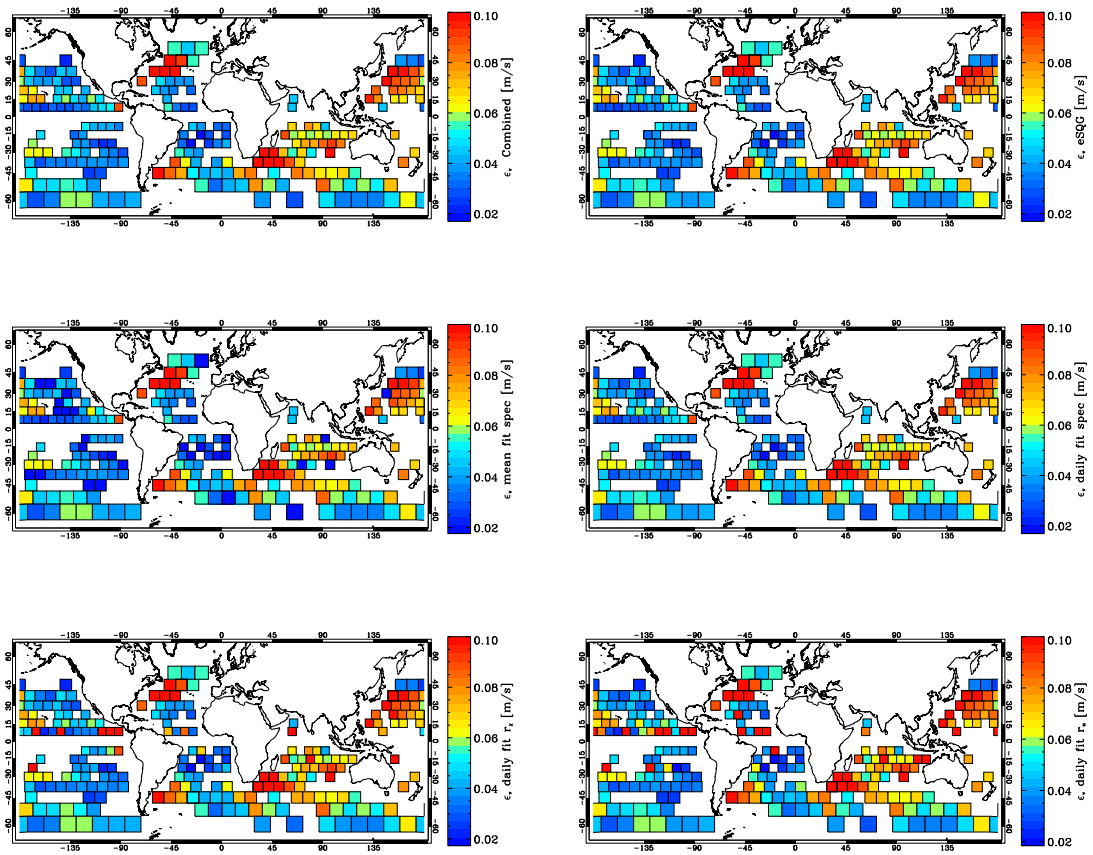

Figure C.4: Meridional velocity RMSE. RMSE between meridional velocity component retrieved from altimetric observations and from (from top to bottom and left to right): the Combined approach, the eSQG reconstruction, the mean TF, the daily TF with α estmated in the wavenumber space, the daily TF with α estimated in the real space by maximizing the stream function correlation, and the daily TF with α estimated in the real space by maximizing the zonal velocity component.

Appendix D

List of publications

Peer-reviewed journals

1. **González-Haro, C.**, and J. Isern-Fontanet (2015), Spectral analysis of the transfer function between SST and SSH at a global scales , J. Geophys. Res. Oceans, In prep.

2. **González-Haro, C.**, and J. Isern-Fontanet (2014), Global ocean current reconstruction from altimetric and microwave SST measurements, J. Geophys. Res. Oceans, 119, 3378−3391, doi:10.1002/2013JC009728.

3. Isern-Fontanet, J., Shinde, M. and **González-Haro, C.** (2014), On the transfer function between surface fields and the geostrophic stream a function in the Mediterranean Sea, J. Pys. Oceanogr., 44, 1406−1423, doi:10.1175/JPO-D-13-0186.1.

Conference proceedings

1. **González-Haro, C.**, Isern-Fontanet, J., Assessment of ocean surface currents reconstruction at a global scale from the synergy between microwave and altimetric measurements, Proc. IEEE International Geoscience and Remote Sensing Sympossium IGARSS, Pag. 2950−2953, Melbourne, Australia, July 2013. doi=10.1109/IGARSS.2013.6723444

2. **González-Haro, C.**, Isern-Fontanet, J., Ocean Surface Reconstruction at a global scale from microwave measurements. Proc. IEEE International Geoscience and Remote Sensing Sympossium IGARSS, Pag.3780−3783, Munich, Germany, July 2012, doi: 10.1109/IGARSS.2012.6350494

Conferences and Workshops

1. **González-Haro, C.**, Isern-Fontanet, J., (2013), Ocean surface reconstruction at a global scale from the synergy between microwave and altimeter measurements. ESA Living Planet Symposium. Edinburgh 9-13 Septiembre 2013.- Oral presentation

2. Isern-Fontanet, J.,Martin-Puig, C. and **González-Haro, C.** (2013), Reconstruction of Ocean velocities from the synergy between SST and SSH from SARM measurements.

ESA Living Planet Symposium. Edinburgh 9-13 Septiembre 2013.- Oral presentation

3. Martin-Puig, C., Isern-Fontanet, J. and **González-Haro, C.** (2013) (2013), Estimation of Surface Geostrophic Currents from SAR Altimetry. ESA Living Planet Symposium. Edinburgh 9-13 Septiembre 2013. - Poster

4. **González-Haro, C.**, Isern-Fontanet, J., (2013), Ocean surface currents reconstruction at a global scale from SST microwave measurements. EGU General Assembly 2013. Viena. 7-12 Abril 2013. - Oral presentation

5. Isern-Fontanet, J., Shinde, M. and **González-Haro, C.** High resolution surface circulation of the Mediterranean sea from the synergy between SSH and SST satellite observations EGU General Assembly 2013. Viena. 7-12 Abril 2013. - Poster

6. **González-Haro, C.**, Isern-Fontanet, J., (2012), Ocean surface currents reconstruction at a global scale from microwave measurements. II Encuentro Oceanografía Física Española. Madrid, 14-16 Noviembre de 2012.- Poster

7. Isern-Fontanet, J., **González-Haro, C.** (2012), Identification of vortices and reconstruction of their dynamics from combined SSH and SST satellite observations. Eos Trans. AGU Ocean Sci. Meet. Suppl. AbstractID: 11404

8. Isern-Fontanet, J., **González-Haro, C.** (2011), Retrieval of ocean currents from the synergy between SSH and SST. Sentinel Potential Science Products Assessment Consolidation Workshop, ESA-ESRIN Frascati, Italy, March 2011

Appendix E

List of acronyms

ADCP Acoustic Doppler Current Profilers

ADT Absolute Dynamic Topography

AMSR-E Advanced Microwave Scanning Radiometer for the Earth Observing System

AVISO Archiving, Validation and Interpretation of Satellite Oceanographic data

CNES Centre National d'Etudes Spatiales

CTD Conductivity Temperature Depth

DORIS Doppler orbitography and radiopositioning integrated by satellite

ECMWMF European Centre for Medium-range Weather Forescasting

eSQG effective Surface Quasi Geostrophic

FOV Field of view

GODAE Global Ocean Data Assimilation Experiment

IFREMER Institut Français de Reserche pour l'Exploitation de le MER

JAMSTEC Japan Agency for Marine-Earth Science and Technology

JASADCP Joint Archive for Shipboard ADCP

LADCP Lowered Acoustic Doppler Current Profiler

LOS Laboratoire d'Océanographie Spatiale

LWE Long Wavelengths Errors

MADT Map of Absolute Dynamic Topography

MCC Maximum Cross-Correlation

MDT Mean Dynamic Topography

MLD Mixed Layer Depth

MP Mean Profile

MSS Mean Sea Surface

MW Microwave

NOAA National Oceanic and Atmospheric Administration

NODC National Oceanographic Data Center

OGCM Ocean General Circulation Model

PV Potential Vorticity

RSS Remote Sensing Systems

SLA Sea Level Anomaly

SQG Surface Quasi Geostrophic

SSALTO Segment Sol Multimission Altimetry and Orbitography

SSS Sea Surface Salinity

SST Sea Surfaces Temperature

SWOT Surface Water and Ocean Topograhy

UNOLS University-National Oceanographic Laboratory System

WSOA Wide Swath Ocean Altimeter

Appendix F

Resumen

Las corrientes oceánicas son clave en muchos procesos oceánicos y climáticos, y su conocimiento es crucial para aplicaciones operacionales y de navegación. Por lo tanto, un aspecto importante en oceanografía es la estimación de campos sinópticos del campo de velocidades superficiales del mar. Actualmente, las velocidades superficiales el mar se estiman rutinariamente a partir de medidas del nivel del mar proporcionadas por altimetros, denotadas a partir de ahora con sus siglas en inglés SSH. Sin embargo, la separación entre las trazas del altimetro lleva a no localizar correctamente las corrientes oceánicas, si solo se utilizan este tipo de medidas para su estimación. Por contra, las imágenes de temperatura superficial del mar, denotadas a partir de ahora por sus siglas en inglés SST, proporiconan una visión cualitativa de la localización de las estructruas oceánicas. Este hecho ha motivado la investigación de metodologías alternativas para reconstruir los campos de velocidades superficiales del mar basados en estas observaciones. Esta tesis doctoral ha investigado la capacidad de las observaciones de SST proporcionadas por radiometros de microondas para recuperar las corrientes oceánicas superficiales. La reconstrucción de estas velocidades a partir de observaciones de SST se puede expresar en términos de una función de transferencia que relacione las observaciones de SST con las observaciones de SSH. Con lo que la estimación del campo de velocidades es directa, puesto que bajo la condición de equilibrio geostrófico la pendiente de la SSH es proporcional a las corrientes oceánicas. Esta función de transferencia se puede derivar teóricamente mediante las equaciones superficiales cuasi-geotróficas, denotadas con sus siglas en inglés SQG a partir de ahora. Una pregunta clave, es si las ecuaciones de este modelo dinámico son válidas. En esta tesis, se han llevado a cabo dos aproximaciones diferentes para la reconstrucción del campo de velocidades superficiales del mar: por un lado, el análisis de la validez de las ecuaciones SQG, y por otro, una aproximación basada en las propierdades sinergéticas entre medidas simultáneas de SST y SSH. El estudio se ha centrado en el período comprendido entre Octubre del 2002 y Mayo del 2005, puesto que durante este período habá disponibles hasta cuatro altmímetros, y consecuentemente la calidad de las observaciones es mayor.

El análisis de la validez de SQG a escala global reveló que este modelo dinámico es válido en las regiones cerca de los sistemas de corrientes extratropicales, como la corriente del Golfo, la Corriente Circumpolar Antártica (ACC), o la Kuroshio. Además, el potencial de las obser-

vaciones de SST en el rango de las microondas para la recuperación del campo de velocidades superficiales del mar, ha sido analizado utilizando un método que combina la fase de la SST con el espectro de SSH. En realidad, se ha investigado bajo que condiciones la SST y SSH están en fase. Los resultados mostraron que la fase de la SST de microondas puede utilizarse para para la reconstrucción en invierno, cerca de los sistemas de corrientes extratropicales, caracterizados por una intensa actividad de mesoscala y la presencia de fuertes gradientes termales, así como de capas de mezcla profundas. Asimismo, la reconstrucción del campo de velocidades a partir de una función de transferencia ideal, construida a partir de imágenes simultaneas de SST y SSH, reveló que la aproximación SQG puede ser mejorada.

Las propiedades espectrales de esta función de tranferencia ideal han sido estudiadas. Como primer intento, las propiedades espectrales de una función de transferencia media fueron caracterizadas a escala global. Los resulados mostraron una respuesta más plana que k^{-1}, la predecida por la teoria SQG, cerca de las corrietnes extratropicales, cuando la pendiente espectral se estimó en el rango entre los 100-400 km. Aunque la pendiente espectral era más cercana a k^{-1} en area muy energéticas si la estimación se restringía a rangos mÃąs bajos de longitud de onda (100-250 km). A continución se reconstruyó el flujo mediante una función de tranferncia que seguía un modelo k^{α} model, donde α era la pendiente espectral de estimada de una función de transferencia media. La evaluación de la reconstrucción desveló que la reconstrucción mediante una función de transferencia considerando la pendiente espectral estimada no mejoraba significativamente la reconstrucción mediante el modelo de SQG.

La variabilidad temporal de la función de transferencia fue analizada. Contrariamente a la aproximaciÃşn usada anteriormente, la pendiente espectral, en este caso, ajustamos la pendiente espectral en el espacio real. Para ello utilizamos dos métricas diferentes: (i) maximización de la correlación entre el flujo reconstruido a partir de la SST mediante la función de transferencia, y el flujo recosntruido a partir de observaciones altimétricas de SSH, y (ii) minimizando el error cuadrático medio entre ambos flujos. A pesar de que las pendientes espectrales estimadas diariamente puedan desviarse de k^{-1}, la media de las pendientes espectrales de ambas aproximaciones presentas patrones geográficos similares, con valores cercanos a k^{-1} en regiones muy energéticas, como en la ACC. Este análisis desveló que para escalas pequeñas y zonas enegéticas, la aproximación SQG es una buena aproximación, al menos, desde un punto de vista estádisco.

Bibliography

Afanasyev, Y. D., Kostianoy, A.G., Zatsepin, A.G., & Poulain, P.-M. 2002. Analysis of velocity field in the eastern Black Sea from satellite data during the Black Sea '99 experiment. *J. Geophys. Res.*, **107**.

Autret, Emmanuelle. 2014 (October). *Analyse de champs de température de surface de la mer à partir d' observations satellite multi-sources.* Ph.D. thesis, Université européenne de Bretagne-Télécom Bretagne.

Barlow, Roger J. 1989. *Statistics: a guide to the use of statistical methods in the physical sciences.* Vol. 29. John Wiley & Sons.

Blumen, W. 1978. Uniform potential vorticity flow: Part I. Theory of wave interactions and two-dimensional turbulence. *J. Atmos. Sci.*, **35**(5), 774–783.

Bowen, M, Enery, J.L., Wilkin, P., Tildeshey, P.C., Barton, I, & Knewston, R. 2002. Extracting multilayer surface currents from sequential thermal imagery using the maximum cross-correlation technique. *J. Atmos. Oceanic Technol.*, **19**, 1665–1676.

Bretherton, F. P. 1966. Critical layer instability in baroclinic flows. *Quart. J. Roy. Meteorol. Soc.*, **92**, 325–334.

Bretherton, F. P., Davis, R. E., & Fandris, C. B. 1976. A technique for objective analysis design of oceanographic experiments applied to MODE-73. *Deep-Sea Res.*, **23**, 559–582.

Buck, Christopher, Aguirre, Miguel, Donion, Craig, Petrolati, Daniele, & D'Addio, Salvatore. 2011 (july). Steps towards the preparation of a Wavemill mission. *Pages 3959–3962 of: Geoscience and Remote Sensing Symposium (IGARSS), 2011 IEEE International.*

Capet, Arthur, Mason, Evan, Rossi, Vincent, Troupin, Charles, Faugère, Yannice, Pujol, Isabelle, & Pascual, Ananda. 2014. Implications of refined altimetry on estimates of mesoscale activity and eddy-driven offshore transport in the Eastern Boundary Upwelling Systems. *Geophysical Research Letters*, **41**(21), 7602–7610.

Chapron, B., Collard, F., & Ardhuin, F. 2005. Direct measurements of ocean surface velocity from space: Interpretation and validation. *J. Geophys. Res.*, **110**, C07008.

Charney, Jule G. 1971. Geostrophic Turbulence. *J. Atmos. Sci.*, **28**(6), 1087–1095.

Chelton, Dudley B, & Wentz, Frank J. 2005. Global microwave satellite observations of sea surface temperature for numerical weather prediction and climate research. *Bull. Amer. Meteor. Soc.*

Cote, Stephane, & Tatnall, Adrian R. L. 2007. The use of the Hopfield neural network to measure sea-surface velocities from satellite images. *IEEE Geosci. Remote Sens. Lett.*, **4**(4), 624–628.

Couper, Alastair Dougal. 1983. *The Times Atlas of the Oceans [cartographic Material].* New York; Toronto: Van Nostrand Reinhold Company.

Davidson, Fraser JM, Allen, Arthur, Brassington, Gary B, Breivik, Øyvind, Daniel, Pierre, Kamachi, Masafumi, Sato, Satoshi, King, Brian, Lefevre, Fabien, Sutton, Marion, *et al.* . 2009. Applications of GODAE ocean current forecasts to search and rescue and ship routing. *Oceanography*, **22**(3), 176.

de Boyer Montégut, C, Madec, G., Fischer, A.S., Lazar, A., & Iudicone, I. 2004. Mixed layer depth over the global ocean: An examination of profile data and a profile-based climatology. *J. Geophys. Res.*, **109**.

Dibarboure, G, Schaeffer, P, Escudier, P, Pujol, M-I, Legeais, Jean-François, Faugère, Y, Morrow, Rosemary, Willis, JK, Lambin, Juliette, Berthias, JP, *et al.* . 2012. Finding Desirable Orbit Options for the "Extension of Life" Phase of Jason-1. *Marine Geodesy*, **35**(sup1), 363–399.

Donlon, C, Rayner, N, Robinson, I, Poulter, DJS, Casey, KS, Vazquez-Cuervo, J, Armstrong, E, Bingham, A, Arino, O, Gentemann, C, *et al.* . 2007. The global ocean data assimilation experiment high-resolution sea surface temperature pilot project. *Bull. Amer. Meteor. Soc.*, **88**(8), 1197–1213.

Donlon, CJ, Minnett, PJ, Gentemann, C, Nightingale, TJ, Barton, IJ, Ward, B, & Murray, MJ. 2002. Toward improved validation of satellite sea surface skin temperature measurements for climate research. *J. Climate*, **15**(4).

Dransfeld, Steffen, Larnicol, Gilles, & Le Traon, Pierre-Yves. 2006. The potential of the maximum cross-correlation technique to estimate surface currents from thermal AVHRR global area coverage data. *IEEE Geosci. Remote Sens. Lett.*, **3**(4), 508–511.

Ducet, N., Le Traon, P.Y., & Reverdin, G. 2000. Global high-resolution mapping of ocean circulation from TOPEX/Poseidon and ERS-1 and -2. *J. Geophys. Res.*, 19477–19498.

Emery, N. J., Thomas, A. C., Collins, M. J., Crawford, W.R., & Mackas, D.L. 1986. An objective method for computing advective surface velocities from sequential infrared satellite images. *J. Geophys. Res.*, **91**, 12865–12878.

Eymard, L., Tabary, L., Gerard, E., Boukabara, S.-A., & Le Cornec, A. 1996. The microwave radiometer aboard ERS-1. II. Validation of the geophysical products. *Geoscience and Remote Sensing, IEEE Transactions on*, **34**(2), 291–303.

Ferrari, R., & Paparella, F. 2003. Compensation and alignement of thermohaline gradients in the ocean mixed layer. *J. Phys. Oceanogr.*, **33**, 2214–2223.

Ferrari, R., & Rudnick, D.L. 2000. Thermohaline variability in the upper ocean. *J. Geophys. Res.*, **105**, 16857–16883.

Frasier, S.J., & Camps, A.J. 2001. Dual-beam interferometry for ocean surface current vector mapping. *Geoscience and Remote Sensing, IEEE Transactions on*, **39**(2), 401–414.

Fu, Lee-Lueng, & Rodriguez, E. 2003. Wide-swath altimetric measurement of ocean surface topography. *In: 2003 IUGG Conference.*

Gommenginger, Christine, Wishart, Alex, Srokosz, Meric, & Richards, Byron. 2010. *The Wavemill 2D Ocean Current Mapping System: On-Board Signal Processing and Architecture Definition.* `http://www.aviso.oceanobs.com/fileadmin/documents/OSTST/2010/Gommenginger_Wavemill.pdf`.

Goody, R.M., & Y.L-Young. 1998. *Atmospheric Radiation.* Oxford University Press.

Handbook, SSALTO/DUACS User. 2012 (December). *(M)SLA and (M)ADT Near-Real Time and Delayed Time Products.* 3rev 3 edn. AVISO, SSALTO. CLS-DOS-NT-06-034.

Handbook, SSALTO/DUACS User. 2014a (May). *(M)SLA and (M)ADT Near-Real Time and Delayed Time Products.* 4rev 1 edn. AVISO, SSALTO. SALP-MU-P-EA-21065-CLS.

Handbook, SSALTO/DUACS User. 2014b (November). *(M)SLA and (M)ADT Near-Real Time and Delayed Time Products.* 4rev 2 edn. AVISO, SSALTO. CLS-DOS-NT-06-034.

Hansen, Donald V, & Herman, Alan. 1989. Temporal sampling requirements for surface drifting buoys in the tropical Pacific. *J. Atmos. Oceanic Technol.*, **6**(4), 599–607.

Hansen, Donald V, & Poulain, Pierre-Marie. 1996. Quality control and interpolations of WOCE-TOGA drifter data. *J. Atmos. Oceanic Technol.*, **13**(4), 900–909.

Hausmann, Ute, & Czaja, Arnaud. 2012. The observed signature of mesoscale eddies in sea surface temperature and the associated heat transport. *Deep Sea Research Part I: Oceanographic Research Papers*, **70**(0), 60 – 72.

Held, I., Pierrehumbert, R.T., Garner, S.T., & Swanson, K.L. 1995. Surface quasi-geostrophic dynamics. *J. Fluid Mech.*, **282**, 1–20.

Hoskins, B.J, McIntyre, M.E., & A.W., Robertson. 1985. On the use and significance of isentropic potential vorticity maps. *Quart. J. Roy. Meteorol. Soc.*, **111**, 877–946.

Hosoda, Kohtaro. 2010. A review of satellite-based microwave observations of sea surface temperatures. *Journal of oceanography*, **66**(4), 439–473.

Hosoda, Kohtaro, & Hanawa, Kimio. 2004. Anticyclonic eddy revealing low sea surface temperature in the sea south of Japan: case study of the eddy observed in 1999–2000. *Journal of oceanography*, **60**(4), 663–671.

Hosoda, Shigeki, Ohira, Tsuyoshi, Sato, Kanako, & Suga, Toshio. 2010. Improved description of global mixed-layer depth using Argo profiling floats. *Journal of Oceanography*, **66**(6), 773–787.

Imaoka, K., Kachi, M., Fujii, H., Murakami, H., Hori, M., Ono, A., Igarashi, T., Nakagawa, K., Oki, T., Honda, Y., & Shimoda, H. 2010. Global Change Observation Mission (GCOM) for Monitoring Carbon, Water Cycles, and Climate Change. *Proceedings of the IEEE*, **98**(5), 717–734.

Imel, David A. 1994. Evaluation of the TOPEX/POSEIDON dual-frequency ionosphere correction. *J. Geophys. Res.*, **99**(C12), 24895–24906.

Isern-Fontanet, J., Chapron, B., Klein, P., & G., Lapeyre. 2006. Potential use of microwave SST for the estimation of surface ocean currents. *Geophys. Res. Lett.*, **33**, L24608.

Isern-Fontanet, J., A., Turiel, García-Ladona, & Font, J. 2007. Microcanonical multifractal formalism: Application to the estimation of ocean surface velocities. *J. Geophys. Res.*, **112**, C05024.

Isern-Fontanet, J, Lapeyre, G., Klein, P., Chapron, B., & Hetcht, M. 2008. Three-dimensional reconstruction of oceanic mesoscale currents from surface information. *J. Geophys. Res.*, C09005.

Isern-Fontanet, J., Shinde, M., & González-Haro, C. 2014. On the transfer function between surface fields and the geostrophic stream function in the Mediterranean Sea. *J. Phys. Oceanogr.*, **44**, 1406–1423.

Kawanishi, T., Sezai, T., Ito, Y., Imaoka, K., Takeshima, T., Ishido, Y., Shibata, A., Miura, M., Inahata, H., & Spencer, R.W. 2003. The Advanced Microwave Scanning Radiometer for the Earth Observing System (AMSR-E), NASDA's contribution to the EOS for global energy and water cycle studies. *IEEE Trans. Geosci. Remote Sens.*, **41**(2), 184–194.

Kelly, K. A. 1989. An inverse model for near-surface velocity from infrared images. *Journal of Physical Oceanography*, **19**, 1845–1864.

Klein, L, & Swift, Calvin T. 1977. An improved model for the dielectric constant of sea water at microwave frequencies. *Antennas and Propagation, IEEE Transactions on*, **25**(1), 104–111.

Klein, P., & Hua, B.L. 1990. The mesoscale variability of the sea surface temperature: an analytical and numerical model. *J. Mar. Res.*, **48**, 729–763.

Klein, P., Tréguier, A.M., & Hua, B.L. 1998. Quasigeostrophic stirring of thermohaline fronts. *J. Mar. Res.*, **56**, 589–612.

Klein, Patrice, Lapeyre, Guillaume, Roullet, Guillaume, Le Gentil, Sylvie, & Sasaki, Hideharu. 2011. Ocean turbulence at meso and submesoscales: connection between surface and interior dynamics. *Geophys. Astrophys. Fluid Dyn.*, **105**(4-5), 421–437.

Kolmogorov, Andrey Nikolaevich. 1941. The local structure of turbulence in incompressible viscous fluid for very large Reynolds numbers. *Pages 299–303 of: Dokl. Akad. Nauk SSSR*, vol. 30.

LaCasce, JH. 2012. Surface quasigeostrophic solutions and baroclinic modes with exponential stratification. *J. Phys. Oceanogr.*, **42**(4), 569–580.

LaCasce, J.H., & Mahadevan, A. 2006. Estimating subsurface horizontal and vertical velocities from sea surface temperature. *J. Mar. Res.*, **64**, 695–721.

Lane, JA, & Saxton, JA. 1952. Dielectric dispersion in pure polar liquids at very high radio frequencies. III. The effect of electrolytes in solution. *Proceedings of the Royal Society of London. Series A. Mathematical and Physical Sciences*, **214**(1119), 531–545.

Lapeyre, G. 2009. What Vertical Mode Does the Altimeter Reflect? On the Decomposition in Baroclinic Modes and on a Surface-Trapped Mode. *J. Phys. Oceanogr.*, **39**(11).

Lapeyre, G., & Klein, P. 2006a. Dynamics of the Upper Oceanic Layers in Terms of Surface Quasigeostrophy Theory. *J. Phys. Oceanogr.*, **36**, 165–176.

Lapeyre, G., & Klein, P. 2006b. Impact of the small-scale elongated filaments on the oceanic vertical pump. *J. Mar. Res.*

Le Traon, P.-Y., & Dibarboure, G. 1999. Mesoscale mapping capabilities of multi-satellite altimeter missions. *J. Atmos. Oceanic Technol.*, **16**, 1208–1223.

Le Traon, P.Y., & Dibarbourne, G. 2002. Velocity Mapping Capabilities of Present and Future Altimeter Missions: The Role of High-Frequency Signals. *J. Atmos. Oceanic Technol.*, **19**, 2077–2087.

Le Traon, P.Y., Nadal, F., & Ducet, N. 1998. An improved mapping method of multisatellite altimeter data. *J. Atmos. Oceanic Technol.*, **15**, 522–534.

Le Traon, PY, Dibarboure, G, & Ducet, N. 2001. Use of a high-resolution model to analyze the mapping capabilities of multiple-altimeter missions. *Journal of Atmospheric and Oceanic Technology*, **18**(7), 1277–1288.

Le Traon, P.Y., Klein, P., Hua, B.L., & Dibarbourne, G. 2008. Do altimeter wavenumber spectra agree with interior or surface quasi-geostrophic theory? *J. Phys. Oceanogr.*, **38**, 1137–1142.

Lebedev, Konstantin V, Yoshinari, Hiroshi, Maximenko, Nikolai A, & Hacker, Peter W. 2007. Velocity data assessed from trajectories of Argo floats at parking level and at the sea surface. *IPRC Tech. Note*, **4**(2), 1–16.

Lumpkin, Rick, & Johnson, Gregory C. 2013. Global ocean surface velocities from drifters: Mean, variance, El Nino–Southern Oscillation response, and seasonal cycle. *J. Geophys. Res.*, **118**(6), 2992–3006.

Lumpkin, Rick, & Pazos, Mayra. 2007. Measuring surface currents with Surface Velocity Program drifters: the instrument, its data, and some recent results. *Lagrangian analysis and prediction of coastal and ocean dynamics*, 39–67.

Marcello, J., Eugenio, F., Marques, F., Hernandez-Guerra, A., & Gasull, A. 2008. Motion Estimation Techniques to Automatically Track Oceanographic Thermal Structures in Multisensor Image Sequences. *Geoscience and Remote Sensing, IEEE Transactions on*, **46**(9), 2743–2762.

McCord, Mark R, Lee, Young-Kyun, & Lo, Hong Kam. 1999. Ship routing through altimetry-derived ocean currents. *Transport. Sci.*, **33**(1), 49–67.

Meissner, T., & Wentz, F. 2002. An updated analysis of the ocean surface wind direction signal in passive microwave brightness temperatures. *IEEE Trans. Geosci. Remote Sens.*, **40**(6), 1230–1240.

Meissner, T., & Wentz, F. 2005. Ocean retrievals for WindSat: radiative transfer model, algorithm, validation. *Pages 130–133 Vol. 1 of: OCEANS, 2005. Proceedings of MTS/IEEE.*

Meissner, T., & Wentz, F.J. 2004. The complex dielectric constant of pure and sea water from microwave satellite observations. *IEEE Trans. Geosci. Remote Sens.*, **42**(9), 1836–1849.

Millero, Frank J., Feistel, Rainer, Wright, Daniel G., & McDougall, Trevor J. 2008. The composition of Standard Seawater and the definition of the Reference-Composition Salinity Scale. *Deep-Sea Res. II*, **55**(1), 50 – 72.

Niiler, P. P., & Paduan, J. D. 1995. Wind–driven motions in the northeast Pacific as measured by Lagrangian drifters. *J. Phys. Oceanogr.*, **31**, 2819–2830.

Niiler, Peter. 2001. The world ocean surface circulation. *International Geophysics*, **77**, 193–204.

Okuyama, A., & Imaoka, K. 2015. Intercalibration of Advanced Microwave Scanning Radiometer-2 (AMSR2) Brightness Temperature. *Geoscience and Remote Sensing, IEEE Transactions on*, **PP**(99), 1–10.

Park, Jong Jin, Kim, Kuh, King, Brian A, & Riser, Stephen C. 2005. An advanced method to estimate deep currents from profiling floats. *J. Atmos. Oceanic Technol.*, **22**(8), 1294–1304.

Pascual, A., Faugeère, Y., Larnicol, G., & Le Traon, P.Y. 2006. Improved description of the ocean mesoscale variability by combining four satellite altimeters. *Geophys. Res. Lett.*, **33**, L02611.

Pierrehumbert, R.T., Held, I., & Swanson, K.L. 1994. Spectra of local and nonlocal two-dimensional turbulence. *Chaos, Solitons & Fractals*, **4**(6), 1111–1116.

Planck, Max. 1901. On the law of distribution of energy in the normal spectrum. *Annalen der Physik*, **4**(553), 1.

Press, W. H., Teukolsky, S. A., Vetterling, W. T., & Flannery, B. P. 2007. *Numerical Recipes: The art of scientific computing.* Third edition edn. Cambridge University Press.

Quartly, G. D., Guymer, T. H., & Srokosz, M. A. 1996. The Effects of Rain on Topex Radar Altimeter Data. *J. Atmos. Oceanic Technol.*, **13**, 1209–1229.

Reul, Nicolas, Chapron, Bertrand, Lee, Tong, Donlon, Craig, Boutin, Jacqueline, & Alory, G. 2014. Sea surface salinity structure of the meandering Gulf Stream revealed by SMOS sensor. *Geophys. Res. Lett.*, **41**(9), 3141–3148.

Robinson, Ian. S. 2004. *Measuring the Oceans from Space: The principles and methods of satellite oceanography.* Springer/Praxis.

Rodriguez, E, Pollard, B, & Martin, J. 1999. Wide-swath ocean altimetry using radar interferometry.

Ruf, Christopher S., Keihm, Stephen J., Subramanya, Bala, & Janssen, Michael A. 1994. TOPEX/POSEIDON microwave radiometer performance and in-flight calibration. *J. Geophys. Res.*, **99**(C12), 24915–24926.

Sasaki, Hideharu, & Klein, Patrice. 2012. SSH wavenumber spectra in the North Pacific from a high-resolution realistic simulation. *J. Phys. Oceanogr.*, **42**(7), 1233–1241.

Saunders, Peter M. 1967. The temperature at the ocean-air interface. *J. Atmos. Sci.*, **24**(3), 269–273.

Service, Robert F. 1996. Rock Chemistry Traces Ancient Traders. *Science*, **274**(5295), 2012–2013.

Stewart, Robert Henry. 2004. *Introduction to physical oceanography.* Texas A & M University.

Sybrandy, A. L., & Niiler, P. P. 1991. *WOCE/TOGA Lagrangian drifter construction manual.* Tech. rept. WOCE Rep. 63, SOI Ref. 91/6. Scripps Inst. of Oceanogr., La Jolla, California.

Tandeo, P., Chapron, B., Ba, S., Autret, E., & Fablet, R. 2014. Segmentation of Mesoscale Ocean Surface Dynamics Using Satellite SST and SSH Observations. *Geoscience and Remote Sensing, IEEE Transactions on*, **52**(7), 4227–4235.

Tokmakian, R., Strub, P.T., & McClean-Padman, J. 1990. Evaluation of the Maximum Cross-Correlation Method of Estimating Sea Surface Velocities from Sequential Satellite Images. *J. Atmos. Oceanic Technol.*, **7**, 852–865.

Tulloch, R., & Smith, K.S. 2006. A New Theory for the Atmospheric Energy Spectrum: Depth-Limited Temperature Anomalies at the Tropopause. *P. Natl. Acad. Sci. USA*, **103**(40), 14690–14694.

Turiel, A., Isern-Fontanet, J., García-Ladona, E., & Font, J. 2005. A multifractal method for the instantaneous evaluation of the stream-function in geophysical flows. *Pys. Rev. Lett.*, **95**.

Turiel, A., Nieves, V., Garcia-Ladona, E., Font, J., Rio, M.-H., , & Larnicol, G. 2009. The multifractal structure of satellite sea surface temperature maps can be used to obtain global maps of streamlines. *Ocean Sci.*, 447–460.

Vallis, G. K. 2006. *Atmospheric and Oceanic Fluid Dynamics.* Cambridge, U.K.: Cambridge University Press.

Vigan, X., Provost, C., Bleck, R., & Courtier, P. 2000. Sea surface velocities from sea surface temperature images sequence 1. Method and validation using primitive equation model output. *J. Geophys. Res.*, **105**(C08), 19499–19514.

Wang, Jinbo, Flierl, Glenn R, LaCasce, Joseph H, McClean, Julie L, & Mahadevan, Amala. 2013. Reconstructing the Ocean's Interior from Surface Data. *J. Phys. Oceanogr.*, **43**(8).

Wentz, F. J., & Meissner, T. 2000 (November). *AMSR Ocean Algortihm (Version 2), Algorithm Theorical Basis Document (ATBD).* Tech. rept. Remote Sensing Systems, Santa Rosa, CA.

Wentz, F. J., & Meissner, T. 2007 (May). *Supplement 1 Algorithm Theoretical Basis Document for AMSR-E Ocean Algorithms.* Tech. rept. Remote Sensing Systems, Santa Rosa, CA.

Xu, Y., & Fu, L.-L. 2012. The effects of altimeter instrument noise on the estimation of the wavenumber spectrum of sea surface height. *Journal of Physical Oceanography*, **42**, 2229–2233.

Xu, Yongsheng, & Fu, Lee-Lueng. 2011. Global Variability of the Wavenumber Spectrum of Oceanic Mesoscale Turbulence. *J. Phys. Oceanogr.*, **41**(4), 802–809.

Yu, Yang, Wang, Longfei, Zheng, Quan'an, & Li, Ziwei. 2014. Geostrophic current estimation using altimetric cross-track method in northwest Pacific. *Page 012105 of: IOP Conference Series: Earth and Environmental Science*, vol. 17. IOP Publishing.